ORTHOGONAL DECOMPOSITION METHODS FOR TURBULENT HEAT TRANSFER ANALYSIS WITH APPLICATION TO GAS TURBINES

A Dissertation

by

MARKUS SCHWÄNEN

Submitted to the Office of Graduate Studies of
Texas A&M University
in partial fulfillment of the requirements for the degree of

DOCTOR OF PHILOSOPHY

May 2011

Major Subject: Mechanical Engineering

ORTHOGONAL DECOMPOSITION METHODS FOR TURBULENT HEAT TRANSFER ANALYSIS WITH APPLICATION TO GAS TURBINES

A Dissertation

by

MARKUS SCHWÄNEN

Submitted to the Office of Graduate Studies of
Texas A&M University
in partial fulfillment of the requirements for the degree of

DOCTOR OF PHILOSOPHY

Approved by:

Chair of Committee,	Andrew Duggleby
Committee Members,	Prabir Daripa
	Devesh Ranjan
	Taher Schobeiri
	Sy-Bor Wen
Head of Department,	Dennis O'Neal

May 2011

Major Subject: Mechanical Engineering

ABSTRACT

Orthogonal Decomposition Methods for Turbulent
Heat Transfer Analysis with Application to Gas Turbines. (May 2011)
Markus Schwänen, Diplom-Ingenieur, Technical University Darmstadt, Germany
Chair of Advisory Committee: Dr. Andrew Duggleby

Gas turbine engines are the main propulsion source for world wide aviation and are also used for power generation. Even though they rely mainly on fossil fuel and emit climate active gasses, their importance is not likely to decrease in the future. But more efficient ways of using finite resources and hence reducing emissions have to be found. Thus, the interest to improve engine efficiency is growing. Considering the efficiency of the underlying thermodynamic cycle, an increase can be achieved by raising the turbine inlet temperature or compression ratio. Due to the complex nature of the underlying flow physics, however, the aero-thermal processes are still not fully understood. For this reason, one needs to perform research at high spatial and temporal resolution, in turn creating the need for effective means of postprocessing the large amounts of data.

This dissertation addresses both sides of the problem - using high-scale, high resolution simulations as well as effective post processing techniques. As an example for the latter, a temporal highly resolved data set from wall pressure measurements of a transonic compressor stage is analyzed using proper orthogonal decomposition. The underlying experiments were performed by collaborators at Technical University Darmstadt. To decompose signals into optimal orthogonal basis functions based on temporal correlations including temperature, a formal mathematical framework is developed. A method to rank the reduced order representations with respect to heat transfer effectiveness is presented. To test both methods, a Reynolds-averaged

Navier-Stokes (RANS) simulation and large eddy simulation (LES) are performed on turbulent heat transfer in a square duct with one single row of pin fins. While the LES results show closer agreement to experiments, both simulations unveil flow parts that do not contribute to heat transfer augmentation and can be considered wasteful. From the most effective mode, a wall contour for the same domain is derived and applied. In the wall contoured domain, energy in wasteful modes decreased, heat transfer increased and the temperature fluctuations at the wall decreased.

Another stagnating boundary layer flow is examined in a direct numerical simulation of a first stage stator vane. Elevated levels of free stream turbulence and integral length scale are generated to simulate the features of combustor exit flow. The horseshoe vortex dynamics cause an increase in endwall heat transfer upstream of the vane. The link between energy optimal orthogonal basis functions and flow structures is examined using this data and the reduced order heat transfer analysis shows high energy modes with comparatively low impact on turbulent heat transfer. The analysis further shows that there are multiple horseshoe vortices that oscillate upstream of the blade, vanish, regenerate and can also merge. There is a punctual correlation of intense vortex dynamics and peaks in the orthogonal temperature basis function.

For all data considered, the link between the energy optimal orthogonal basis functions and flow structures is neither guaranteed to exist nor straightforward to establish. The orthogonal expansion locks onto flow parts with high fluctuating kinetic energy - which might or might not be the ones that are looked for. The heat transfer ranking eliminates this problem and is valid independently of how certain basis functions are interpreted.

To my family

ACKNOWLEDGMENTS

First and foremost, I would like to thank my advisor Dr. Andrew Duggleby. Your unconditional trust and faith in me as a person and researcher has made success almost an obligation and is a constant inspiration for my interaction with other people. I am deeply thankful for your scientific creativity as well as the freedom you granted me to explore.

I would also like to thank my committee members as well as Dr. Thole, Dr. Fischer, Dr. Schiffer, and Dr. Müller for many helpful discussions.

The life and work experience at A&M, in Texas, and in the Unites States was made so much more joyful due to the presence and activities of my fellow lab mates Dallas, Jared, Josh, Marshall, Michael, Pradeep, Sebastian, Shriram, and William. Thank you all for your kindness, hospitality, help, and friendship. For all the support I got while at Virginia Tech, I would like to thank Joe, Nick, Stephen, and Sundar.

I was lucky to be able to live my life like I did because of my parents Ursula and Dieter - thank you for your love, confidence, and sacrifice that took away doubts and sorrows.

The love I receive from my wife Susanne adds sense to everything I do. She is the driving force to overcoming my inertia and a great person. I love you.

TABLE OF CONTENTS

CHAPTER Page

LIST OF TABLES

LIST OF FIGURES

FIGURE Page

FIGURE Page

FIGURE Page

FIGURE Page

FIGURE Page

FIGURE Page

FIGURE Page

NOMENCLATURE

Greek Symbols

α, λ	Eigenvalue
Δ_2	Convective boundary layer enthalpy thickness
φ, Φ	Spatial basis function
Ψ	Time basis function
ρ	Density

Superscripts

ϑ	Based on mean temperature and velocity
ς	Based on fluctuating temperature and velocity
n, m, k	Order of OD modes
$\bar{}$	Time-averaged part
$'$	Fluctuating part

Roman Symbols

$A_i(\vec{x}, t)$	Signal vector
C_{ax}	Axial turbine chord
C	Turbine chord
C_L, C_D	Lift and drag coefficient

c_p, c_v	Specific heat capacity
D	Pin diameter
DNS	Direct numerical simulation
$\dot{E}_{Conv}$	Convective energy transport
Ec	Eckert number
$\dot{E}_{Diff}$	Diffusive energy transport
H	Channel height in pin fin domain
h_{ref}	Specific enthalpy
i_{ref}	Stagnation/total enthalpy
LES	Large eddy simulation
L^2	Function space
$\vec{n}$	Unit vector normal on control surface/line
Nu_0, f_0	Nusselt number and friction factor of unobstructed channel
$PISO$	Pressure-implicit with splitting of operators: Pressure-velocity coupling scheme
$\dot{q}$	Heat flux
$\dot{q}''$	Specific heat flux
$\mathrm{Re} = U_0 2D/\nu$	Reynolds number based on channel hydraulic diameter for pin fin domain

Re	Reynolds number Re $= U_\infty C/\nu$ for turbine simulation
S	Spanwise pin spacing
St	Stanton number $St = h/\rho C_p U_\infty$
Str	Strouhal number
T	Static temperature
$\mathfrak{T}$	Non-dimensionalized and weighted temperature
$\overline{T_{in}}$	Average inflow temperature
$\overline{T_{out}}$	Average exit temperature
U, U^*, R, S	Operators
$\mathbf{U}$	Velocity magnitude
U_0	Bulk flow velocity
U_∞	Freestream velocity in turbine domain
$URANS$	Unsteady Reynolds-averaged Navier-Stokes
u, v, w	Non-dimensionalized velocity components
$\dot{W}$	Shear work
x^+, y^+, z^+	Non-dimensional wall distance/grid point spacing based on turbulence scales
X, Y, Z	Streamwise, pitchwise and spanwise coordinate in turbine domain

Subscripts

∞	Evaluated far away from surface
ϕ	Available or potential
s	Evaluated at surface
Y	Evaluated at top of control volume

CHAPTER I

INTRODUCTION

A. Background and motivation

Gas turbine engines comprise most of the world's aviation transport and a considerable part of its electricity generation. The high power-to-weight ratio as well as the high dynamical response make the gas turbine particularly attractive for these applications. According to the 2009 electric power annual report [1], around 20% of the electricity generation capacity in the US is alloted to combined-cycle units. The role of gas turbines is not likely to decrease in the future, even though most rely on burning fossil fuel. But due to the increasing sense of a necessity to curb emissions for limiting climate change and the finite availability of carbon based combustibles, the interest to improve engine efficiency is growing. A small improvement in efficiency in these systems corresponds to drastic energy and economic savings due to their wide spread use.

Even though these complex systems were advanced for more than 50 years, the gas turbine engine is still not fully understood. Some of the basic components and relations can be seen in Fig. 1. The working fluid, typically air, enters the compressor (from left to right in Fig. 1), in which pressure and temperature increase. Heat is then added in the combustion chamber and the gas expands over the following turbine, which in turn drives the compressor. Work can be extracted from the shaft or the exit stream in terms of thrust. The thermodynamic efficiency of this open cycle depends on the pressure increase over the compressor mostly or the temperature ratio between the surroundings and the combustor exit. In the real engine, those parameters are

---

The journal model is *IEEE Transactions on Automatic Control.*

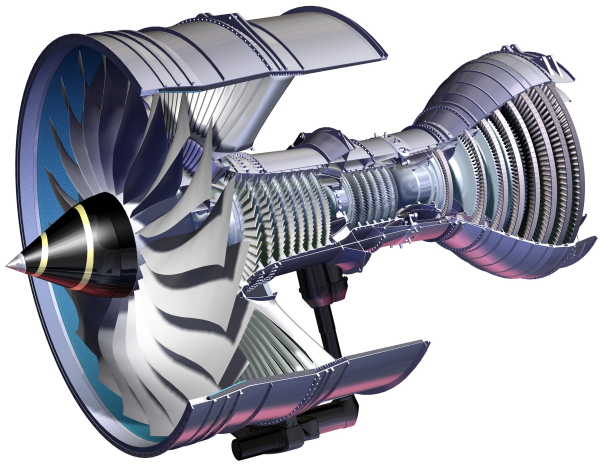

Fig. 1.: The civil jet engine Trent 1000 from Rolls Royce with fan, compressor stages, combustion chamber and turbine stages from [2].

constrained by aerodynamic effects or material properties. For example, stall on the compressor blades limits the pressure increase one stage can deliver. The blade metal melting temperature, on the other hand, determines the necessary cooling measures to avoid part failure. The underlying flow physics are highly complex and unsteady, for example shock fronts interacting with clearance flow and high free stream turbulence affecting heat transfer at the blade hub. There is thus a need for high spatial and temporal resolution in experiments and numerical simulations.

In terms of numerical investigations, an accurate and fast Navier Stokes solver needs to fulfill these requirements. For the work presented in this dissertation, the spectral element code Nek5000 [3] is chosen because it is highly parallelizable, accurate and can handle complex geometries. Its positive attributes originate, among other things, from the use of spectral basis functions within a mesh of discrete hexahedral elements. Within each element, the solution is approximated by Lagrangian interpolants of a user defined order. For an optimum of parallel performance and

solution accuracy, a polynomial order of typically 7-11 is chosen. Even though non-orthogonal elements are allowed, the most efficient solving process will be achieved by elements with as little skewness as possible and an aspect ratio which is uniform and close to unity. To approximate arbitrarily formed surfaces, first or second order functions are used to distribute the grid points on element faces and edges. The use of spectral solution functions facilitates the implementation of filtering for turbulence models or improved stability, since applying a filter to certain variables is done by multiplying the polynomial coefficients with chosen filter values. The exponential solution convergence that spectral elements provide is thereby not diminished. To ensure stability at high Reynolds numbers, dealiasing is implemented in the code. The time discretization is of second or third order. The characteristics time stepping scheme allows for time steps yielding a Courant number larger than unity.

Effective and insightful analysis techniques are needed for the large amounts of data generated by numerical or experimental investigations. Therefor, an analysis methodology is derived based on orthogonal decomposition. For problems involving convection, it is shown how the reduced order representation is used to rank basis functions with respect to their relevance for heat transfer.

B. Dissertation structure

The first chapter describes the mathematical background of decomposition and ranking, which is used in the following chapters. In the second chapter, static wall pressure measurements from a transonic compressor cascade are analyzed with orthogonal expansion. The third chapter presents numerical simulations of heat transfer in a simplified internal blade cooling pin fin passage with a lower order turbulence model (Reynolds-averaged Navier-Stokes) and more accurate large eddy simulations, includ-

ing an orthogonal expansion analysis. These results are used for the work presented in the fourth chapter, where the pin fin heat exchanger is optimized by wall contouring based on the orthogonal basis functions. A direct numerical simulation of heat transfer in the stagnation region of a first stage stator vane is presented in the fifth chapter and the data analyzed with the developed techniques. Each of the four sections has its individual introduction, background and conclusion section to generate a complete project description. In the last chapter, common conclusions are drawn from all presented projects and an outlook on future work is given.

CHAPTER II

MATHEMATICAL BACKGROUND

In three dimensional convective heat transfer problems, where surface heat transfer by introducing unsteadiness (either due to turbulence, in the bulk flow or both), the classical proper orthogonal decomposition yields a set of vectorial spatial functions combined with scalar time coefficients. This allows for some conclusions on the *spatial* distribution of flow structures and corresponding temperature fluctuations. In engineering applications, however, optimizing these heat exchangers to achieve high *time averaged* heat transfer relative to, for example, pressure loss is usually of great interest. For heat transfer in a pin fin cooling channel, for example, flow structures that do not contribute to heat transfer enhancement could be identified by their time trace instead of spatial (time-averaged) appearance. The mathematical framework for an orthogonal decomposition in time and space was first proposed by Aubry et al. (1991) [4]. A variant of this expansion is derived in Section A following the steps of Aubry et al. (1991) [4]. The basis functions or reduced order representations can be used to assess heat transfer effectiveness. A framework is derived in Section B, where different scenarios will be distinguished:

- Internal or external flow
- Heating or cooling
- Constant wall temperature or constant heat flux (adiabatic wall) boundary condition.

A. Time orthogonal decomposition (TOD)

1. TOD with vectorial time eigenfunctions

The expansion based on a variant of Aubry et al. (1991) [4] results in a scalar spatial field and a vector time signal. Because the vector component of the orthogonal expansion is associated with time, the term Time-Orthogonal Decompostion will be used to describe this variant.

The following derivation is similar to Aubry et al. (1991) [4], but uses a multi-dimensional signal $A_i(x,t)$ from the start and only real functions are considered.

Definition A.1. $A_i(\vec{x},t)$ is a real, measurable, square-integrable, vectorial function of space and time.

$$A_i(\vec{x},t) = [A_1, A_2, A_3, A_4], \mathbf{A} \in L^2(X \mathbf{x} \mathbf{T}), X \subset \mathbb{R}^1, \mathbf{T} \subset \mathbb{R}^4,$$

where A_1, A_2, A_3, A_4 are arbitrary functions of x, t.

Remark A.2. Even though the problem is three-dimensional in space, the spatial coordinate $x \in \mathbb{R}^1$ is a scalar and can be thought of as a pointer variable identifying a particular control volume of a discretized domain. This does not hinder spatial integration because it is approximated by a summation over grid cell volumes. For problems involving unstructured grids, as is the case for the simulations under consideration, spatial correlations are hard to find due to numerical reason. From the traditional POD methods, the "Method of Snapshots" ([5]) overcomes this limitation by using correlations in time.

Proposition A.3. *We define a linear operator*

$$U : L^2(X) \rightarrow L^2(\mathbf{T})$$

such that

$$\forall \varphi \in L^2(X), (U\varphi)_i(t) = \int_X A_i(\vec{x}, t)\varphi(\vec{x})dx \tag{2.1}$$

and the adjoint operator

$$U^* : L^2(\mathbf{T}) \to L^2(X)$$

such that

$$\forall \mathbf{\Psi} \in L^2(\mathbf{T}), (U^*\mathbf{\Psi})(\vec{x}) = \int_T A_i(\vec{x}, t)\Psi_i(t)dt. \tag{2.2}$$

Note that $\int_X(\cdot)dx$ *is* $\frac{1}{X}\int(\cdot)dx$ *and* $\int_T(\cdot)dt$ *is* $\frac{1}{T}\int(\cdot)dt$.

Proof. Due to Hoelder's inequality and because $\mathbf{A} \in L^2(X\times\mathbf{T})$, Eqn. (2.1) and Eqn. (2.2) define bounded operators (see [6], lemma II.1.6 example j).

The order of integration in the following is interchangeable due to Fubini-Tonelli's theorem since U is bounded and continous. One can show that U^* is the adjoint operator of U by considering an inner product

$$\begin{aligned}
(\mathbf{\Psi}, U\varphi) &= \int_T \Psi_i(t)(U\varphi)_i(t)dt \\
&= \int_T \int_X \Psi_i(t)A_i(\vec{x}, t)\varphi(\vec{x})dxdt \\
&= \int_X \varphi(\vec{x}) \int_T A_i(\vec{x}, t)\Psi_i(t)dtdx \\
&= \int_X \varphi(\vec{x})(U^*\mathbf{\Psi})_{(\vec{x})}dx \\
&= (U^*\mathbf{\Psi}, \varphi).
\end{aligned}$$

Proposition A.4. *The analysis of the signal* $A_i(\vec{x}, t)$ *is reduced to the spectral analysis of* U*, which is compact for* $\mathbf{A} \in L^2(X\times\mathbf{T})$*. This is motivated by the existence of*

orthonormal functions in X and $\mathbf{T}$ as shown in [6] (theorem VI.3.6).

Proposition A.5. *We introduce an operator*

$$R : L^2(\mathbf{T}) \to L^2(\mathbf{T})$$

such that

$$R = UU^*,$$

which means that U operates on U^*, and

$$S : L^2(X) \to L^2(X)$$

such that

$$S = U^*U.$$

The operator R is a non-negative, integral (tensorial) operator whose kernel is the temporal correlation of the signal $A_i(\vec{x}, t)$ and the operator S is a non-negative, integral operator whose kernel is the spatial two-point correlation of the signal $A_i(\vec{x}, t)$.

Proof. Both operators are compact since U is compact and positive when satisfying (see [6], theorem III.4.4 and equation VI.7):

$$\begin{aligned} (R\mathbf{\Psi}, \mathbf{\Psi}) &= (UU^*\mathbf{\Psi}, \mathbf{\Psi}) & (S\varphi, \varphi) &= (U^*U\varphi, \varphi) \\ &= (U\mathbf{\Psi}, U\mathbf{\Psi}) & &= (U\varphi, U\varphi) \\ &= \int_T (U\mathbf{\Psi})^2 dt & &= \int_X (U\varphi)^2 dx \\ &\geq 0 & &\geq 0. \end{aligned}$$

To show the operator kernel, we consider a function set $\mathbf{\Psi}$ in $L^2(\mathbf{T})$.

$$\begin{aligned}(R\mathbf{\Psi})_{j(t)} &= (UU^*\mathbf{\Psi})_{j(t)} \\ &= \int_X A_j(\vec{x},t)(U^*\mathbf{\Psi})_{(\vec{x})}dx \\ &= \int_X\int_T A_j(\vec{x},t)A_i(\vec{x},t')\Psi_{i(t')}dxdt' \\ &= \int_T r_{ij}(t,t')\Psi_i(t')dt'\end{aligned}$$

Here, $r_{ij}(t,t') = \int_X A_j(\vec{x},t)A_i(\vec{x},t')dx$ is the (tensorial) temporal correlation function of the signal.

Similarily, considering a function $\varphi(\vec{x})$ in $L^2(X)$

$$\begin{aligned}(S\varphi)_{(\vec{x})} &= (U^*U\varphi)_{(\vec{x})} \\ &= \int_T A_i(\vec{x},t)(U\varphi)_{i(t)}dt \\ &= \int_T\int_X A_i(\vec{x},t)A_i(\vec{x}',t)\varphi(\vec{x}')dx'dt \\ &= \int_X l(\vec{x},\vec{x}')\varphi(\vec{x}')dx'\end{aligned}$$

yields $l(\vec{x},\vec{x}') = \int_T A_i(\vec{x},t)A_i(\vec{x}',t)dt$ which is the spatial correlation function.

Theorem A.6. *There exists a decomposition of the signal $A_i(\vec{x},t)$ such that*

$$A_i(\vec{x},t) = \sum_{k=0}^{\infty}\alpha^k\varphi^k(\vec{x})\Psi_i^k(t) \tag{2.3}$$

with

$$\alpha^0 \geq \alpha^1 \geq ... > 0$$

$$\lim_{N\to\infty}\alpha^N = 0$$

$$(\varphi^k,\varphi^l) = (\mathbf{\Psi}^k,\mathbf{\Psi}^l) = \delta_{kl}.$$

Proof. For S being a self-adjoint operator, [6] (theorem VI.3.2) shows its spectral

decomposition to be

$$S = U^*U = \sum_{k=0}^{\infty} (\alpha^k)^2 (\cdot, \varphi^k)\varphi^k \tag{2.4}$$

from which follows that

$$S\varphi^k = U^*U\varphi^k = (\alpha^k)^2\varphi^k \tag{2.5}$$

due to the orthonormality of $(\varphi^k, \varphi^k) = 1$. It is apparent that φ^k are the eigenfunctions of S associated with the eigenvalues $(\alpha^k)^2$.

Introducing a function

$$\Psi_i^k = (\alpha^k)^{-1}(U\varphi^k)_i \tag{2.6}$$

orthonormality of $\mathbf{\Psi}^k$ in $L^2(\mathbf{T})$ can be shown as follows:

$$\begin{aligned}
(\mathbf{\Psi}^k, \mathbf{\Psi}^l) &= (\alpha^k)^{-1}(\alpha^l)^{-1}((U\varphi^k)_i, (U\varphi^l)_i) \\
&= (\alpha^k)^{-1}(\alpha^l)^{-1}((U^*U\varphi^k), \varphi^l) \\
&= (\alpha^k)^{-1}(\alpha^l)^{-1}((\alpha^k)^2\varphi^k, \varphi^l) \\
&= \alpha^k(\alpha^l)^{-1}(\varphi^k, \varphi^l) \\
&= \delta_{kl}.
\end{aligned}$$

A spectral decomposition of the operator

$$U = \sum_{k=0}^{\infty} \alpha^k (\cdot, \varphi^k)\Psi_i^k \tag{2.7}$$

can be shown by recalling Eqn. (2.4) together with $(\alpha^k)^2\varphi^k = U^*U\varphi^k$ Eqn. (2.5) and

the definition $\Psi_i^k \alpha^k = (U\varphi^k)_i$ Eqn. (2.6).

$$\begin{aligned}
U^*U &= \sum_{k=0}^{\infty} (\alpha^k)^2 (\cdot, \varphi^k)\varphi^k \\
U^*U &= \sum_{k=0}^{\infty} U^*U\varphi^k (\cdot, \varphi^k) \\
\int_T A_i(\vec{x}, t) U dt &= \sum_{k=0}^{\infty} \int_T A_i(\vec{x}, t)(U\varphi^k)_i (\cdot, \varphi^k) dt \\
\int_T A_i(\vec{x}, t) U dt &= \int_T A_i(\vec{x}, t) \sum_{k=0}^{\infty} \alpha^k (\cdot, \varphi^k) \Psi_i^k dt
\end{aligned}$$

from which follows that $U = \sum_{k=0}^{\infty} \alpha^k (\cdot, \varphi^k) \Psi_i^k$ and furthermore:

$$\begin{aligned}
(U\varphi)_i(t) &= \sum_{k=0}^{\infty} \alpha^k (\varphi, \varphi^k) \Psi_i^k(t) \\
&= \int_X \sum_{k=0}^{\infty} \alpha^k \varphi(\vec{x}) \varphi^k(\vec{x}) \Psi_i^k(t) dx.
\end{aligned}$$

Using the original definition of U from Eqn. (2.1) for the left hand side yields

$$\int_X A_i(\vec{x}, t)\varphi(\vec{x}) dx = \int_X \sum_{k=0}^{\infty} \alpha^k \varphi^k(\vec{x}) \Psi_i^k(t) \varphi(\vec{x}) dx$$

for which a kernel identification results in theorem A.6.

Remark A.7. To compute the time eigenfunctions, an eigenvalue problem involving the operator R needs to be solved. This can be shown by starting from Eqn. (2.7)

and using Proposition A.5.

$$\begin{aligned}
U &= \sum_{k=0}^{\infty} \alpha^k(\cdot, \varphi^k)\Psi_i^k \\
UU^* &= \sum_{k=0}^{\infty} \alpha^k((U^*\cdot), \varphi^k)\Psi_i^k \\
&= \sum_{k=0}^{\infty} \alpha^k(\cdot, (U\varphi^k))\Psi_i^k \\
&= \sum_{k=0}^{\infty} (\alpha^k)^2(\cdot, \Psi_i^k)\Psi_i^k \\
(R\mathbf{\Psi}^k)_{i(t)} &= (\alpha^k)^2\Psi_i^k(t) \\
\int_T r_{ij}(t,t')\Psi_j^k(t')dt' &= (\alpha^k)^2\Psi_i^k(t)
\end{aligned}$$

The time integral on the left hand side can be approximated numerically and written in matrix form so that the entire expression can be treated with standard numerical eigenproblem solvers. In case the intergration is approximated with a quadrature function $w(t')$, it has to be applied in a manner that preserves symmetry of the correlation matrix $r_{ij}(t,t')$:

$$\begin{aligned}
r_{ij}(t,t')\Psi_j^k(t')w(t') &= (\alpha^k)^2\Psi_i^k(t) \\
\sqrt{w(t')}r_{ij}(t,t')\sqrt{w(t)}\chi_j^k(t') &= (\alpha^k)^2\chi_i^k(t)
\end{aligned}$$

The eigenproblem solution will provide the new basis functions $\chi_i^k(t) = \Psi_i^k(t)\sqrt{w(t)}$ which have tp be devided by the square root of the weight to determine the desired solution $\Psi_i^k(t)$.

Similarily, the spatial eigenfunctions could be computed from the spatial correlation function. Since this is not feasible in some cases, a projection of the time funtion

set on the signal yields the same result when starting from Eqn. (2.5).

$$\begin{aligned} U^*U\varphi^k &= (\alpha^k)^2\varphi^k \\ U^*\alpha^k\mathbf{\Psi}^k &= (\alpha^k)^2\varphi^k \\ \int_T A_i(\vec{x},t)\Psi_i^k(t)dt &= \alpha^k\varphi^k(\vec{x}) \end{aligned} \tag{2.8}$$

Note that the spatial eigenfunctions resulting from solving the left hand side need to be normalized in a way to preserve orthonormality by deviding with the square root of the inner product and disregarding α^k. The appropriate basis function scaling for reduced order representations can also be obtained by combining Eqn. (2.8) and Eqn. (2.3):

$$A_i(\vec{x},t) = \sum_{k=0}^{\infty}\int_T A_i(\vec{x},t)\Psi_i^k(t)dt\Psi_i^k(t) \tag{2.9}$$

Remark A.8. The scalar eigenfunction $\varphi(x)$ will not satisfy continuity or match boundary conditions, for example no slip at walls. But because φ at the wall contains only the temperature contribution of the original data set (see Eqn. (2.8)), examining the decomposed surface temperature is still possible and of the most interest in this study. Another way to look at the resulting function sets is to see the spatial eigenfunctions as flow energy (originating from kinetic and thermal sources lumped together) and the time eigenfunctions to ressemble its component-wise time behavior.

Proposition A.9. *The global energy of the signal, given by the square norm in* $L^2(X\times\mathbf{T})$*, equals the sum of eigenvalues as defined in decomposition Eqn. (2.3).*

$$E_{(\mathbf{A})} = \int_X\int_T A_i(\vec{x},t)A_i(\vec{x},t)dtdx = \sum_{k=0}^{\infty}(\alpha^k)^2$$

Proof. Applying orthogonality of the time and space eigenfunctions as well as decom-

position Eqn. (2.3), Proposition A.9 can readily be shown.

$$\begin{aligned} E_{(\mathbf{A})} &= \sum_{k=0}^{\infty} \alpha^k \int_X \varphi^k(\vec{x}) \int_T A_i(\vec{x},t)\Psi_i^k(t)dtdx \\ &= \sum_{k=0}^{\infty} \alpha^k \sum_{l=1}^{\infty} \alpha^l \int_X \varphi^k(\vec{x})\varphi^l(\vec{x})dx \int_T \Psi_i^k(t)\Psi_i(t)^l dt \\ &= \sum_{k=0}^{\infty} \alpha^k \sum_{l=1}^{\infty} \alpha^l \delta_{lk}\delta_{lk} \\ &= \sum_{k=0}^{\infty} (\alpha^k)^2 \end{aligned}$$

Remark A.10. The spatial and temporal energy, as the sum of eigenvalues multiplied with the squared time or space function sets, respectively, can be derived in a similar fashion.

$$\begin{aligned} \int_X A_i(\vec{x},t)A_i(\vec{x},t)dx &= \sum_{k=0}^{\infty} (\alpha^k)^2 \Psi_i^k(t)\Psi_i^k(t) \\ \int_T A_i(\vec{x},t)A_i(\vec{x},t)dt &= \sum_{k=0}^{\infty} (\alpha^k)^2 \varphi^k(\vec{x})\varphi^k(\vec{x}) \end{aligned}$$

2. Conclusion

It was shown that a real signal $A_i(\vec{x},t) \in L^2(X \times \mathbf{T})$ can be decomposed into a sumproduct of scalar space eigenfunctions and vectorial time eigenfunctions such that these functions are orthonormal in $L^2(X)$ and $L^2(\mathbf{T})$, respectively, and are coupled with the same eigenvalue. The time eigenfunctions can be calculated from a tensorial time correlation function and the spatial eigenfunctions by projection of time eigenfunctions on the signal. The eigenvalues ressemble the global signal energy, from which can be concluded that the proposed decomposition is also optimal in a sense that the least possible amount of eigenfunction pairs is required to rebuild a given

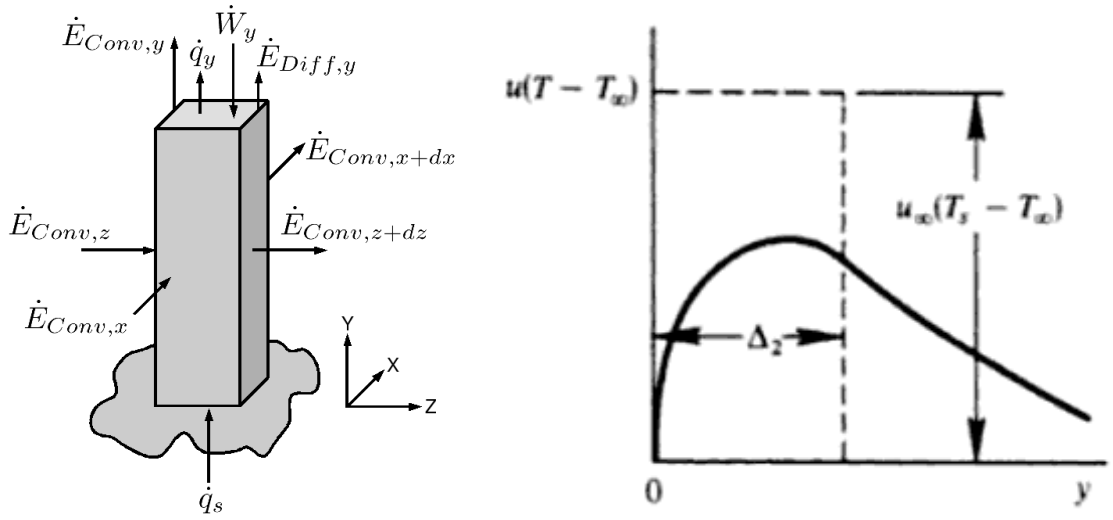

(a) (b)

Fig. 2.: The left plot, (a), shows a control volume, the right figure, (b), visualizes the meaning of enthalpy thickness, taken from Kays et al. (2005) [7].

fraction of the global signal energy.

B. Heat transfer evaluation

1. Integral energy balance

For a 3-dimensional, cubic control volume on a flat surface as shown in Fig. 2(a), the energy balance can be written as:

$$\begin{aligned} \dot{E}_{Conv,x} + \dot{E}_{Conv,z} \quad &+ \quad \dot{q}_s + \dot{W}_Y \\ = \dot{E}_{Conv,x+dx} + \dot{E}_{Conv,z+dz} \quad &+ \quad \dot{E}_{Diff,Y} + \dot{q}_Y + \dot{E}_{Conv,Y}. \end{aligned} \tag{2.10}$$

If Y is sufficiently larger than the boundary layer thickness of an external flow ($Y \rightarrow \infty$), all variables at Y will approach their local free stream values. In computations

of internal flows, this is also the case when symmetry is assumed (for example when a symmetry midplane is a boundary of the domain) and y reaches from the wall to the symmetry plane. We also assume that all turbulent fluxes on this boundary can be neglected compared to those at the wall, thus only the streamwise (x) and pitch wise (z) variables, as well as the surface wall heat flux are significant. Additionally, the contribution of the following terms is neglected:

$$\dot{W}_{\infty} = 0 \tag{2.11}$$

$$\dot{E}_{Diff,\infty} = 0 \tag{2.12}$$

$$\dot{q}_{\infty} = 0 \tag{2.13}$$

$$\dot{E}_{Conv,\infty} = 0. \tag{2.14}$$

As proposed in Kays et al. (2005) [7], the energy fluxes will be expressed in terms of stagnation enthalpy,

$$i_{ref} = (h + \frac{1}{2}\mathbf{U}^2) - (h_{\infty} + \frac{1}{2}\mathbf{U}_{\infty}^2), \tag{2.15}$$

where the reference datum is the local free stream stagnation enthalpy. With further assumptions of:

- Constant specific heat
- Perfect gas
- Low-speed flow (no kinetic energy contribution to enthalpy)
- No chemical reactions,

the stagnation enthalpy becomes

$$h_{ref} = c_p(T - T_{\infty}). \tag{2.16}$$

Replacing the terms in Eqn. (2.10) with the flux of h_{ref},

$$\dot{E}_{Conv,x} = dz \int_0^Y \rho u h_{ref} dy \tag{2.17}$$

$$\dot{E}_{Conv,x+dx} = dz \int_0^Y \rho u h_{ref} dy + dz \frac{\partial}{\partial x} \left(\int_0^Y \rho u h_{ref} dy \right) dx \tag{2.18}$$

$$\dot{E}_{Conv,z} = dx \int_0^Y \rho w h_{ref} dy \tag{2.19}$$

$$\dot{E}_{Conv,z+dz} = dx \int_0^Y \rho w h_{ref} dy + dx \frac{\partial}{\partial z} \left(\int_0^Y \rho w h_{ref} dy \right) dz \tag{2.20}$$

$$\dot{q}_s = \dot{q}_s'' dz dx, \tag{2.21}$$

the following simplified energy balance is obtained:

$$\dot{q}_s'' = \frac{\partial}{\partial x} \int_0^Y \rho u h_{ref} dy + \frac{\partial}{\partial z} \int_0^Y \rho w h_{ref} dy. \tag{2.22}$$

We now define two enthalpy thicknesses (for the physical significance see Fig. 2(b)):

$$\Delta_{2,u} = \int_0^\infty \frac{u}{u_\infty} \left(\frac{T - T_\infty}{T_s - T_\infty} \right) dy \tag{2.23}$$

$$\Delta_{2,w} = \int_0^\infty \frac{w}{u_\infty} \left(\frac{T - T_\infty}{T_s - T_\infty} \right) dy. \tag{2.24}$$

Assuming incompressible flow, letting $Y \to \infty$ and using the chain rule of derivatives, Eqn. (2.22) can be rewritten in terms of the enthalpy thicknesses (an exemplary calculation is given in Appendix A).

$$\begin{aligned} \frac{\dot{q}_s''}{\rho u_\infty c_p (T_s - T_\infty)} = & \frac{\partial \Delta_{2,u}}{\partial x} + \frac{\partial \Delta_{2,w}}{\partial z} \\ & + \Delta_{2,u} \left(\frac{1}{u_\infty} \frac{\partial u_\infty}{\partial x} + \frac{1}{T_s - T_\infty} \frac{\partial (T_s - T_\infty)}{\partial x} \right) \\ & + \Delta_{2,w} \left(\frac{1}{u_\infty} \frac{\partial u_\infty}{\partial z} + \frac{1}{T_s - T_\infty} \frac{\partial (T_s - T_\infty)}{\partial z} \right) \end{aligned} \tag{2.25}$$

or

$$\dot{q}''_s = \frac{\partial}{\partial x}[\Delta_{2,u}\rho c_p u_\infty(T_s - T_\infty)] + \frac{\partial}{\partial z}[\Delta_{2,w}\rho c_p u_\infty(T_s - T_\infty)] \tag{2.26}$$

$$\rho c_p u_\infty(T_s - T_\infty) = \dot{q}''_{\phi,s}. \tag{2.27}$$

The term $\rho c_p u_\infty(T_s - T_\infty)$ has units of W/m^2 and can be thought of as a potential heat flux available for surface heat transfer contained in the flow. Surface heat transfer is thus determined by the spatial change (gradient) of this "available heat flux" $\dot{q}''_{\phi,s}$ multiplied with the enthalpy thickness. Wherever the spatial enthalpy thickness change is high, the surface heat transfer will be elevated as well for given values of u_∞, T_s and T_∞.

Eqn. (2.26) can be further simplified by introducing an enthalpy thickness vector

$$\vec{\Delta}_2 = \Delta_{2,u}\vec{e}_x + \Delta_{2,w}\vec{e}_z \tag{2.28}$$

with which one arrives at an equation similar to the divergence of a flow field:

$$\dot{q}''_s = \vec{\nabla} \cdot (\vec{\Delta}_2 \dot{q}''_{\phi,s}). \tag{2.29}$$

As the goal is to evaluate modes of a turbulent flow, Reynolds decomposition ($u = \overline{u} + u'$, $v = \overline{v} + v'$ and $T = \overline{T} + T'$) is now applied on every fluctuating part and the entire expression is averaged (see Appendix B for more detailed calculations). Note that $\dot{q}''_s$ is not included and all reference variables (T_s, T_∞ and u_∞) are constant and thus have no fluctuating part. After introducing the definition of turbulent enthalpy thickness (compare to Eqn. (2.23) and (2.24)),

$$\Delta^{\varsigma}_{2,u} = \int_0^\infty \frac{\overline{u'T'}}{u_\infty(T_s - T_\infty)} dy \tag{2.30}$$

$$\Delta^{\varsigma}_{2,w} = \int_0^\infty \frac{\overline{w'T'}}{u_\infty(T_s - T_\infty)} dy, \tag{2.31}$$

Eqn. (2.25) is written as:

$$\frac{\dot{q}''_s}{\rho u_\infty c_p (T_s - T_\infty)} = \frac{\partial(\Delta^\vartheta_{2,u} + \Delta^\varsigma_{2,u})}{\partial x} + \frac{\partial(\Delta^\vartheta_{2,w} + \Delta^\varsigma_{2,w})}{\partial z} + (\Delta^\vartheta_{2,u} + \Delta^\varsigma_{2,u}) \left(\frac{1}{u_\infty} \frac{\partial u_\infty}{\partial x} + \frac{1}{T_s - T_\infty} \frac{\partial (T_s - T_\infty)}{\partial x} \right) + (\Delta^\vartheta_{2,w} + \Delta^\varsigma_{2,w}) \left(\frac{1}{u_\infty} \frac{\partial u_\infty}{\partial z} + \frac{1}{T_s - T_\infty} \frac{\partial (T_s - T_\infty)}{\partial z} \right) \tag{2.32}$$

or in analogy to Eqn. (2.28) and (2.29)

$$\dot{q}''_s = \vec{\nabla} \cdot (\vec{\Delta}^\vartheta_2 \dot{q}''_{\phi,s}) + \vec{\nabla} \cdot (\vec{\Delta}^\varsigma_2 \dot{q}''_{\phi,s}). \tag{2.33}$$

2. Interpretation of enthalpy thicknesses

In order to better understand the significance of enthalpy thicknesses as introduced above, the Blasius solution of the one dimensional, laminar flat plate boundary layer with no pressure gradient and constant surface temperature is evaluated. Note that the transition to turbulence was neglected for the sake of simplification, but the Reynolds number based on streamwise distance x is well above the critical point for most of the values shown. As seen in Fig. 3, if the gradient of enthalpy thickness ($\partial \Delta_{2,u} / \partial x$) gets smaller, the heat transfer coefficient decreases and, for the case of constant $T_s - T_\infty$, surface heat flux reduces. The steeper the increase in enthalpy thickness, the higher is surface heat transfer. For a constant enthalpy thickness, the surface heat flux will be zero.

For turbulent flows, an enthalpy thickness based on fluctuations was introduced in Eqn. (2.30) and is combined with Eqn. (2.33) in one dimension for the sake of explanation:

$$\frac{\dot{q}''_s}{\rho c_p} = \frac{d}{dx} \left[\int_0^\infty \frac{\overline{u}(\overline{T} - T_\infty)}{u_\infty (T_s - T_\infty)} dy + \int_0^\infty \frac{\overline{u'T'}}{u_\infty (T_s - T_\infty)} dy \right] \tag{2.34}$$

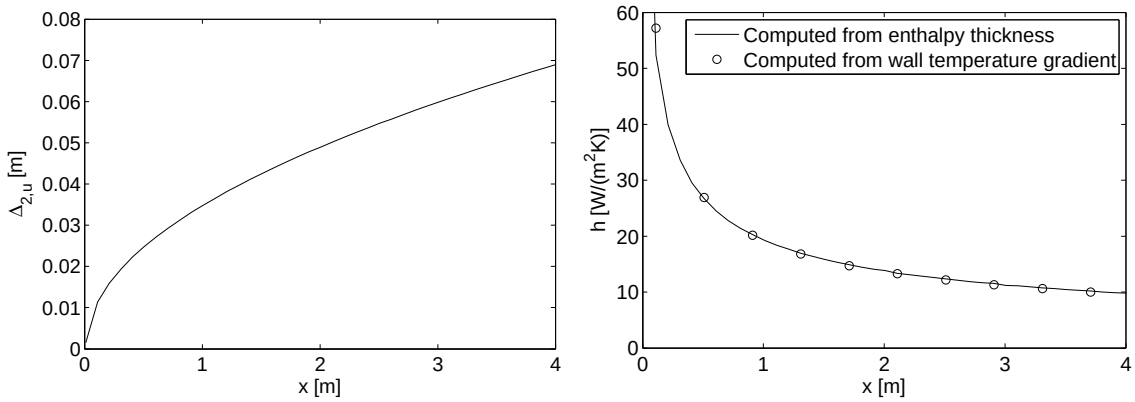

Fig. 3.: The left figure shows enthalpy thickness as function of streamwise distance from the leading edge of a flat plate boundary layer with constant surface temperature and no pressure gradient. The Blasius solution (assuming no transition to turbulence) is used. For the right figure, heat transfer coefficient as function of streamwise distance is plotted. The surface heat flux is computed with using the gradient of enthalpy thickness (see Eqn. (2.29) for one dimension) and the Fourier conduction law.

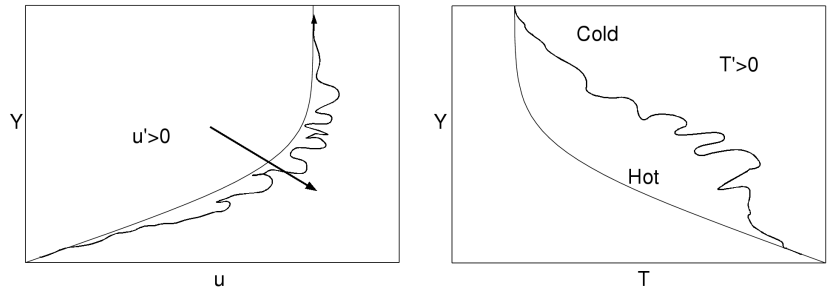

(a) (b)

Fig. 4.: The plots show mean velocity and temperature profiles with superimposed fluctuations for a flat plate boundary layer with constant surface temperature.

Assuming a situation where the flow has no fluctuations at one point but $\overline{u'T'} > 0$ along dx and furthermore all time averaged values do not change (short time step), enthalpy thickness and subsequently heat transfer will increase according to the above conclusions from laminar flow. One such combination of u' and T' is shown schematically in Fig. 4 for the case of a heated surface. If $u' > 0$ (Fig. 4(a)), comparable to an accelerated boundary layer, a flow velocity towards the surface is induced to compensate for the mass flux defficiency closer to the surface. For negative velocity fluctuations, which is comparable to an adverse pressure gradient, the boundary layer develops a concave dent and a velocity component away from the surface is induced. Considering $\overline{u'T'} > 0$ by merging Fig. 4(a) and Fig. 4(b), cooler fluid from the mean flow is convected towards the wall, into a zone of high temperature due to $T' > 0$. Mixing is now enhanced, and so is surface heat transfer.

3. Evaluation of OD modes

a. Heat exchangers

In most heat exchange applications (internal blade cooling in gas turbines, for example), turbulence is enhanced to increase surface heat transfer in terms of the heat transfer coefficient. For computing such problems, one defines either the wall heat flux or the surface temperature as a constant given boundary condition. The evaluation procedure developed in the following is valid for both cases.

Eqn. (2.33) is rewritten using the definitions of enthalpy thickness and available heat flux:

$$\begin{aligned} \dot{q}_s'' &= \vec{\nabla}\cdot(\vec{\Delta}_2^{\vartheta}\dot{q}_{\phi,s}'') + \vec{\nabla}\cdot(\vec{\Delta}_2^{\varsigma}\dot{q}_{\phi,s}'') \\ &= \frac{\partial}{\partial x}\int_0^{\infty}\rho\overline{u}c_p(\overline{T}-T_\infty)\,dy + \frac{\partial}{\partial z}\int_0^{\infty}\rho\overline{w}c_p(\overline{T}-T_\infty)\,dy \\ &+ \frac{\partial}{\partial x}\int_0^{\infty}\rho c_p\overline{u'T'}\,dy + \frac{\partial}{\partial z}\int_0^{\infty}\rho c_p\overline{w'T'}\,dy \end{aligned} \tag{2.35}$$

The right hand side can be expressed in terms of orthogonal basis functions, exemplarily shown for the first flucutating term on the right hand side:

$$\frac{\partial}{\partial x}\int_0^{\infty}\rho c_p\overline{u'T'}\,dy = \frac{\partial}{\partial x}\int_0^{\infty}\overline{\left(\rho\sum_{k\neq 0}\alpha^k\Psi_u^k(t)\varphi^k(\vec{x})\right)\left(c_p\sum_{l\neq 0}\alpha^l\Psi_T^l(t)\varphi^l(\vec{x})\right)}\,dy, \tag{2.36}$$

where modes with $k,l = 0$ represents the mean and the ones with $k,l \neq 0$ the fluctations.

If the wall heat flux is given as a constant boundary condition, the sum of all higher order modes will be zero for all points in space and time. A ranking of mode pairs in terms of their contribution to the left hand side will then allow for a qualitative assessment of their importance with respect to turbulent heat transfer. If an assessment of modes averaged over an area of interest (the stagnation region of a

body in crossflow, for example) is of greater interest than the *local* OD mode ranking, which is the outcome of the evaluation of Eqn. (2.36), Eqn. (2.33) can be integrated over the surface and simplified using Gauss' divergence theorem.

$$\begin{aligned}
\int_S \dot{q}''_s dS &= \int_S \vec{\nabla}\cdot(\vec{\Delta}_2^{\vartheta}\dot{q}''_{\phi,s})dS + \int_S \vec{\nabla}\cdot(\vec{\Delta}_2^{\varsigma}\dot{q}''_{\phi,s})dS \\
\dot{q}_s &= \oint_L (\vec{\Delta}_2^{\vartheta}\dot{q}''_{\phi,s})\cdot\vec{n}\,dL + \oint_L (\vec{\Delta}_2^{\varsigma}\dot{q}''_{\phi,s})\cdot\vec{n}\,dL \\
&= \oint_L \left[\int_0^\infty \rho\overline{u}c_p(\overline{T}-T_\infty)\,dy\right]\vec{e}_x\cdot\vec{n}\,dL \\
&+ \oint_L \left[\int_0^\infty \rho\overline{w}c_p(\overline{T}-T_\infty)\,dy\right]\vec{e}_z\cdot\vec{n}\,dL \\
&+ \oint_L \left[\int_0^\infty \rho c_p\overline{u'T'}\,dy\right]\vec{e}_x\cdot\vec{n}\,dL + \oint_L \left[\int_0^\infty \rho c_p\overline{w'T'}\,dy\right]\vec{e}_z\cdot\vec{n}\,dL
\end{aligned} \tag{2.37}$$

As in Eqn. (2.36), the unnormalized enthalpy thickness terms can be expressed with OD modes. This procedure is computationally much more tractable since no derivatives have to be computed and the integrals only need to be evaluated along the lines enclosing the area of interest. For a square area defined on the x,z-plane with four edges (West, North, East, South), inserting OD modes and neglecting the averages (mode 0), the right hand side is rewritten as:

$$\begin{aligned}
&- \int_W \left[\int_0^\infty \overline{(\rho\alpha^k\Psi_u^k(t)\varphi^k(\vec{x}))\left(c_p\alpha^l\Psi_T^l(t)\varphi^l(\vec{x})\right)}\,dy\right]dL \\
&+ \int_E \left[\int_0^\infty \overline{(\rho\alpha^k\Psi_u^k(t)\varphi^k(\vec{x}))\left(c_p\alpha^l\Psi_T^l(t)\varphi^l(\vec{x})\right)}\,dy\right]dL \\
&+ \int_N \left[\int_0^\infty \overline{(\rho\alpha^k\Psi_w^k(t)\varphi^k(\vec{x}))\left(c_p\alpha^l\Psi_T^l(t)\varphi^l(\vec{x})\right)}\,dy\right]dL \\
&- \int_S \left[\int_0^\infty \overline{(\rho\alpha^k\Psi_w^k(t)\varphi^k(\vec{x}))\left(c_p\alpha^l\Psi_T^l(t)\varphi^l(\vec{x})\right)}\,dy\right]dL
\end{aligned} \tag{2.38}$$

The result of this expression will provide an estimate of how much the particular mode combination k/l contributes to wall heat flux.

b. Adiabatic surface with no heat flux

In certain cases, one assumes adiabatic walls with no heat flux ($\dot{q}''_s = 0$) and inflows with different temperatures (film cooling holes in gas turbine experiments or simulations for example). The design goal is to have as little convective energy tranport within the boundary layer as possible, so the average temperature difference between wall und free stream hot gas path remains large. This does not imply higher surface heat transfer since the surface is adiabatic. High fluctuations or gradients of fluctuations increase mixing within the thermal boundary layer, which is undesired. Under these circumstances, the energy balance (Eqn. (2.33)) is rewritten as a balance of divergence in vector fields:

$$\vec{\nabla} \cdot (\vec{\Delta}_2^{\vartheta} \dot{q}''_{\phi,s}) = -\vec{\nabla} \cdot (\vec{\Delta}_2^{\varsigma} \dot{q}''_{\phi,s}) \tag{2.39}$$

$$\begin{aligned} \dot{q}''_{\phi,s} \frac{\partial \Delta^{\vartheta}_{2,u}}{\partial x} + \Delta^{\vartheta}_{2,u} \frac{\partial \dot{q}''_{\phi,s}}{\partial x} + \dot{q}''_{\phi,s} \frac{\partial \Delta^{\vartheta}_{2,w}}{\partial z} + \Delta^{\vartheta}_{2,w} \frac{\partial \dot{q}''_{\phi,s}}{\partial z} = \\ = -\left[\dot{q}''_{\phi,s} \frac{\partial \Delta^{\varsigma}_{2,u}}{\partial x} + \Delta^{\varsigma}_{2,u} \frac{\partial \dot{q}''_{\phi,s}}{\partial x} + \dot{q}''_{\phi,s} \frac{\partial \Delta^{\varsigma}_{2,w}}{\partial z} + \Delta^{\varsigma}_{2,w} \frac{\partial \dot{q}''_{\phi,s}}{\partial z} \right] \end{aligned} \tag{2.40}$$

$$\dot{q}''_{\phi,s} = \frac{-\left[(\Delta^{\vartheta}_{2,u} + \Delta^{\varsigma}_{2,u}) \frac{\partial \dot{q}''_{\phi,s}}{\partial x} + (\Delta^{\vartheta}_{2,w} + \Delta^{\varsigma}_{2,w}) \frac{\partial \dot{q}''_{\phi,s}}{\partial z} \right]}{\frac{\partial \Delta^{\vartheta}_{2,u}}{\partial x} + \frac{\partial \Delta^{\vartheta}_{2,w}}{\partial z} + \frac{\partial \Delta^{\varsigma}_{2,u}}{\partial x} + \frac{\partial \Delta^{\varsigma}_{2,w}}{\partial z}} \tag{2.41}$$

To maintain a high difference between cooled surface and mean flow ($\dot{q}''_{\phi,s}$ is a large negative number), the denominator ($\vec{\nabla} \cdot \vec{\Delta}_2^{\vartheta} + \vec{\nabla} \cdot \vec{\Delta}_2^{\varsigma}$) of this equation needs to be small and the sum of terms within the brackets of the numerator needs to be large and positive. For the further analysis, only the denominator is considered since the numerator can be thought of as a feedback (gradients of $\dot{q}''_{\phi,s}$ will obviously cause changes in its absolute value).

In orthogonal decomposition analysis, the first mode ($k, l = 0$) represents the average and fluctuating parts are expressed by higher order modes. The gradient of enthalpy thickness due to fluctuations (last two terms in Eqn. (2.41)) is exemplarily

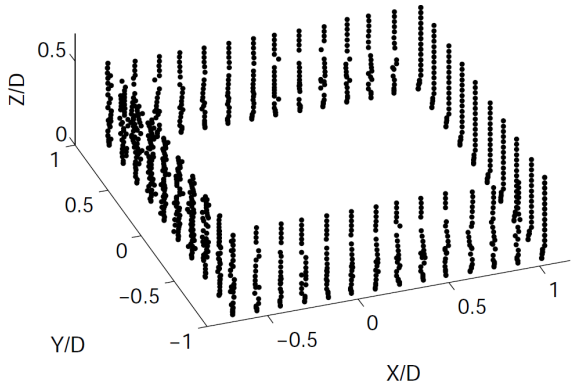

Fig. 5.: Line points extrapolated from an unstructured grid.

for one direction written as:

$$\frac{\partial \Delta_{2,u}^{\varsigma}}{\partial x} = \frac{\partial}{\partial x} \frac{\int_0^{\infty} \overline{\left(\sum_{k\neq 0} \alpha^k \Psi_u^k(t)\varphi^k(\vec{x})\right)\left(\sum_{l\neq 0} \alpha^l \Psi_T^l(t)\varphi^l(\vec{x})\right)} dy}{u_{\infty}(T_s - T_{\infty})}. \tag{2.42}$$

To identify flow subsets or structures that are most disruptive to the boundary layer, one seeks for mode combinations that minimize this expression in all directions $(\vec{\nabla} \cdot \vec{\Delta}_2^{\varsigma})$.

Ranking the OD modes in reference to an area of interest using Gauss' divergence theorem after integrating Eqn. (2.41) will not be as advantageous as it was in the previous section due to the fraction on the right hand side. The treatment of adiabatic surfaces with zero wall heat flux will thus remain restricted to a local evaluation.

c. Evaluating finite volume computations on unstructured grids

If data from computational simulations on unstructured grids are analyzed with this methodolgy, some practical implications need to be considered. Some error is introduced, for example, when the grid point data along certain lines for computing the

integrals in Eqn. (2.38) are obtained in a post-processing step without interpolation and, due to asymmetry in the unstructured grid, will not line up exactly with the desired line profiles. An example is seen in Fig. 5, where the points on edge W (left side) are located within an area of relatively high mesh non-uniformity. If the temperature data were normalized and weighted to build orthogonal basis functions, for example such that

$$\mathfrak{T}(\vec{x},t) = Ec\frac{T(\vec{x},t) - \overline{T_{in}}}{\overline{T_{out}} - \overline{T_{in}}} \tag{2.43}$$

$$Ec = \frac{U_0^2}{c_v(\overline{T_{out}} - \overline{T_{in}})}, \tag{2.44}$$

correct scaling of variables of the reduced order model will be achieved by adding the inlet temperature only to the average mode:

$$T(\vec{x},t) = \frac{\alpha^0\Psi^0_{\mathfrak{T}}(t)\varphi^0(\vec{x})}{Ec}(\overline{T_{out}} - \overline{T_{in}}) + \overline{T_{in}} + \sum_{k\neq 0}\frac{\alpha^k\Psi^k_{\mathfrak{T}}(t)\varphi^k(\vec{x})}{Ec}(\overline{T_{out}} - \overline{T_{in}}) \tag{2.45}$$

CHAPTER III

ORTHOGONAL DECOMPOSITION OF STATIC WALL PRESSURE DATA

A. Introduction

Axial compressors are limited in their range of operation by dynamic instabilities. To prevent these instabilities from occuring, high saftey margins have to be imposed, not allowing to use the peak pressure rise as an operating point (Greitzer (2007) [8]). This yields an optimization potential that makes investigating the occurance and development of instability a worthwhile endeavor.

A commonly observed feature of dynamic instabilities is rotating stall. When fully developed, it causes the overall pressure ratio to drop significantly and induces vibrations that can destroy the compressor. Two types of stall can be destinguished: large scale (or modal) and small scale (or spike type). The former has been investigated by Camp and Day (1998) [9] and the latter by Vo et al. (2008) [10], for example. The large scale instabilities can be examined without spatially resolving the blades since thay scale on the annulus diameter. Spike type inception, however, is characterized by scales smaller than the blade passage and thus require high spatial resolution when conducting experiments or simulations. The numerical investigations of the latter by Vo et al. (2008) [10] for low speed compressors propose two precursors for stall inception related to the tip leakage flow: spillage of the leakage flow upstream of the leading edge and backflow of tip clearance fluid at the trailing edge. For transonic compressors, the interaction of the shock front and the tip clearance flow complicates the picture. In a numerical study of a transonic compressor, Hah et al. (2006) [11] show that this interaction is inherently unsteady and the overall unsteadiness in wall pressure much larger than that due to only the shock front.

Unfortunately, the flow within the blade passage is not easily accessible experimentally. Static wall pressure measurements at the casing, in turn, allow some insight into the near wall flow field. Since only a few rotor revolutions are sufficient for the stall cell to develop fully, pressure data have to be obtained at very high sampling rates, leading to a large amount of data very rich in dynamics. An example for spectral analyses performed in terms of Fourier Transformation is given in Biela et al. (2008) [12]. The compressor was operated in transient mode in that it was driven into the stall regime while casing mounted static pressure probes recorded the wall pressure. From the Fourier analysis, the authors concluded that a frequency band excitation occurs which is only observed near the tip clearance vortex.

To make use of optimal basis functions instead of sine functions, we apply proper orthogonal decomposition (POD) to the data obtained from a transonic single stage compressor test rig at TU Darmstadt. This method has been used to examine turbulent flow data, for example in Ball et al. (1991) [13]. They applied POD to data from direct numerical simulation of channel flow in order to understand bursting and sweeping events in the internal turbulent boundary layer. Later, Duggleby et al. (2009) [14] used the same methodology on a direct numerical turbulent pipe flow simulation. Certain flow structures in the boundary layer were linked to basis functions and the energy transfer between them classified. Instead of computing the decomposition based on spatial correlations, Aubry et al. (1991) [4] show the equivalence of using time and space autocorrelations. An exemplarily application of the time based method is used in Handler et al. (2006) [5] who post process turbulent channel flow with polymer injection to explain drag reduction.

The experimental data used for this work were provided by collaborators at TU Darmstadt, Germany, see for example Biela at al. (2008) [12]. In their experiments, the rotor casing was staffed with 14 equally spaced pressure probes, aligned in the flow

direction and sampled at 125 kHz. The sensors range from roughly one cord length upstream of the blade leading edge to the blade middle. In order to understand the meaning of the eigenfunctions provided by POD, measurements under steady-in-the-mean conditions at different operating points (peak efficiency, near stall and in between) were decomposed. The eigenfunctions are then projected onto the pressure field to yield a reduced order data set. Data with an unsteady mean were obtained by closing a valve downstream of the stage which increased the pressure ratio until stall was observed. This data were analyzed by performing POD on time bins before, at onset and during stall inception. For a detailed description of the experimental setup see Biela et al. (2008) [12].

B. Mathematical procedure

Proper orthogonal decomposition is, depending on the nature of the underlying data set, typically done in one of two ways: by solving a matrix equation based on spatial correlation (in the following referred to as DPOD) or temporal correlation (MoS). In general, the signal is decomposed into an optimal basis function set,

$$p(x,t) = \sum_{n=0}^{N=\infty} \lambda_n a_n(t) \Phi_n(x) \tag{3.1}$$

$$\max_{\Phi \in L^2} \frac{\langle |(p,\Phi)|^2 \rangle}{\|\Phi\|^2}, \tag{3.2}$$

where the spatial eigenfunctions $\Phi_n(x)$ with a corresponding eigenvalue λ_n are accompanied by their respective time-dependent coefficients $a_n(t)$. The fluctuating pressure p is calculated by substracting the time averaged pressure for every sensor signal $p(x,t) = P(x,t) - \langle P(x,t) \rangle$ and $\langle\rangle$ denotes the time average over all available samples. These functions are optimal in that the least number is required to rebuild a given sample of the data (reduced order model). When those basis functions are de-

rived from pressure signals, optimality does not refer to kinetic flow energy, which is the usual case when examining flow fields. Instead, the maximum value problem will be written as in Eqn. (3.2), which maximizes the dynamical information contained in an eigenfunction.

The experimental setup delivers data in one aperiodic spatial direction, sampled at 14 points and in time. With DPOD, this data is decomposed into 14 eigenfunctions $\Phi_n(x)$ as defined in Eqn. (3.1). The number of function sets (or POD modes) approximating infinity in Eqn. (3.1) and obtained by MoS is equivalent to the number of data samples in time (see Eqn. (3.7)). DPOD can be derived by applying variational calculus on Eqn. (3.2) in analogy to Holmes et al. (1996) [15], so that a Fredholm integral arises,

$$\int_\Omega K(x,x')\Phi_n(x')d\Omega = \lambda_n \Phi_n(x), \tag{3.3}$$

$$K(x,x') = \lim_{T\to\infty} \frac{1}{T} \int_0^T p(x,t)p(x',t)dt, \tag{3.4}$$

where x is the position vector in the (one dimensional) domain Ω. The kernel $K(x,x')$ is essentially a time averaged autocorrelation of pressure signals in the spatial direction. The integration in Eqn. (3.3) is numerically approximated by a trapezoidal quadrature and the resulting matrix equation solved as an eigenvalue problem. Time signals for every mode can be calculated by projecting the eigenfunctions onto the original data field, which yields

$$a_n(t) = \int_\Omega \Phi_n(x)p(x,t)d\Omega, \tag{3.5}$$

where $a_n(t)$ are time coefficients for particular eigenfunctions. Reduced order pressure fields are built using eigenvalues, time coefficients and spatial basis functions for any number of modes ($N < \infty$) according to Eqn. (3.1).

Similar to the eigenvalue problem in Eqn. (3.3), the time coefficients in the MoS are calculated first based on:

$$\int_T R(t,t')a_n(t')dt = \lambda_n a_n(t), \tag{3.6}$$

$$R(t,t') = \int_\Omega p(x,t)p(x,t')d\Omega. \tag{3.7}$$

As in Eqn. (3.5), the spatial basis function are obtained from projection.

C. Results

Both DPOD and MoS were used on data gathered from compressor operation at peak efficiency. Using DPOD, eigenfunctions were extracted from pressure fields with steady in the mean conditions taken at three different compressor operating points. The relation between basis functions and flow features is then examined. The time behavior of basis eigenfunctions was analyzed for transient compressor operation experiencing rotating stall. These results are presented in the last subsection.

1. MoS on data from operation at peak efficiency

Since there are more time observations (equals modes from the MoS) than pressure sensors in space (equals the number of modes from DPOD), the data was initially analyzed using the MoS. To be able to compare results to DPOD, the data were centered in time (p as defined above), where normally one would substract the spatial average for every time step. Only the first 14 modes have eigenvalues higher than machine precision. Thus, also when using the MoS only the first 14 modes will yield non-zero reduced order representations that can be used for further analysis. Fig. 6 shows convergence of the first 14 eigenvalues for different data sample sizes. It should be noted that all samples were spanning the same real time (dynamical history of

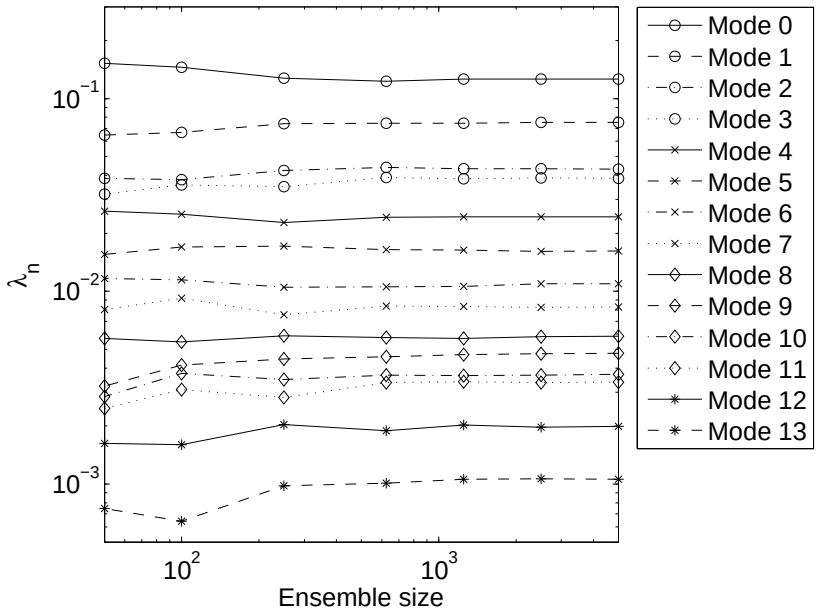

Fig. 6.: Shown are the first 14 eigenvalues from the MoS POD when performed on the same data set but with different sampling rates, yielding different sample sizes.

compressor operation), but to get smaller sample sizes the sampling frequency was reduced. For more than ~ 600 data points in time, there is no significant change of eigenvalues observable, especially in the lower order modes. The eigenvalues resulting from DPOD and Eqn. (3.3) were compared to MoS, Eqn. (3.6), and are exactly the same.

2. Steady operating point at peak efficiency

The pressure data was analyzed with DPOD over 40 rotor revolutions, which is roughly equivalent to 15150 data samples, for the next three subsections. At peak efficiency, the backpressure is relatively low so that the deflection of the vortex trajectory upstream towards the blade leading edge is less compared to near stall. Also,

the angle between vortex trajectory and shock front is closer to 90°, which lowers the impact on casing pressure fluctuations. This combined with the overall lower pressure fluctuations due to the shock itself makes it harder to distinguish between flow features and eigenfunctions. Consequently, the eigenvalue spectrum as shown in the figure on page 37 is more flat, but still decreases in a step after the forth mode, indicating that the first 4 modes contain the most important information. Also, the coupling of modes 0 and 1 with shock and blade induced pressure change, as well as 2 and 3 with tip vortices, seems justified. A reduced order field in analogy to the near stall case is presented in Fig. 7. The reduced order representation is rather poor, the shock far upstream of the blade for example seems not to be represented by any of the used modes. When comparing modes 0 and 1 with the reconstructed field (third from left), however, the footprint of the vortex trajectory seems to be captured since the low pressure region in the field reconstructed from mode 0 and 1 is more homogeneous.

For this system, Fourier transformations can only be performed on individual sensor signals. Extraction of information in the spatial direction with FFT is prohibitive. POD, in turn, delivers time signals that incorporate the dynamics of the entire system. For the peak efficiency case, the measured data was rather noisy. A spectral analysis is shown in Fig. 8, where the worst case sensor in terms of noise is depicted. Comparing the FFT spectrum of the sensor 7 signal with that of the mode 0 time coefficient $a_0(t)$, the spectrum appears relatively less noisy and peaks are clearly at the BPF and its harmonics. In this context, POD can be thought of as a signal filtering technique. At mode 3, the highest peak in the spectrum is not at the BPF. This is another indicator for the first two modes representing shock and blade induced pressure variations.

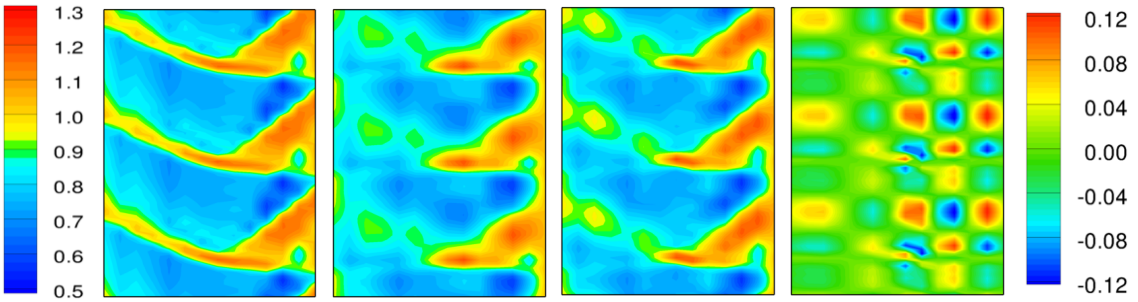

Fig. 7.: From left to right: Measured data at peak efficiency, normalized with total inlet pressure and ensemble averaged over almost 40 rotor revolutions. Summation of average pressure change, mode 0 and mode 1. Summation of average pressure change, mode 0, 1, 2 and 3. Summation of fluctuating pressure of mode 2 and 3.

3. Steady operating point in between peak efficiency and stall

The analysis of a slightly more throttled compressor stage, between peak efficiency and near stall, showed a differing behavior in terms of POD results. The eigenvalues dropped off after the 5th mode and were following a generally exponential trend. Thus, the first 5 modes were used for reduced order reconstruction, but no conclusions could be drawn which modes were to be combined. The spectral analysis showed that only mode 5 had the highest Fourier coefficient not at the BPF. Only the combination with mode 2 yields relatively flat eigenfunctions upstream of the blade leading edge. Comparing the reconstructed flow field in Fig. 9 to the peak efficiency case (Fig. 7), the overall reconstruction quality has significantly improved since shocks are more distinct in the measured data. The peaks in mode 2 and 4 are shifted upstream compared to their peak efficiency counterparts, indicating a deflection of the vortex trajectory towards the blade leading edge.

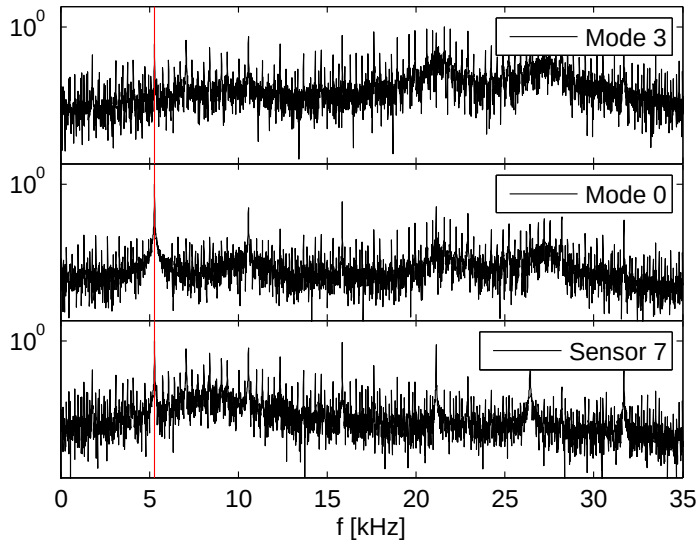

Fig. 8.: The spectra of Fourier coefficients, normalized by the maximum coefficient. The spectrum is obtained from the peak efficiency case, FFT of sensor 7 and time coefficients $a_0(t)$ and $a_3(t)$ are plotted. The first peak in mode 0 indicates the BPF at 5280 Hz (vertical line).

4. Steady operating point near stall

When the rotor is operated near the stability limit, the shock front is more distinct and has a wider impact on the casing pressure as compared to peak efficiency cases, which facilitates the interpretation of eigenfunctions. Fig. 10 shows the convergence of eigenvalues. The eigenvalue belonging to a particular eigenfunction is a measure of the dynamics contained within this eigenfunction as it is the average over the time fluctuations ($\lambda_n = \langle a_n^2(t) \rangle$). Since the first four modes contain the most flow information and a drop in the eigenvalue plot can be seen after the 4th mode, only the first four modes are condisidered in the following. For this system, a single one-dimensional eigenfuntion can not reproduce the flow patterns caused by the compressor blade

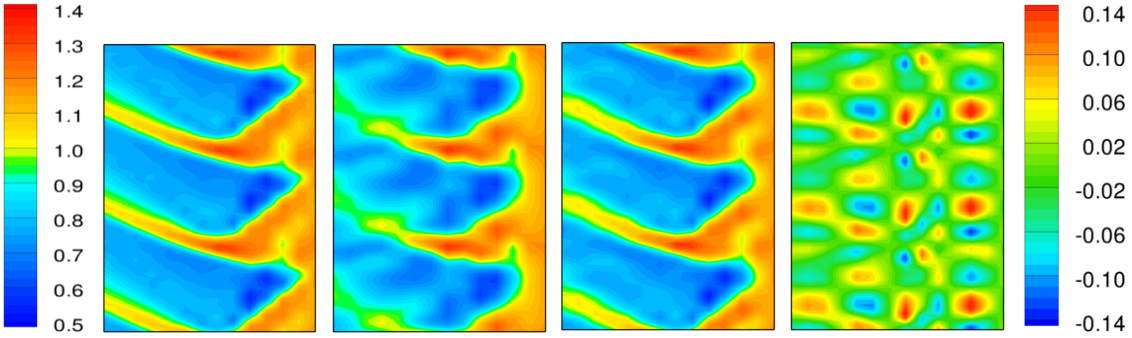

Fig. 9.: From left to right: Measured data between peak efficiency and stall, normalized with total inlet pressure and ensemble averaged over almost 40 rotor revolutions. Summation of average pressure change, mode 0, mode 1 and mode 3. Summation of average pressure change, mode 0, 1, 2, 3 and 4. Summation of fluctuating pressure of mode 2 and 4.

which is angled with respect to the spatial coordinate. As eigenfunctions are sorted in terms of their information content represented by the eigenvalue, we combine mode 0 and 1 as well as mode 2 and 3 to account for spatial gradients.

The time averaged measured data shows a significant pressure drop around sensors 9 and 10. An eigenfunction showing a peak at the same location belongs to mode 2. Its curve is rather flat for all other positions. A reconstructed pressure field for this mode is depicted in Fig. 11. The location of pressure drop in the compressor passage, caused by the shock and tip clearance vortex interaction, is identical with a significant peak in the time behavior of eigenfunction mode 2 (see Fig. 12). The effect of the tip vortex therefore can be linked to mode 2. The eigenfunction with the next lower eigenvalue $n = 3$ seems to contain the circumferencial gradient of the vortex signal.

Pressure fluctuations are dominanted by the shock waves originating upstream

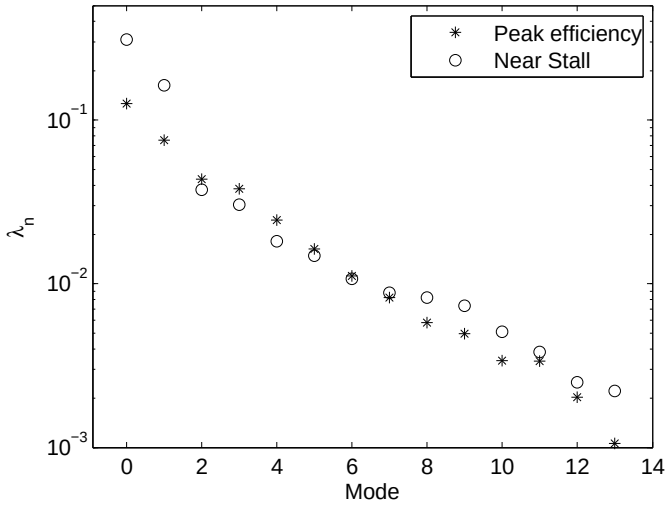

Fig. 10.: The eigenvalues represent how well a certain eigenfunction resembles the initial data. The first four eigenvalues seem to be dominant for both cases.

of the blade leading edge and the blade. Due to the large difference in magnitude of the first and second eigenvalue compared to the rest as shown in Fig. 10, the first two modes contain the major dynamics. Since they are the most important ones, they represent the change of pressure due to shocks and the blade itself. The result of this decomposition is shown in Fig. 13. Reducing the order of the system from 14 to 4 modes results in loss of information especially where steep gradients exist, for example at the edge of the shock wave, which appears to be smoother in the reconstructed data. Yet, all major flow features are captured. The low pressure region in the blade passage looks relatively homogeneous when only accounting for modes 0 and 1. The strong variations, as present in the original data from blade leading edge to approximatley a quarter of the chord, are mostly represented by modes 2 and 3. This is the region where the tip clearance vortex interacts whith the shock front and leaves its footprint on the wall pressure. The FFT spectrum of mode 2 shows the highest

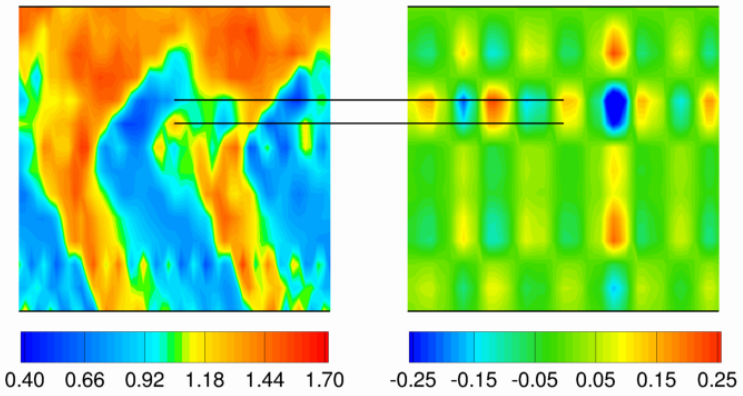

Fig. 11.: Instantaneous pressure normalized with total inlet pressure for an operating point near stall (left) and the respective reconstructed field of mode 2 (right), where only the fluctuating component is displayed. The black lines indicate the position of sensors 9 and 10. Note that the flow direction is from bottom to top and the blade rotates from right to left.

peak at twice the BPF and is the first mode where the peak at BPF is not the highest in the spectrum.

5. Transient operation with stall inception

Time bins for the transient POD were defined based on running averages of pressure data as shown in Fig. 14. The time bin size was chosen to be an integer multiple of sensor signals per entire blade passing cycle in order to get periodic data in time. Furthermore, starting points for POD were set so that one time bin is located in the middle of stall inception (C) and right on the edge of steady operation (B). POD analysis of bin A was obtained from data spanning about 840 revolutions in the fully steady regime. Since POD depends on statistical correlations, sufficient data needs to be included to achieve convergence of modes. This was assured by comparing

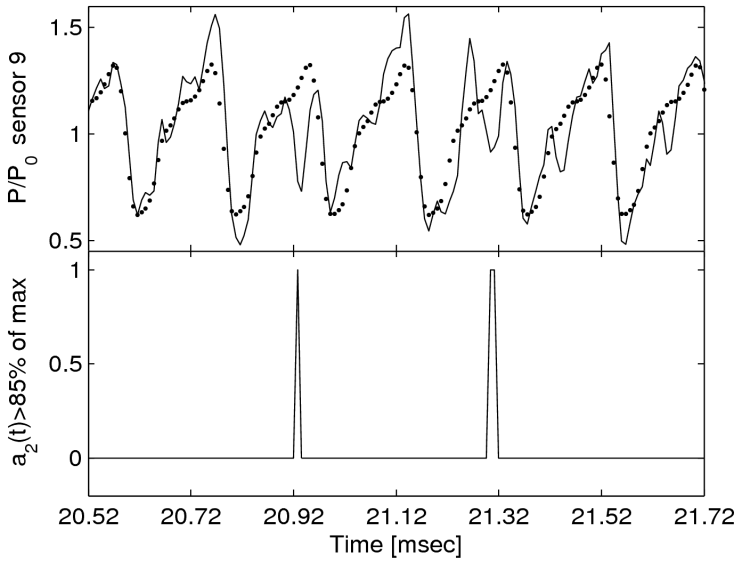

Fig. 12.: The top plot shows normalized pressure data of sensor 9 (solid black) and an FFT reconstruction of the same signal with 10 modes (dots). The bottom plot shows where the time coefficient of mode 2 exceeds a certain threshold for the same measurement time.

eigenvalues of the lower order modes from bin A and B, which yielded almost identical plots for the first 4 modes.

A comparison of eigenfunctions of mode 0 and 2 is shown in Fig. 15. The pressure variation due to shock waves as mapped by mode 0 remains almost unchanged. Among the first 4 modes, only the eigenfunction of mode 2 varies significantly from bin fully steady (A) to onset of stall inception (B). The peak at sensor position 10, where interaction between tip clearance vortex and shock front is the highest (Fig. 11), remains unchanged as well, but a higher peak occurs at sensor position 8. This the last sensor before the blade leading edge in streamwise direction. Further upstream, the eigenfunction seems to pick up some dynamics induced by the shock front, but the

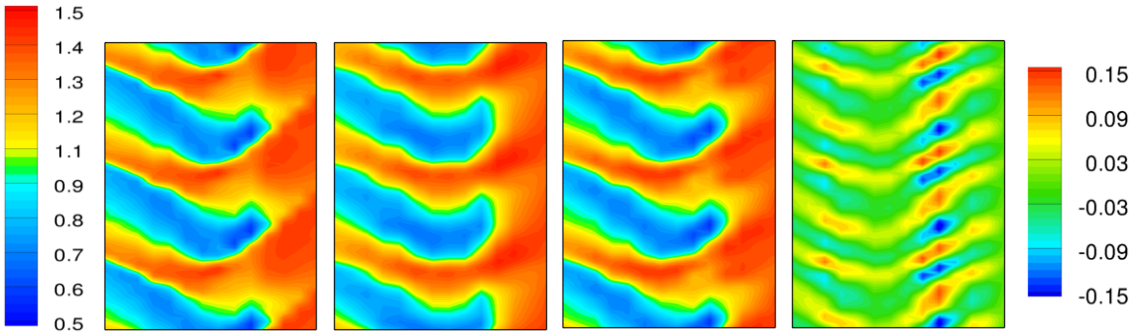

Fig. 13.: From left to right: Measured data at an operating point near stall, normalized with total inlet pressure and ensemble averaged over alomst 40 rotor revolutions. Summation of average pressure change, mode 0 and mode 1. Summation of average pressure change, mode 0, 1, 2 and 3. Summation of fluctuating pressure of mode 2 and 3.

magnitude remains 50% lower than the peak at position 8. During the development of the stall cell, bin C, the eigenfunction returns to its original shape except for positions 11, 12 and 13. The signal seems to weaken overall, indicating a less significant impact of the tip clearance vortex on the wall pressure. It should be noted, however, that the eigenvalues change slightly between the onset of stall inception (B) and stall inception (C). Though their general step wise characteristic (Fig. 10) prevails, modes of order higher than 4 become more important, which means that the correlations between eigenfunctions and flow features established from steady operation near stall do not necessarily hold for the entire stalling process.

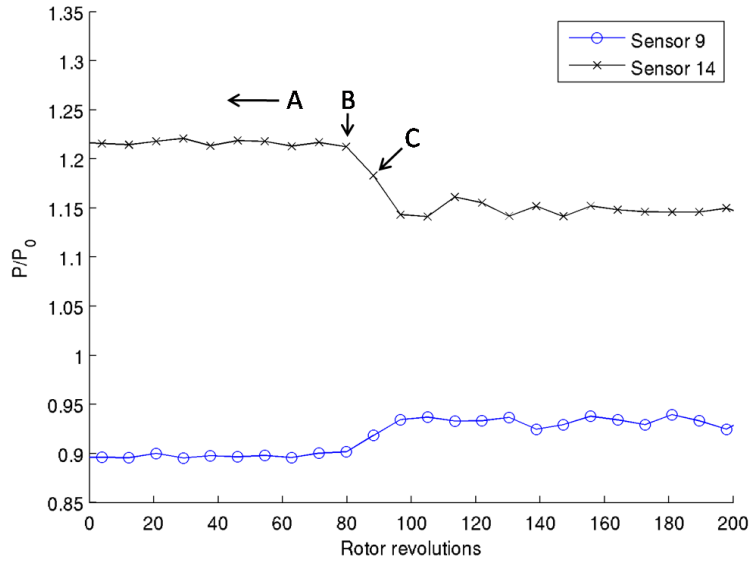

Fig. 14.: Pressure data during transient compressor operation, where each data point represents a running average over roughly 8.5 revolutions. Sensor 9 is the first one over the blade and sensor 14 is the last in the array, half the blade length downstream of the tip. Data for bin A was collected during steady operation, for B at the onset of stall inception and for C during stall inception, respectively.

D. Conclusion

The analysis of high frequency wall pressure measurements of a transonic compressor stage using POD was presented. Rebuilding reduced order pressure fields from these eigenfunctions helped to establish a connection between certain eigenfunctions and flow features. This works best for data taken near the compressor stability limit. Extending this analysis to cases at peak efficiency and in between showed in principal similar results, but the correlation between eigenfunctions and flow features is somewhat more ambiguous. This is due to the lower impact that shock waves and shock/tip clearance vortex interaction have on pressure fluctuations.

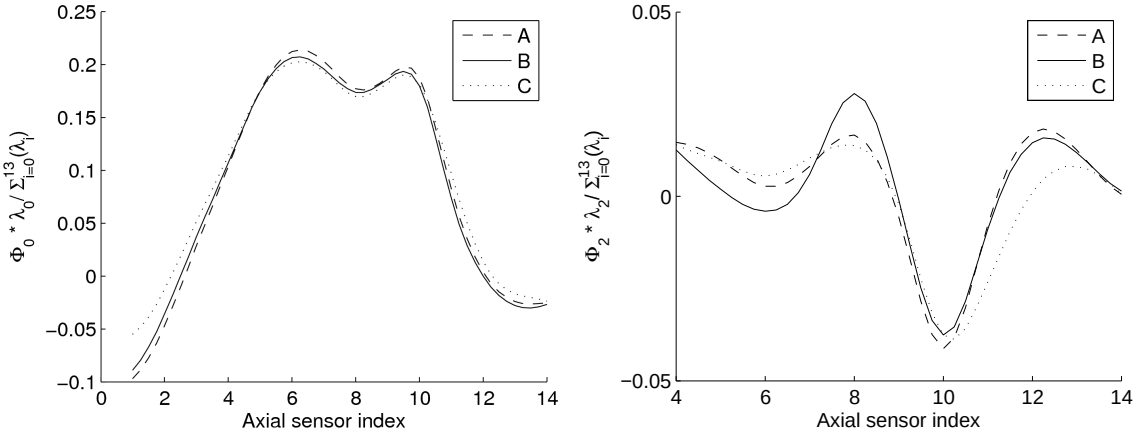

Fig. 15.: The eigenfunctions of mode 0 (left) and mode 2 (right) for three different data bins are normalized with their respective eigenvalue and plotted with a cubic spline interpolation. For the different compressor states, no significant change can be noted in mode 0. For mode 2 and case B, a relatively high peak occurs at senor position 8, which is the one closest to the blade leading edge in the free stream.

When performing spectral analysis of the data, both DPOD and MoS were used to incorporate information in the aperiodic spatial direction. Noise in the measurements tends to appear at higher modes, whereas spectra of lower modes appear cleaner than those of the measured data. In contrast to some sensor signals, the FFT spectra of lower order modes have the highest peaks at the BPF, which is expected. Those modes with a rather uniform power spectrum are accounting for effects not depending on the blade passing such as tip clearance vortex dynamics.

Performing transient POD analysis on a stalling rotor showed consistent eigenfunction behavior for the first 2 modes before and during stall inception. At the onset of stall, an eigenfunction that is related to the tip clearance vortex develops a second peak right at the tip of the blade. Since this is the only change in eigenfunctions from

steady operation, this suggests that the clearance vortex interaction with the blade leading edge might serve as a precursor for stall inception.

CHAPTER IV

IDENTIFYING INEFFICIENCIES IN UNSTEADY PIN FIN HEAT TRANSFER USING ORTHOGONAL DECOMPOSITION

A. Introduction

Optimization in gas turbines, demanded by the market and increasingly strict environmental regulations, mostly concerns overall engine efficiency. It is, amongst others factors, depending on the combustor exit temperature which in modern engines ranges well above the melting point of the blade and vane metal (Schobeiri (2005) [16]). To maintain operability and durability which decreases with higher temperature under oscillating load, cooling the surfaces exposed to the hot gas path is vital. Computational fluid dynamics opens the possibility to study the cooling effectiveness of a pin fin array by examining the details of the flow in both space and time.

At the first stage, turbine blade cooling is typically done both externally (film cooling) and internally. Internal cooling is realized by casting channels into the vane or blade where cooler compressor bleeding air is forced through for convective heat exchange (Fig. 16). However, in the trailing edge region of a vane or blade, the channel height becomes rather small. Manufacturing ribbed cooling channels, which are typically found in the main body of the airfoils, is therefore not possible. Instead, small solid cylinders, or pin fins, are put inside the channel. This leads to an increased heat exchanging surface, higher turbulence levels and increased heat transfer (Han et al. (2000) [17]).

In case of pin fins, this turbulence level increase leads to a higher pressure loss across the array. To avoid backflow of hot combustion cases into the cooling region, the pressure loss has to be compensated by the compressor. Since the pressured

Fig. 16.: Schematic of a turbine blade with a pin fin cooling array in the trailing edge region from Kindlmann (1999) [18].

air can not be used to drive the thermodynamic cycle, extraction of energy from the compressor via bleeding air decreases the overall efficiency of the engine. The engineering task is to find an optimal configuration, with low pressure loss relative to high heat transfer. The turbulent flow dynamics inside pin fin passages are not well understood and difficult to access experimentally.

Towards this goal, computations can have a large impact on improving designs. For design iterations, this requires models as simple and as fast as possible. For this reason, one aspect of this study is to evaluate a URANS model to solve the flow in a pin fin cooling passage. Due to the unsteady nature of the flow and the relatively large amount of data created, effective analytical tools are also required. In this paper, we present results of a numerical investigation of a base line pin fin geometry with a spacing over fin diameter ratio $S/D = 2$ and at an elevated Reynolds number of $\mathrm{Re} = 12,800$, where the Reynolds number is based on bulk velocity and hydraulic channel diameter. The data are analyzed with orthogonal decomposition. As an extension to traditional decomposition methods such as POD, we propose

the inclusion of temperature in terms of thermal energy. To improve the modeling of turbulence of the simulation, a LES study of the same geometry was done and evaluated in the same manner. The basis functions were then ranked with regard to their impact on turbulent surface heat flux.

B. Review of relevant literature

Pin fin arrays for heat transfer augmentation have been studied in a broad variety of experiments (see Armstrong and Winstanley (1988) [19]). Lyall et al. (2007) [20], to which the domain is matched for experimental validation, studied a single row of pin fins with a height-to-diameter ratio $H/D = 1$ in a high aspect ratio channel with varying pin spacings at different Reynolds numbers. They reported results for overall friction factor augmentation, drag on the fin and spatially resolved heat transfer augmentation. A spacing of $S/D = 2$ has been found to show the highest heat transfer augmentation compared to an unobstructed channel from all geometries tested. It is highest for the lowest Reynolds number used, $\mathrm{Re} = 5013$, and remains on a rather constant level for Reynolds numbers between $7500 < \mathrm{Re} < 17500$. The area of highest augmentation in the wake of the fin moves upstream, towards the cylinder trailing edge, with increasing Reynolds number.

Ames and Dvorak (2005) [21] have computationally modeled the flow in a multi-row pin-fin array with the use of the k-ϵ turbulence model in conjuntion with a one-equation model in the boundary layer, which was resolved down to the viscous sublayer. Only one quarter of the full domain was simulated, applying symmetric boundary conditions at the cylinder mid span and along even and odd row pin centerlines. Steady calculations showed an underprediction of heat transfer augmentation and pressure loss. The authors attribute this to the applied cylinder centerline

symmetry, which prevents transient vortex shedding in the trailing edge region of the pin.

To examine the complexity of this flow problem, one can imagine decomposing the flow into a single cylinder in crossflow and an unobstructed channel. The latter is a thoroughly investigated canonical flow problem, serving as a validation source for turbulence model coefficients. More difficulty arise from the cylinder case. Young and Ooi (2004) [22] examined different two-equation turbulence models for a cylinder in cross flow and two dimensions in an infinite domain. The results showed a poor agreement with the experimental data for the drag coefficient. The authors suggest improving turbulence modeling. A known defficiency of eddy-viscosity models is the over prediction of turbulent kinetic energy in stagnating flow, which energizes the boundary layer on the cylinder surface and impacts transition and separation. To improve this, Holloway et al. (2004) [23] propose a third transport equation for laminar kinetic energy, representing the magnitude of non-turbulent stream wise fluctuations in the pre-transitional boundary layer. They report improved predictions for the drag coeffiecient and conclude that boundary layer transition is better captured with their model adaptions. Harrison and Bogard (2008) [24] examined different 2-equation models for a jet in cross flow and heat transfer. They showed that surface heat transfer is reasonably predicted with the SST-k-ω model.

Based on the previous research, we chose to use the SST-k-ω in a three dimensional, span wise periodic domain for the URANS. The near wall mesh resolves the entire boundary layer and the Reynolds number is set at an elevated level of $\mathrm{Re} = 12,800$.

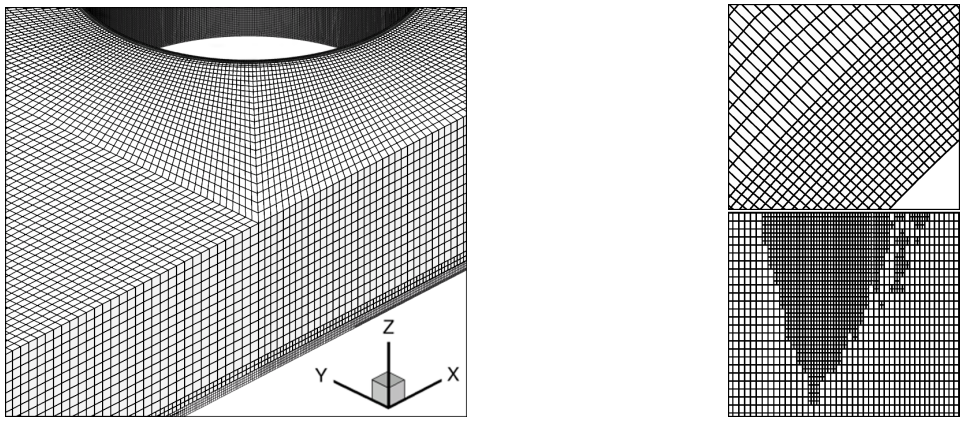

Fig. 17.: The URANS domain mesh close to the pin fin is displayed (left). A top view of the bottom wall mesh is shown in the upper right figure. Grid refinement in regions of high velocity gradients on the pin fin surface viewed from the front are visible in the lower right figure.

C. Computational procedure

In this section, the settings, mesh setup and boundary conditions for the URANS part are outlined. A grid independence study was performed to obtain an estimate on the uncertainty of the computational results. The LES domain and boundary conditions are described in the second subsection. The third subsection closes with a description of the modified signal decomposition procedure for data analysis.

1. Solver settings and grid for URANS study

The commercial Navier-Stokes solver Fluent 6.2.16 was used in conjunction with the SST-k-ω model. This model blends a k-ω closure near the wall with a modified k-ϵ formulation in the free stream. Furthermore, the transitional option was enabled, which activates a Low-Reynolds number modification of the model and damps the

eddy viscosity in the near wall region (Durbin (1996) [25]). The discretization schemes for time, pressure and all transport scalars are of second order, where an upwinding scheme has been used for the convective terms, energy and turbulence scalars. Time is advanced with an implicit algorithm. Pressure and momentum are coupled with the PISO algorithm (pressure-implicit with splitting of operators) since the mesh had some skewed cells at the interface between the channel grid and the cylinder grid (Fig. 17). The PISO scheme also yields faster convergence and allows pressure and momentum under-relaxation parameters to be set to unity. The Courant number is close to unity for the employed time step of $\Delta t = 0.001s$. This is roughly equal to 0.034% of one cylinder lift cycle. One time step was considered converged when all residuals fell on the order of 10^{-5}. The entire simulation was run for a little over 100 cycles of cylinder lift coefficient. On a 40 processor cluster, computing 5 lift cycles for this study with 15,000 time steps and 6 iterations per time step took about 7 days wall clock time.

The computational domain models a single row of pin fins inside a rectangular duct, where the ratio of duct height to cylinder diameter is unity, $H/D = 1$ (Fig. 18). The influence of walls in the spanwise direction is neglected by assuming an infinite row of fins and applying periodic boundary conditions on the lateral domain faces, which are positioned such that one full pin fin is included within the domain. Experimentally, this can be achieved by examining a long row of fins with the spanwise test section dimension much larger than the duct height and assuming that the middle pins will not see the influence of the spanwise walls.

The spanwise periodic boundaries are $2D$ apart, yielding an infinite row of pin fins with a spacing of $S/D = 2$. Only one half of the domain in the wall normal direction is meshed and computed to save computational ressources. A symmetry boundary condition is applied on the top face. A pressure outlet boundary condition is used

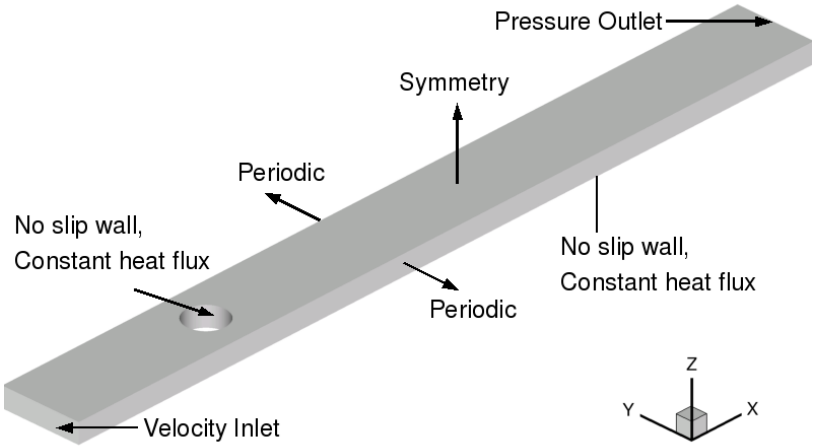

Fig. 18.: The computational domain of the URANS study with applied boundary conditions is shown schematically.

$14D$ downstream of the pin fin center. All required boundary values at the inflow, which is modeled as a velocity inlet $4D$ upstream of the pin, were obtained from a steady state simulation of an unobstructed channel beforehand and then linearily interpolated to fit the pin fin domain mesh. A specific wall heat flux $\dot{q}_W$ was imposed on the no-slip bottom wall. Since the fin is only heated by conduction, its surface heat flux was calculated from the cylinder cap area covered by the heated channel walls and also imposed as a constant heat flux boundary condition ($\dot{q}_{PinFin} = \dot{q}_W/2$).

Initially, a structured grid was created with Gambit. Since wall functions cannot correctly model the complex flow phenomena, the boundary layer is resolved down to the viscous sublayer with a solution based grid adaptation. Fig. 17 shows some adapted mesh regions on the pin fin surface and the endwall. The final mesh contains around 6.2 million hexaedral cells. Before data for the OD analysis were recorded, cells with high gradients in velocity (near the cylinder wall), high skewness and distance

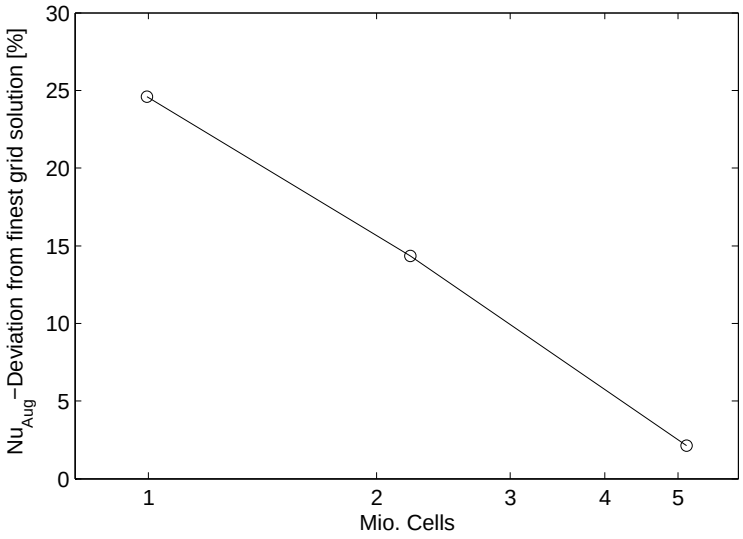

Fig. 19.: The deviation of Nusselt number augmentation for three coarser grids compared to the finest grid solution is plotted for the URANS simulation.

too far from the wall, were refined at multiple instants in time to retain symmetry within the mesh. Around 98% of the wall nearest cells range between $0 < y^+ < 2$ and no cell is farther from the wall then $y^+ = 5.4$. For the grid independence study as shown in Fig. 19, first all cell adaptations were removed yielding a domain with 1 million cells. For the second domain with 2.2 million cells, only the first adaptation level was retained. The third domain consists of 5.1 million cells and was created by removing refinements in the upper boundary layer parts. The Nusselt number averaged over the entire bottom surface (Fig. 18) was then calculated and related to an open channel correlation found in Kays and Crawford (1980) [26]. The local reference temperature is calculated from an energy balance, in detail shown in Lyall et al. (2007) [20]. This Nusselt number augmentation for the three coarser domains is then related to the finest grid solution in terms of percentage deviation and plotted in Fig. 19.

2. LES study

For the large eddy simulation, the domain was extended to include three cylindrical pins as opposed to one in order to avoid locking the shedding frequency in the wake of the pin by imposing periodic boundary conditions enclosing only one single pin. The spanwise periodic boundaries are therefore $6D$ apart, the outflow with a pressure outlet was placed $9.5D$ downstream of the pin row middle and the inflow is $9D$ upstream. The domain was extended to contain the full pin height and is thus bounded by two walls in z (Fig. 18). To generate a fully developed, turbulent inflow, the inflow plane is a recycling periodic boundary that picks up velocity and temperature values from a recycling plane located $3D$ upstream of the pin middle. When copying the different variables from the recycling plane to the inflow plane, the velocity components are scaled to maintain a constant flow rate. The heat added due to the constant wall heat flux at the walls within this quasi periodic section is computed from a First Law energy balance and substracted from the recycling temperature. The Navier-Stokes equations are solved using a spectral element method (for details see Fischer et al. (2008) [3]). The mesh consists of 3552 elements and within each, the solution is approximated by 13th order Legendre polynomials. To account for the unresolved grid scales, the last 3 modes of the solution polynomials are multiplied with a second order filter function such that the last mode is reduced by 5%. This grid resolution provides a maximum wall distance of the wall nearest cell (in the region of highest wall shear) of $z^+ < 1$. Away from the walls, the grid point spacing increases in the wall normal direction z (but stays the same in the streamwise x and spanwise y direction), such that the grid point spacing is $\Delta x^+ \approx 33, \Delta y^+ \approx 22, \Delta z^+ \approx 11$ in the middle of the recycling inflow subsection. For the spectral element LES, a convergence study could be done by increasing the polynomial order, which would couple the filter width with

grid spacing, similar to eddy diffusivity LES on finite volume meshes. As pointed out by Celik et al. (2009) [27], this prohibits estimating convergence towards a grid independent solution. For this reason, no convergence study is presented herein and validation against experimental values becomes even more important.

D. Results

To ensure a fully developed and statistically stationary flow, the lift coefficient on the cylinder surface,

$$C_{L(t)} = \frac{F_{L(t)}}{\frac{1}{2}\rho U_0^2 A_{Normal}}, \tag{4.1}$$

was monitored over the simulation time and is shown in Fig. 20, top, for the URANS simulation. One data sample was taken every 30 time steps so that roughly 90 snapshots are collected per one lift coefficient period. In comparison, Fig. 20, bottom, shows lift and drag coefficient (the respective forces are normalized as in Eqn. (4.1)) for the LES on the middle pin. Here, roughly 34 data samples are collected for one lift cycle. The periodic boundary enclosing only one pin does indeed lock the shedding frequency, whereas the 3-pin arrangment allows for the lift on the middle pin to vary more freely. The frequency of vortex shedding, which causes the oscillations of the lift coefficient, is nearly constant and ranges between 0.333Hz and 0.342Hz in the URANS study. On average for the plotted time range, the Strouhal number Str = 0.326, which is considerably higher than experimentally obtained results for a single cylinder in crossflow. The amplitude of the lift coefficient is also higher than what is expected. The Strouhal number obtained from the LES and the middle pin is slightly higher. The friction factor augmentation upstream of the pins from the LES study is shown in Fig. 21. Two different experimental correlations for the baseline

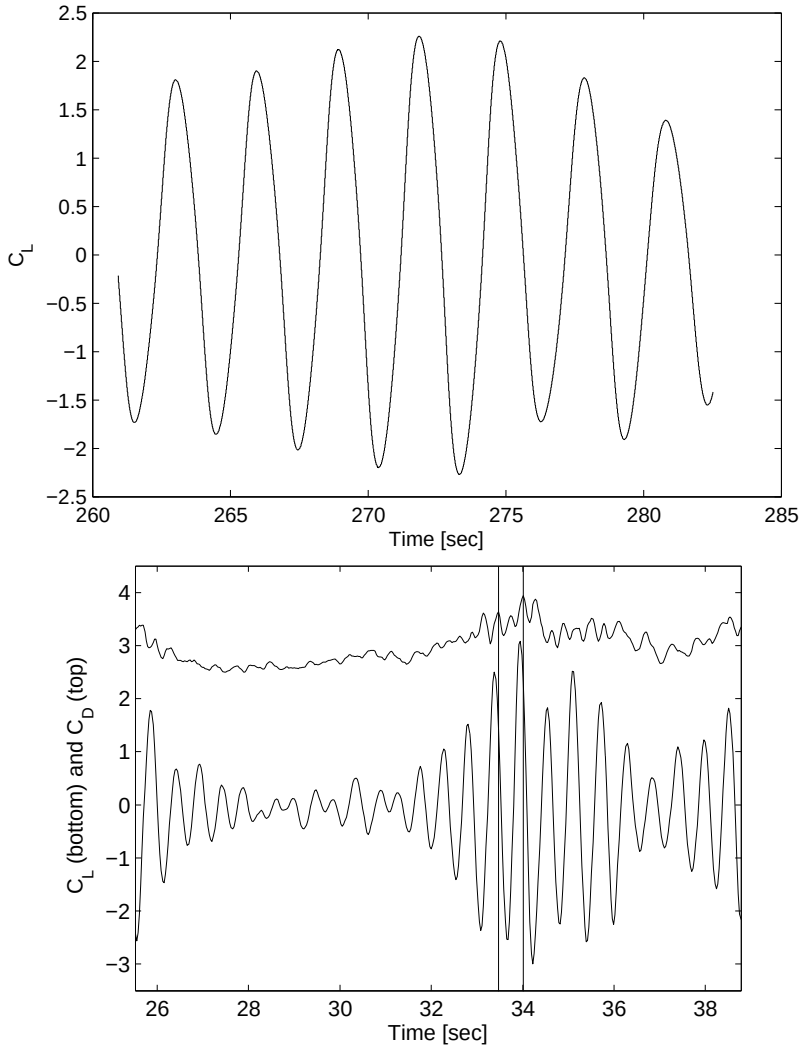

Fig. 20.: The plot shows normalized lift force on the pin for the URANS study (top) and lift and drag for the LES on the middle pin (bottom). The vertical lines indicate the time span of the smaller sample used for orthogonal decomposition. The lift and drag coefficients vary in magnitude and slightly in frequency. Even though the shedding breaks down for some time in the LES, it recovers to its former extent.

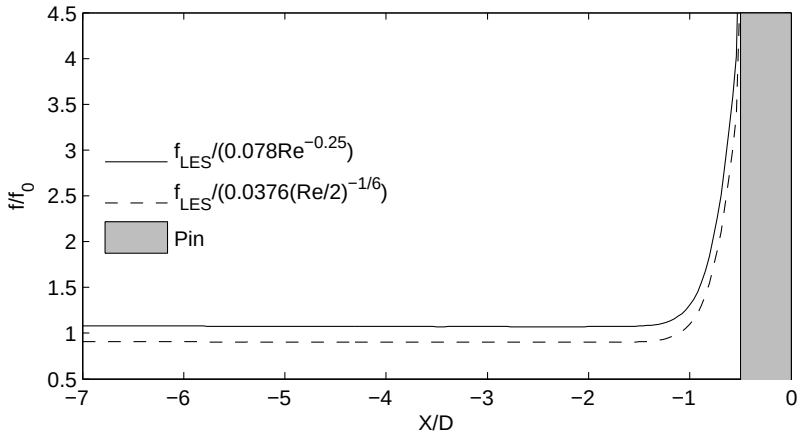

Fig. 21.: The local, span-wise averaged friction factor augmentation from the LES study is plotted as a function of streamwise distance. The pressure data is normalized with different baseline correlations.

friction factor f_0 were used: the one that gives higher augmentation values is used in Lyall et al. (2007) [20] and was developed for geometries of circular cross section, but is expected to be valid for rectangular channels when basing the Reynolds number on the hydraulic diameter. As pointed out by Patel and Head (1969) [28], this concept breaks down for high aspect ratio channels, and another expression is shown therein (valid to $3000 < \mathrm{Re_C} < 10^5$, where $\mathrm{Re_C}$ is based on the channel height) which leads to the lower augmentation in Fig. 21. The computational results lie roughly in the middle between the two correlations within a 6%-7% range. From the plot, it is noted that the flow within the recycling section is statistically fully developed as the friction factor is a straight horizontal line. Lyall et al. (2007) [20] also present an array friction augmentation $(f - f_0)/f_0 = 3.8$ for the given geometry and Reynolds number. The pressure loss was measured over 15 hydraulic diameters. Since the computational LES domain was not that long, pressure loss from plane averaged data and wall pressure

values were evaluated at locations 7 hydraulic diameters apart. The downstream pressure measurement location was 5.75D away from the pin center. At this point, the pressure has not yet fully recovered and the friction factor is not quite constant. But due to the accelerated outflow which started at 5.75D, this location is as far away from the pins as possible. This resulted in $(f - f_0)/f_0 = 3.75$ when using the static wall pressure line-averaged in the spanwise direction, and a slightly higher value of 4 when using y/z-planar averaged pressures. A comparison of Nusselt number augmentation on the channel wall is shown in Fig. 22. The experiments, described in Lyall et al. (2007) [20], were conducted using the same geometry and Reynolds number as in the present study. The surface Nusselt number augmentation is defined as the ratio of actual Nusselt number (with a reference temperature depending on the stream wise position) over the Nusselt number for an unobstructed channel (found in Kays and Crawford (1980) [26], $\mathrm{Nu}_0 = 0.022\mathrm{Re}^{0.8}\mathrm{Pr}^{0.5}$). For Fig. 22, bottom, two additional correlations for Nu_0 are used: the Dittus-Boelter correlation from Incropera and DeWitt (2002) [29] and a baseline Nusselt number computed based on the friction factor from Patel and Head (1969) [28]. Results are plotted in terms of a spanwise line average. Since the computational domain did not include the solid pin fin body, no data are presented in the region where the pin is mounted onto the channel surface (gray area in Fig. 22). Close to the pin fin, both computations show significant peaks that deviate from the experiments. This can be explained by the heat transfer augmentation on the channel surface due to conduction through the fin. This effect, as well as conduction within the wall itself, is not included in the simulations. A similar trend is shown by Su et al. (2005) [30], who used a RANS approach for an array of pin fins (at slightly different Reynolds number and $H/D = 2$). Compared to experimental values, the computed endwall heat transfer shows similar peaks near the pin fin row independent of row number. Upstream of the pin fin, heat transfer

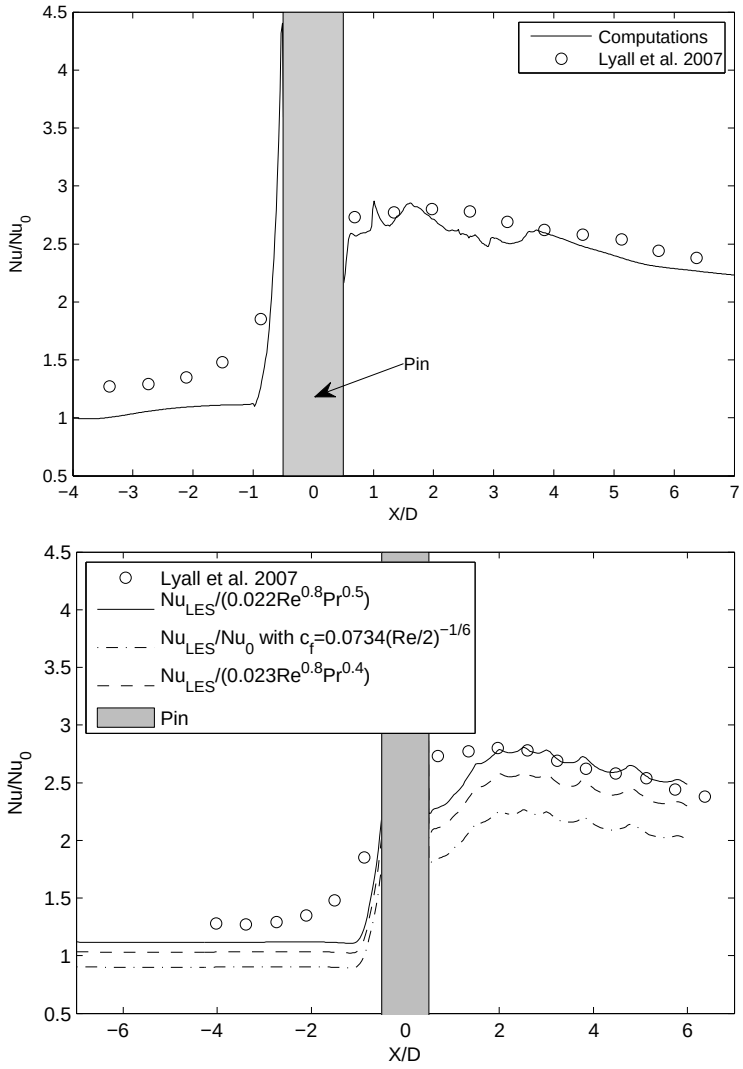

Fig. 22.: The local, span-wise averaged Nusselt number augmentation from the URANS (top) and LES (bottom) study compared to experiments is plotted as a function of streamwise distance. The temperature data is normalized with different baseline correlations.

Table I.: Time sample sizes and dimensions from URANS, excluding the first mode. D_{90}, D_{95} and D_{99} is the number of modes required to retrieve 90, 95 and 99 percent of the flow, respectively.

Sample size	D_{90}	D_{95}	D_{99}
89	3	6	19
268	4	7	35
446	4	9	51

augmentation is predicted around unity for the URANS study, which is expected but below experimental values. This might be due to different turbulence inlet conditions compared to the experiment or an inappropriate correlation for Nu_0. Lyall et al. (2007) [20] used a sand paper strip upstream of the fin row to trip the boundary layer, whereas the URANS simulation inlet conditions were computed from a smooth turbulent channel flow. The URANS computation shows a reasonable agreement in the pin fin wake, but those results are improved with the LES. Using the same correlation as Lyall et al. (2007) [20] for baseline heat transfer, the augmentation in the wake is matched closely. The peak locations of this curve are identical to the element corners of the spectral element grid. Upstream of the pin, the LES data show good agreement with the Dittus-Boelter correlation from Incropera and DeWitt (2002) [29].

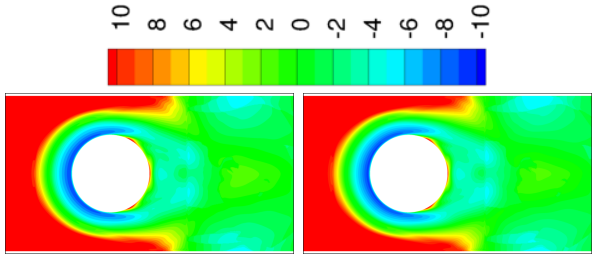

Fig. 23.: The contour plots of the average bottom wall temperature (left) and the scalar spatial eigenfunction $\varphi^k(\vec{x})$ of mode 0 at the bottom surface (right) from the URANS computation are identical. The data are scaled to a common color range.

1. Orthogonal decomposition URANS

The decomposition analysis was performed on three URANS data sets of different sizes in time, namely for one, three and five lift cycles. The time sample sizes can be found in Table I. To ensure convergence of the decomposition method, three different dimensions of the system are also given in Table I. When plotted over the number of time samples used, the dimension should converge towards a constant value. That is not the case for the three samples under consideration. But since the system is periodic in time and turbulent fluctuations are filtered out by the chosen turbulence model, the first 6 modes under examination are expected not to change when extracting the modes from data taken over a longer flow time. The time averaged values for temperatue and velocity were not substracted from the data before hand, thus the eigenfunctions of the first mode 0 are a representation of the average. Its spatial representation is depicted in Fig. 23 and is very similar to the average wall temperature contour in the same figure. The cooling effect of the leading edge region horseshoe vortex, winding around the cylinder at its junction with the endwall, can be seen as an area of relatively low temperature where cool core flow is

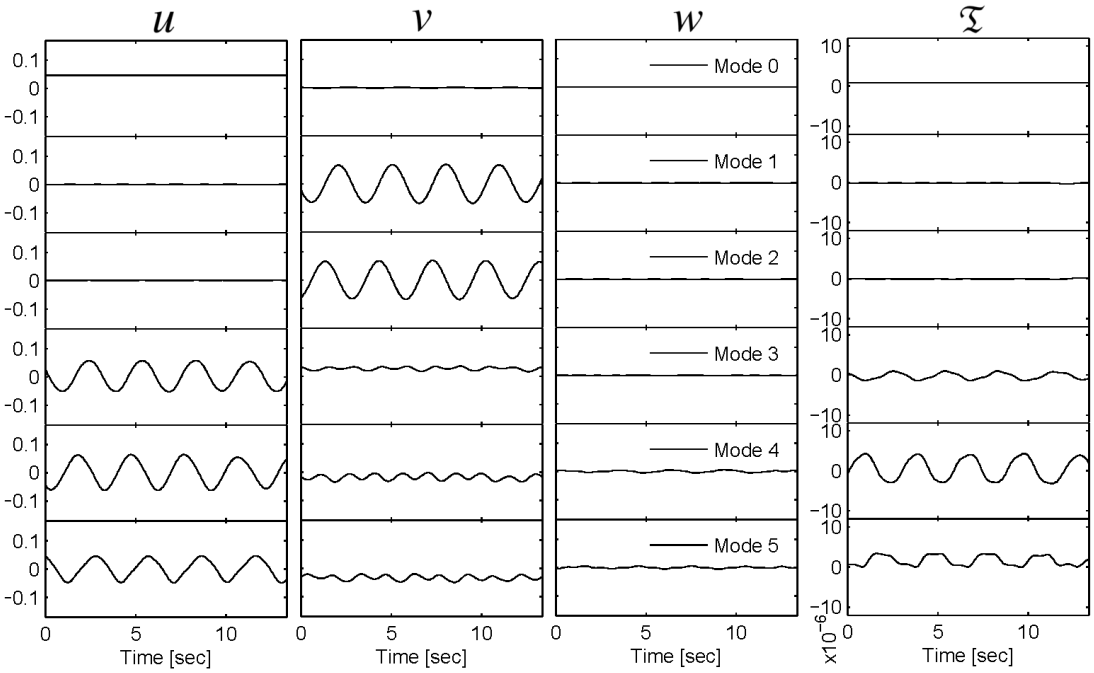

Fig. 24.: Time eigenfunctions $\Psi_i^k(t)$ from the URANS computation of the first 6 modes for velocity (3 left) and temperature (right). The constant average streamwise velocity component (top left), two lift modes oscillating in the spanwise velocity v and three shearing modes 3-5 can be identified.

pushed towards the heated endwall. Downstream of the pin fin, vortices spinning off from the cylinder create a rather homogeneous, relatively low temperature profile.

The time eigenfunctions $\Psi_i^k(t)$, Fig. 24, show that the only non-zero average component is the streamwise velocity and the temperature in mode 0. Both modes 1 and 2 contain the flowfield responsible for spanwise flow fluctuations, causing a lift force on the pin fin. The wall temperature fluctuations start deviating from the mean for modes higher than 2, as seen by the respective time eigenfunctions which increase by an order of magnitude. The time eigenfunctions of temperature have an overall much lower value due to the weighting when assembling the correlation

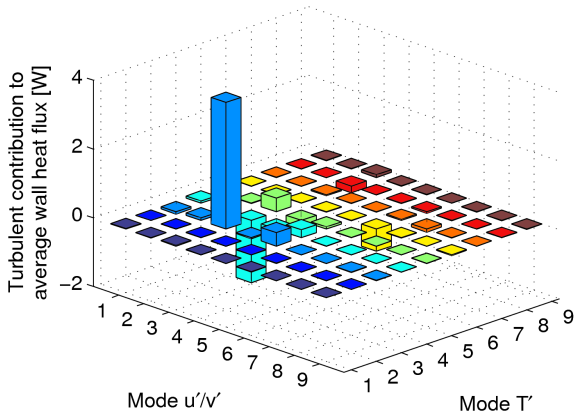

Fig. 25.: Different modes $k \neq 0$ have been used to evaluate the integrals in Eqn. (2.38) for the URANS and show that the dominant mode combination in terms of surface heat flux is 3/3.

matrix. This does not mean that they are less significant. The time basis functions from the medium and small sample size have similar qualitative features as the time functions shown in Fig. 24. The decomposition analysis (Fig. 24) shows that the first three modes look essentially the same with respect to wall temperature, therefore the flow field represented by modes 1 and 2 does not contribute to a change in wall temperature and thus heat transfer. The energy contained in these two modes (83.22% of the energy in all non-zero modes) can therefore be considered a loss and a closer examination might yield some potential for either optimizing the geometry or fin arrangement. The evaluation of the integral from Eqn. (2.38) is shown in Fig. 25, where different mode combinations have been inserted for the fluctuating parts and the average ($k = 0$) was not considered. Mode combination 3/3 has the highest contribution to turbulent heat flux for a control volume around the pin. Due to the optimality of the orthogonal expansion, the higher order modes show a decreasing importance.

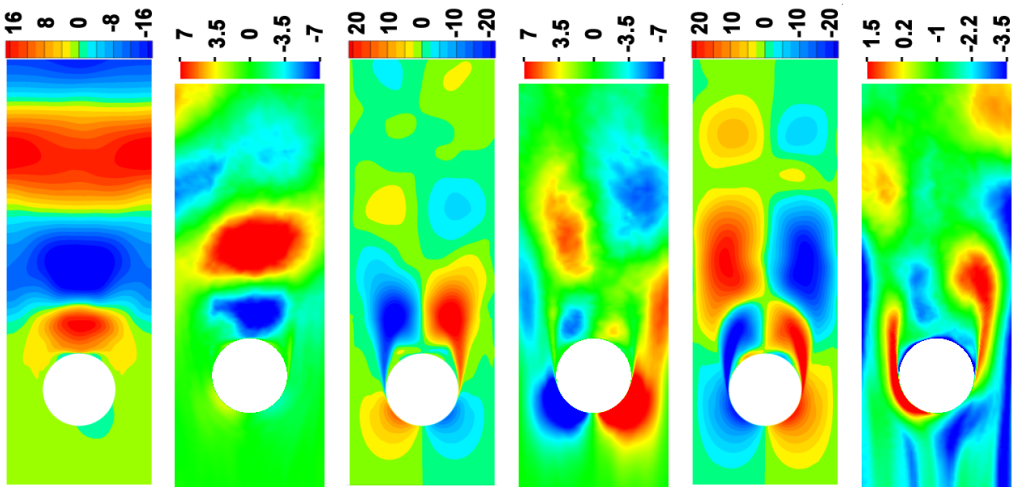

Fig. 26.: The figure shows contours of the scalar spatial eigenfunction $\varphi^k(\vec{x})$ at 10%D. The plots from left to right are: Mode 2 URANS, mode 2 LES, mode 3 URANS, mode 3 LES, mode 4 URANS, mode 7 LES.

In Fig. 26, the near wall spatial eigenfunctions (which include all four components of the flow field) are plotted on a plane at $10\%D$ above the bottom wall. The spatial eigenfunctions of the parasitic mode 2 is shown left in Fig. 26. Compared to the useful spatial eigenfunctions of modes 4 and 7 (Fig. 26, right), which contribute to heat transfer increase, they appear as a one-dimensional wave function of streamwise distance downstream of the pin. Mode 3, in turn, has a higher spatial complexity and covers the region of the stagnating horseshoe vortex.

2. Orthogonal decomposition LES

For the LES, an orthogonal expansion was computed within a box around all 3 pins, where the box covered the domain between 3D upstream of the pins and 5.75D downstream, for two data sets - one spanning the entire lift history as seen in Fig. 20 and another one for approximately one lift cycle as indicated by the vertical lines in the

same figure. Every second data sample (for a total of 443 samples) was used to compute the orthogonal expansion. The plot of time basis functions for the larger sample size is shown in Fig. 27, which is qualitatively similar to the basis functions obtained from the smaller sample. Again, since the time averages where not substracted before hand, mode 0 shows the mean flow rate in x and an increase in mean temperature. As seen from the basis functions from URANS, the high order v-modes are very similar to the lift oscillation, but as there are now also fluctations in the streamwise direction, the u-functions exhibit the same dynamics as the drag curve in Fig. 20, bottom. The first non-zero mode in the temperature functions is mode 7, where it was mode 3 in URANS. This is due to the fact that LES data contain more large energy fluctuations (large eddys are now resolved) which spread the mode spectrum over a higher energy range compared to RANS. But it can still be hypothesized that there are mode combinations which do not contribute to heat transfer augmentation. Modes one to six contain 32.14% of the total energy in all non-zero modes. Unlike in the URANS, the temperature function of mode 7 does not strongly correlate with velocity and does not vary in time. Similarities between URANS and LES also exist for the spatial functions, which are shown in Fig. 28. The mode representing the average flow field (whose only non-zero time basis function is in the streamwise component), top left, extents farther downstream from the middle pin compared to the side pins. This is due to the break up of vortex shedding, which makes the wake of the middle pin longer for a certain part of the simulated time. A lift mode, lower left, whose time basis function has the highest amplitude in the v-component, is very similar to what was seen from the URANS results. The shearing mode 3, which in the URANS study used to be the most important mode for turbulent heat flux, also has a very similar spatial basis function structure as it is active in the region of the horseshoe vortex. The quantitivative mode assessment is shown in Fig. 29, proving that the

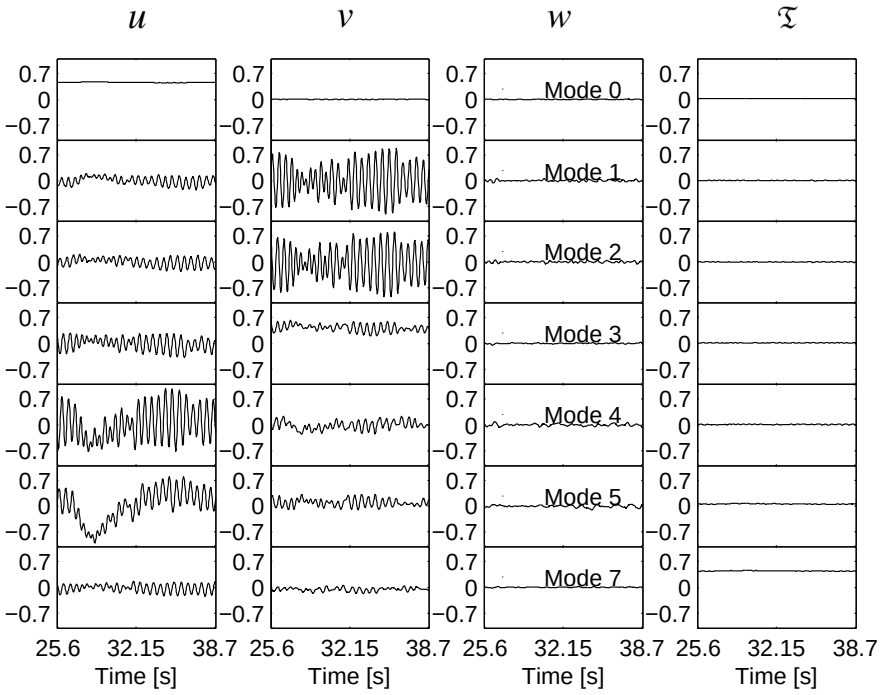

Fig. 27.: Time eigenfunctions $\Psi_i^k(t)$ of 8 modes for velocity (3 left) and temperature (right) from the LES. The constant average streamwise velocity component (top left), two lift modes oscillating in the spanwise velocity v and two mainly shearing modes 4-5 can be identified. The first mode with non-zero temperature function is mode 7. The functions are scaled for better visualization.

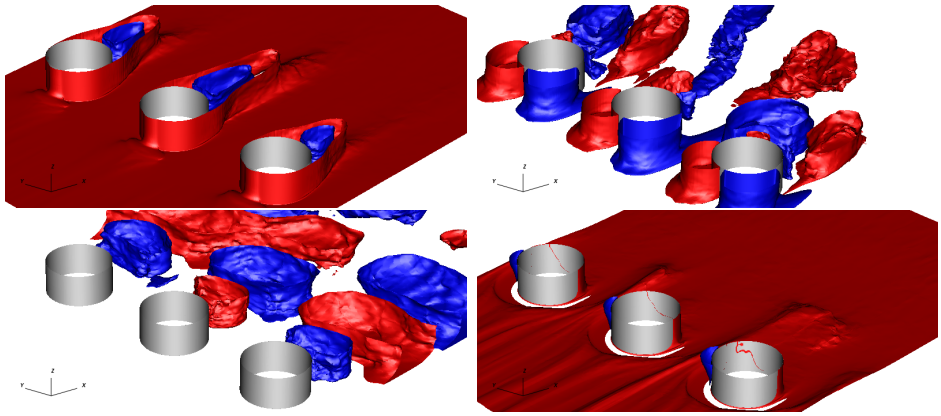

Fig. 28.: The figure shows isosurfaces at -4 (red) and 4 (blue) of the scalar spatial eigenfunction $\varphi^k(\vec{x})$ of the LES. Upper left: Mode 0, lower left: Mode 2, not contributing to heat transfer. Upper right: Mode 3, a shearing mode. Lower right: Mode 7, useful mode in terms of heat transfer.

mode combination 7/7 has the highest positive heat transfer contribution. In this application, higher heat transfer is desired since the internal passage is intended to cool the blade walls. Combinations of temperature mode 7 with other velocity modes, shown in Fig. 29 right, have a negative impact on wall heat flux.

E. Conclusion

Using an unsteady RANS calculation and a LES, the heat transfer effectiveness of a single, infinite row of pin fins was examined. This geometry can be found in a simplified internal cooling passage at the trailing edge region of a gas turbine blade. The infinite row was simulated with one pin (URANS) and 3 pins (LES) enclosed by periodic boundaries. Compared to experiments, the computationally intense simulations showed good agreement, depending on the correlations for unobstructed flow from the literature. The level of resolution in space and time allows for a high order

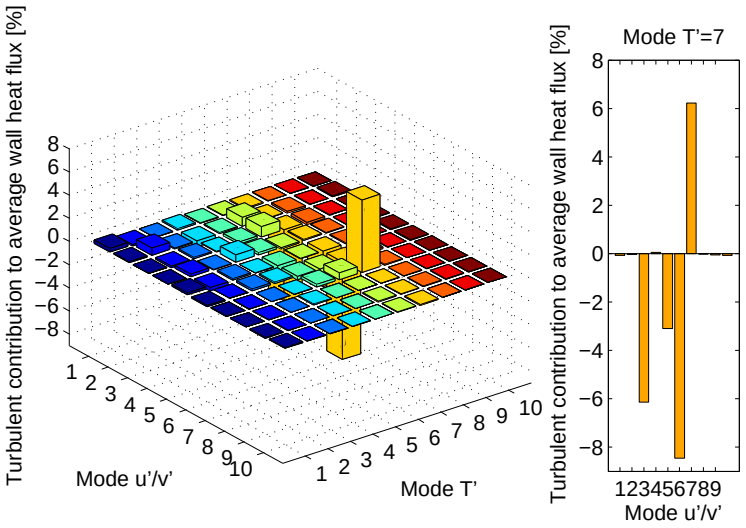

Fig. 29.: Different modes $k \neq 0$ have been used to evaluate the integrals in Eqn. (2.38) for the LES and show that the dominant mode combination in terms of positive surface heat flux is 7/7.

analysis of the pin fin heat transfer effectiveness that would be impossible to obtain experimentally.

With the presented orthogonal decomposition and analysis technique, flow features that do not contribute to heat transfer augmentation but contain relatively high amounts of energy are identified in modes that mainly contain the part of the flow responsible for lift. This means that there is plenty of room for optimization towards more efficient internal cooling. Potential improvements would include geometric adjustments that cause higher streamwise flow fluctuations relative to the spanwise fluctuations.

CHAPTER V

OPTIMIZING TURBULENT HEAT TRANSFER USING ORTHOGONAL DECOMPOSITION BASED CONTOURING

A. Introduction

Heat transfer in turbulent flows is not only an academically challenging problem, but also of great relevance to many real world applications. In a great number of thermal-fluid engineering systems, efficiency is directly related to the amount of heat a surface can withstand without melting. Unfortunately, turbulence enhancing methodologies to increase the rate of heat transfer often come at the cost of increasing pressure loss. In order to characterize and understand such flows, well resolved investigations are needed because steady simulations (Reynolds-averaged Navier-Stokes) do not compare well with experimental data and experimental point or planar measurements cannot capture 3D turbulent structures. Recent advances in supercomputing with large eddy simulation (LES) and structure identification techniques (proper orthogonal decomposition) now make an investigation into the flow dynamics and heat transfer accessible computationally.

The advantages are significant as computational visualization and advanced analysis such as proper orthogonal decomposition offer insight into the heat transfer dynamics. The challenge, as in any computational work, is to validate resolution and model accuracy by comparing to experimental results. Once validated, the insight gained is applied to a more physics-based methodolgy of optimizing turbulent heat transfer systems.

Many computational optimization strategies are based on user defined design parameters and cost functions, for which global minima are searched. The number

of simulations to map out the solution space increases with the number parameters, which prohibits the use of LES in many cases. Further, the solutions are constrained a priori by the design parameters - it is not known whether the iterated optimum is the best solution possible.

In this study, an analysis methodology that is based on orthogonal basis functions derived from post processing data from a highly resolved simulation is developed and tested. The orthogonal basis functions are ranked with respect to their contribution to surface heat flux. An isosurface of the most important mode is then used to optimize a heat exhanger via end wall contouring. As opposed to gradient based optimizing strategies, this approach is led by the flow physics and does not require user constraints.

B. Background

To develop and test the novel analysis methodology, a turbulent heat transfer application that is both computationally tractable as well as practically relevant is needed. It was found in pin fin heat exchangers, which have been studied in broad variety (see Armstrong and Winstanley (1988) [19]). A fairly low Reynolds number study with a relatively simple geometry that still contains all relevant features of such flows is presented in Lyall et al. (2007) [20], which serves as an experimental validation for this work. A single row of pin fins with a height-to-diameter ratio $H/D = 1$ in a square duct with a very high aspect ratio was studied under varying Reynolds number and pin spacing. Results were reported in terms of friction and heat transfer augmentation compared to unobstructed channel flow. The pressure measurements were performed on certain wall locations, where the temperature was measured with high spatial resolution. The heat transfer increase for a pin spacing of $S/D = 2$ is

highest for the lowest Reynolds number used, Re = 5013, and remains on a rather constant level for Reynolds numbers between $7500 < \mathrm{Re} < 17500$.

Computationally, this problem was examined by Ames and Dvorak (2005) [21] in a multi-row pin-fin array. They used the k-ϵ turbulence model and symmetric boundary conditions at the cylinder mid span and along even and odd row pin centerlines. Their steady calculations showed an underprediction of heat transfer augmentation and pressure loss. One reason for the deviation might lie within the turbulence closure: for the cylinder in crossflow, Young and Ooi (2004) [22] examined different two-equation turbulence models and found poor agreement with the experimental data for the drag coefficient. They suggest improving turbulence modeling. The over prediction of turbulent kinetic energy, a known defficiency of eddy-viscosity models in stagnating flow, does not allow for correctly determining the boundary layer separation point, which has an impact on the wake and thus wall surface heat transfer. Holloway et al. (2004) [23] introduce a third transport equation for laminar kinetic energy, which is expected to extend the turbulence model's validity to pre-transitional, laminar boundary layers.

The underlying problem, that deriving turbulent viscosity from strain rate is not a valid concept in intermittent regions or laminarization zones, is adressed by Stolz (2005) [31], who developed a closure for large eddy simulations based on high pass filtered velocities. The model, which in principal is similar to an eddy viscosity ansatz for the sub grid stresses, is supposed to be inactive when no fluctuations (only low frequencies) are present in the flow. High shear in a laminar layer would thus not lead to excessive sub grid stress. A natural way to implement such a model is the use of a spectral code, where the solved variables are represented as polynomials of different order. A highly parallel, open source and accurate spectral element code, NEK5000, has been developed by Fischer et al.(2008) [3]. The solver has shown 70%

parallel efficiency for over 230,000 processors. As an alternative to increasing viscosity in the momentum equation to account for unresolved scales, the stabilizing filter as proposed in Fischer and Mullen (2001) [32] is used as a fixed coefficient turbulence model for the large eddy simulation.

The wealth of data obtained from spatial and temporal highly resolved simulations offers the chance to gain insight from postprocessing beyond first and second order statistics. Ball et al. (1991) [13] apply proper orthgonal decomposition to data from direct numerical simulation of channel flow in order to understand bursting and sweeping events in the turbulent boundary layer. Later, Duggleby et al. (2009) [14] applied the same methodology to discover the energy transfer between turbulent structures in pipe flow. These studies show that orthognal decomposition is an effective way to analyze turbulent flow data. Due to the canonical nature of their geometries, the direct computation of orthogonal spatial basis functions (proper orthogonal decomposition) could be done efficiently due to a priori known results in the periodic directions. For the pin fin domain, this is not the case. Thus, an alternative method is needed which is shown in Aubry et al. (1991) [4]. Their work demonstrates the equivalence of orthogonal basis functions derived from time and space autocorrelations. Orthogonal modes can also be used to build reduced order models. One application is flow control, for example to reduce drag by affecting the vortex shedding in the wake of cylinders, by Bergmann and Cordier (2008) [33].

Some current computational fluid dynamics optimization strategies are presented in Thvenin and Janiga (2008) [34]. One way to optimize turbulent heat transfer systems is by deforming the wall surface. In one article, the wall of a wavy channel was optimized for low pressure loss at high heat transfer. When using polynomial functions to parametrize the two dimensional wall contour, some efficient design solutions could not be fabricated and had to be filtered out. For more complex geometries,

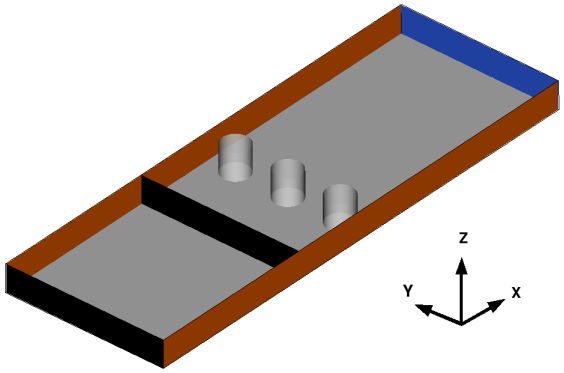

Fig. 30.: The computational domain consists of periodic boundaries in the lateral direction (brown), a pressure outlet (blue), no slip walls with a constant heat flux (gray) and a recycling inflow (two black planes), where velocity and temperature is copied from the downstream plane to the domain inlet after appropriate scaling. The top wall is omitted for better visualization.

Lynch et al. (2011) [35] and Saha and Acharya (2008) [36], for example, use nonaxisymmetric endwall contouring to improve heat transfer in a turbine passage. The geometry can be determined computationally by parameterizing the surface, defining a cost function and then trying to find optima by probing the solution space. A high likelyhood of finding global optima instead of local ones is provided by genetic algorithms as shown in Reising and Schiffer (2009) [37], who used a commercial CFD code to optimize a compressor stage by hub and shroud contouring. Solutions are explored that are defined and constrained by the user defined design parameters and rely on a mulitude of CFD runs, which were coarsley resolved (RANS turbulence model) to maintain computational feasibility.

C. Computational setup

The computational domain consists of three pins in a square channel, with height to pin diameter ration $H/D = 1$ and spacing $S/D = 2$. Measured from the pin centers, the domain extends 8.5 pin diameters downstream and 9 pin diameters upstream. In the lateral direction (y in Fig. 30), periodic boundaries simulate an infinite, single row arrangement. Three pins instead of one were included to avoid locking the vortex shedding frequency. Top and bottom are modeled with no slip walls and a constant specific heat flux boundary condition. The heat flux applied on the no slip pin cylinder walls is equal to the heat conducted through the cylinder caps covered by the endwall. Starting 1.75D upstream of the outflow plane, a source term is added to the continuity equation. Its strength increases linearily. This results in an acceleration towards the outflow plane and straightens vortical flow structures that might create a backflow through the pressure outlet, which in turn might cause a diverging simulation.

To generate a turbulent inflow, a recycling section is implemented (enclosed by the two black planes in Fig. 30) where all three velocity components and the flow temperature are read during runtime from the downstream plane and then copied to the inflow. Within it, the flow is initialized with a Walsh vortex solution in the x/y-plane (see Walsh (1992) [38]). When recycling, all velocity components are scaled such that a domain averaged mean stream wise velocity of unity is maintained. The total added heat is substracted from the recycling temperature. For the given diameter, the viscosity is set to yield the flow Reynolds number based on hydraulic channel diameter and bulk velocity of $\mathrm{Re} = 12,800$. The fluid conductivity is fixed such that the Prandtl number is $\mathrm{Pr} = 0.71$. The incompressible Navier-Stokes equations together with the energy equation, temperature being treated as a passive scalar, are solved using a spectral element method (Fischer et al. (2008) [3]). The domain is meshed with 3552

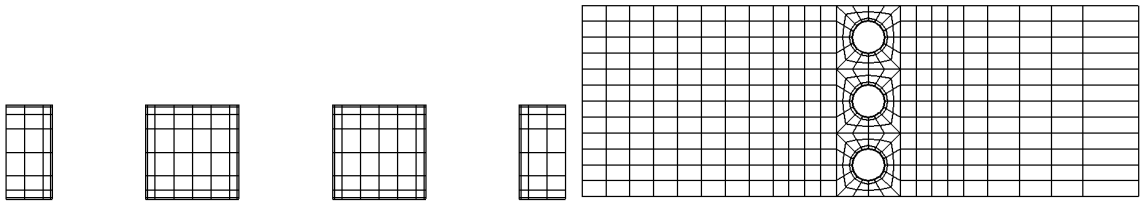

Fig. 31.: The mesh consists of hexahedral elements, which are smaller near the wall. The left figure shows a slice in the y-z plane through the pin row center. The right plot shows a slice in the x-y plane, where the pin fin bodies appear as unmeshed holes.

hexahedral elements (see Fig. 31) and within each, the solution is approximated with 13th order Lagrange polynomials. As seen in Fig. 31, the grid resolution is increased near the walls to resolve the boundary layer. The maximum wall distance of the wall nearest cell (in the region of highest wall shear) is $z^+ < 1$. The grid point spacing increases away from the walls, but remains the same in the streamwise x and spanwise y direction. In the middle of the recycling inflow subsection (enclosed by the two black planes in Fig. 30), the grid point spacing is $\Delta x^+ \approx 33, \Delta y^+ \approx 22, \Delta z^+ \approx 11$. The effect of unresolved grid scales (sub grid scale viscosity) is accounted for by filtering the equations, which is done by multiplying the Lagrange coefficients with a filter function. In this study, the interpolants of order 11, 12 and 13 are multiplied with a quadratic filter function with a maximum at order 11 such that the last mode is reduced by 5%.

The solution at each time step is considered converged when the residuals for pressure/continuity reach 10^{-6} and those for velocity and temperature 10^{-8}. For a resolution convergence study, increasing the polynomial order would change the filter width because it is coupled to the grid spacing when the number of filtered modes is kept constant. This is similar to eddy diffusivity LES on finite volume meshes.

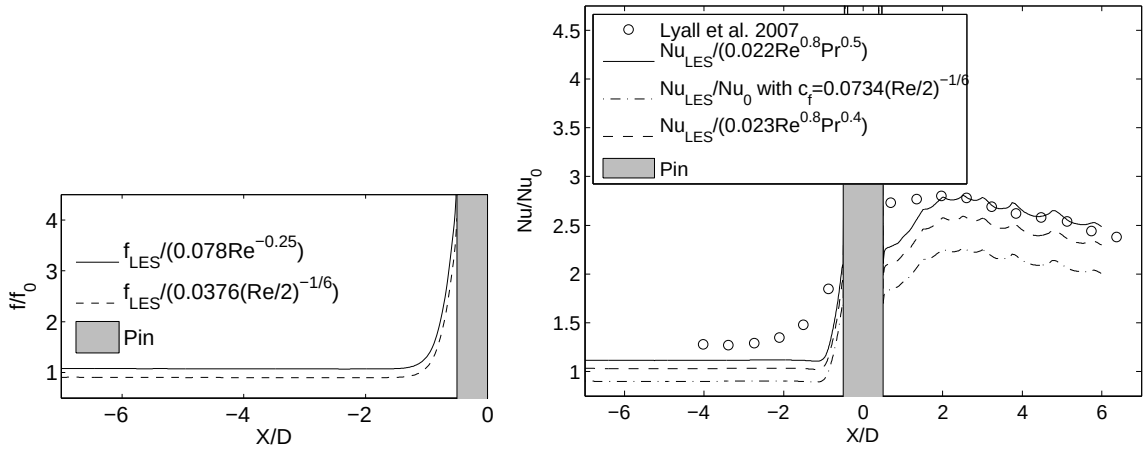

Fig. 32.: Left: The local, pitch-wise averaged friction factor augmentation is plotted as a function of streamwise distance. The pressure data is normalized with different baseline correlations. Right: The local, pitch wise averaged Nusselt number augmentation compared to experiments is plotted as a function of streamwise distance. The temperature data are normalized with different baseline correlations.

Estimating convergence towards a grid independent solution is thus prohibited as pointed out by Celik et al. (2009) [27]. Since no convergence study can be presented, validation against experimental values becomes even more important.

D. Results

1. Baseline

To validate the LES study against experimental results, friction factor and Nusselt number augmentation (in comparison to the unobstructed channel) are evaluated (see Fig. 32). The friction factor correlation that gives higher augmentation values is used in Lyall et al. (2007) [20]. It is expected to be valid for square channels even though

is was developed for circular cross sections if the Reynolds number is based on the hydraulic diameter. Patel and Head (1969) [28] show that this concept breaks down for channels with high aspect ratios. They developed another correlation (valid for $3000 < \mathrm{Re_C} < 10^5$, where $\mathrm{Re_C}$ is based on the channel height). Normalizing the CFD results with this corrleation leads to a lower augmentation, as shown in Fig. 32, left. The desired result ($f/f_0 = 1$) is within a 6%-7% range between the two correlations.

Fig. 32, right, shows a comparison of the pitch wise (y) averaged Nusselt number augmentation on the channel wall to experiments. Downstream of the pin and when using the same Nusselt correlation as in the experiments (from Kays and Crawford (1980) [26], $\mathrm{Nu_0} = 0.022\mathrm{Re}^{0.8}\mathrm{Pr}^{0.5}$), the agreement is quite good. Upstream, the desired value of $Nu/Nu_0 = 1$ is achieved when using the Dittus-Boelter correlation from Incropera and DeWitt (2002) [29]. For completeness, another baseline heat transfer correlation is shown when using the friction factor for high aspect ratios defined by Patel and Head (1969) [28]. The differences can be explained by geometry, uncercertainty and different turbulence conditions (for example, Lyall et al. (2007) [20] used sand paper to trip the boudnary layer far upstream of the measurement location, where the computation used smooth walls).

The orthogonal expansion was computed within a box enclosing all 3 pins, extending 3D upstream of the pins and 5.75D downstream. Two data sets were used: a small one spanning approximately one lift cycle (19 samples) and one for the entire flow time of approximately 13.3 seconds (a total of 443 samples). The resulting time basis functions from cases are qualitatively similar and are shown in Fig. 33 for the larger sample. Mode 0 shows the mean flow in x and an increase in mean temperature due to heating the endwalls. The velocity funtions of the higher non-zero modes show the time trace of flow components responsible for lift and drag. Mode 7 is the first mode with a non-zero temperature function. Modes one to six, which are potentially

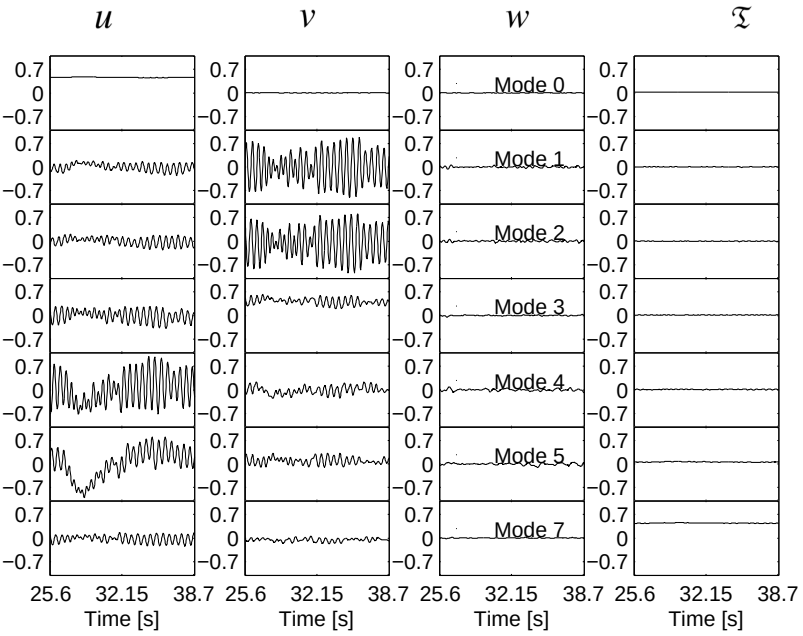

Fig. 33.: The plot shows time eigenfunctions $\Psi_i^k(t)$ of 8 modes for velocity (3 left) and temperature (right), scaled for better visualization. Mode 7 is the first mode with a non-zero temperature function. The stream wise and pitch wise velocity functions of modes one, two, four and five closely resemble the time history of lift and drag.

wasteful in terms of turbulent heat transfer, contain 32.14% of the total energy in all non-zero modes. To further distinguish between useful and non-useful modes, the integrals from the enthalpy-based analysis (Eqn. (2.38)) are evaluated for modes one to ten and are shown in Fig. 34. Globally, mode combination 7/7 has the highest positive heat transfer contribution. Higher heat transfer is desired in this application since the internal passage is intended to cool the blade walls.

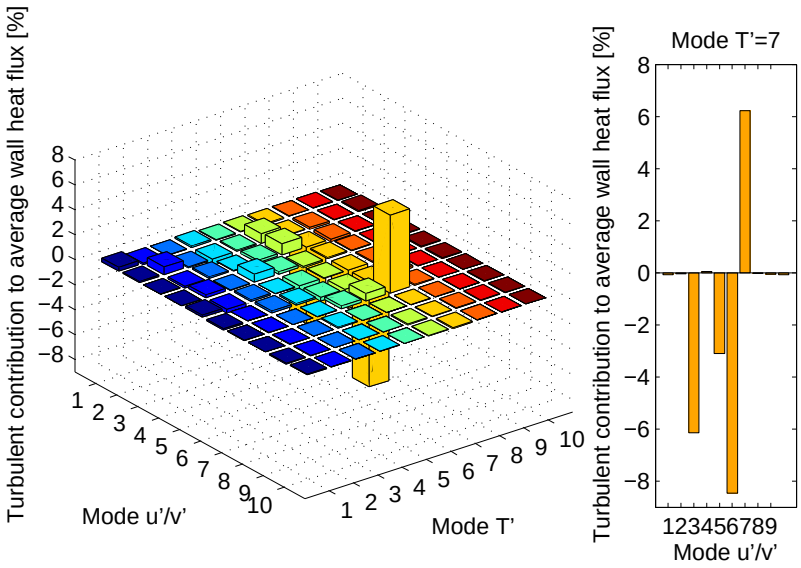

Fig. 34.: The plot shows a ranking of mode combinations with respect to their heat transfer contribution (see Eqn. (2.38)). Mode combination 7/7 has the highest positive result.

2. Contouring the endwall

As seen from the evaluation of orthogonal basis functions, the scalar mode 7 has the highest positive heat flux contribution (as desired for cooling the blade wall). In order to test whether this information can be used to improve heat transfer while at the same time increasing pressure drop by as little as possible, it might be beneficial to stimulate that mode such that it contains more energy, climbs up the OD spectrum and replaces lower order modes that are identified as wasteful in terms of heat transfer. One possible approach is to contour the domain endwall to ressemble an isosurface of a given mode value. The scalar mode threshold which determines the surface elevation in this case needs to be high enough to capture important spatial features, but should not be too high to avoid contracting the channel. The latter would result

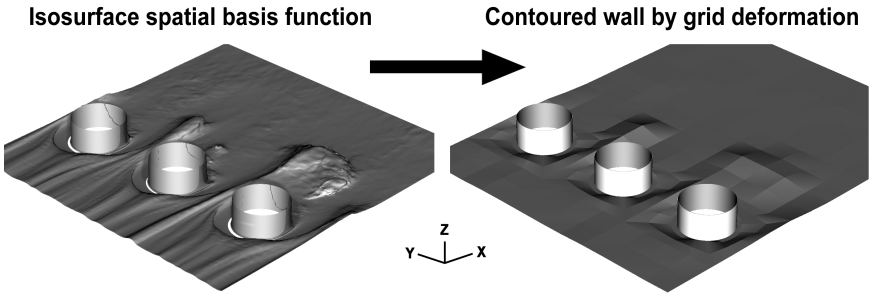

Fig. 35.: The left figure shows an isosurface at ≈ 13% of the maximum value of scalar mode 7. The right plot shows the resulting contoured endwall of the computational domain, which is a first order approximation in the sense that only element corners were deformed and grid points in between linearly interpolated.

in increasing heat transfer merely by globally accelerating the flow. Fig. 35, left, shows the chosen isosurface at a certain fraction of the absolute maximum of scalar mode 7. The elevation of this surface over the bottom endwall was used as a basis for the wall contour: by post-processing the spatial eigenfunction mode 7, the wall normal coordinate (Z) was saved of every grid point on which the scalar value of mode 7 fell within a given tolerance of the desired isosurface value (13%±1.7% of the absolute maximum of scalar mode 7). From those points, the lowest Z-values were chosen to lift the element corners of the smooth bottom wall. The Gauss-Lobatto grid points between element corners are then interpolated with a first order function. This deformation was applied symmetrically to bottom and top wall of the domain. As seen in Fig. 35, right, which shows the deformed endwall of the computational domain, this leads to sharp edges. Due to the corseness of the element mesh, it is only an approximation of the smooth surface in Fig. 35, left.

Another representation of the contoured endwall is given in Fig. 36. The lines

mark the new wall contour sliced normal to the streamwise direction. Upstream of the pins, the channel is only contracted, using a fairly flat, horizontal profile. This decreases the flow area by about 11.3%. Approaching the pin in the streamwise direction, the profile then drops towards the circular pin bottom and forms a trough around it where the stagnation horseshoe vortex is located. Between the pins (at $X/D = 0$), the trough sides form a ridge with a flat top, located in the middle of the pins. Those ridges become sharper downstream and stay at the same height for about one pin diameter. Then, two ridges decrease towards the undeformed profile and the remaining ridge widens at the top to form a bump. The spanwise averaged elevation of the wall stays on a constant level in the wake of the pins and yields a flow area (cross sectional) reduction of 5.7%. The deformation then decreases to a horizontal profile, resulting in 2.5% area reduction downstream of $X/D = 2.6$ (not shown in Fig. 36). Overall, the contoured endwall increases the top and bottom wall area available for heat exhange by $\approx 0.31\%$ and can be neglected which allows keeping the specific heat flux boundary condition the same for the smooth and contoured case.

After recording data from the smooth wall case in a statistically stationary state, the endwall contour is applied at top and bottom and the computation is restarted from some earlier point in time. This is done by mapping the existing smooth case field (including temperature) to the deformed domain grid point by grid point, without interpolation. The simulation is run for the same flow time so that a comparison can be made. Fig. 37 shows lift and drag coefficients on the middle pin of the smooth wall case (left) and the contoured wall case (right). There is a strong correlation between lift amplitude and drag in both cases, but the overall drag coefficient is slightly higher in the contoured case. As indicated by a significant decrease in lift on the middle pin of the smooth case, the vortex shedding breaks down for some time and a relatively wide and long wake develops. This behavior cannot be seen in the contoured case,

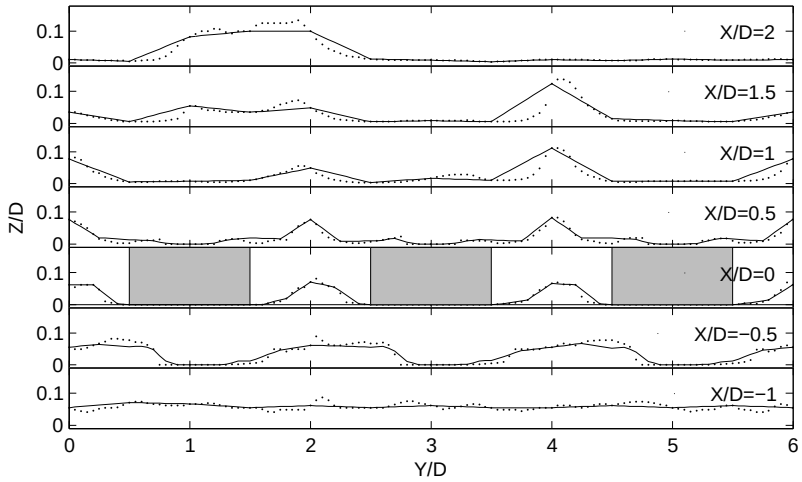

Fig. 36.: The plot shows the endwall contour in spanwise slices at different streamwise locations X. The pin bodies at X/D=0 are shown in gray. The dotted lines represent a deformation involving all grid points as opposed to only the element corners with linear interpolation (solid line). For this study, the linear interpolation is used.

where the pins are somewhat isolated from each other by the ridges in the endwall. It is further hypothesized that the horseshoe vortex oscillation is dampened due to the trough around the pin base, which could also stabilize the flow in the wake.

A key goal of this heat exchanger optimization is to increase surface heat transfer without increasing the pressure loss of the passage. In order to judge the pressure penalty that is paid for changing heat transfer, the total pressure drop as a function of streamwise distance is computed from the wall static pressure, averaged in the spanwise (y) direction, and the dynamic pressure. For the latter, only the mean flow velocity in the streamwise direction is used since both spanwise and pitchwise velocity are zero in the mean. The streamwise velocity is derived from the volumetric flow rate in the recycling section (which is the same for the smooth and contoured case) devided by the cross sectional area at any given streamwise distance. Fig. 38 shows

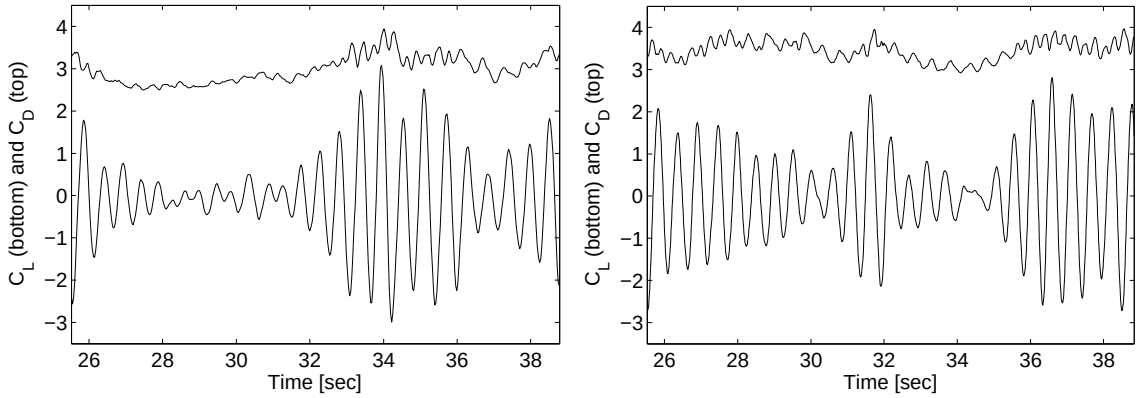

Fig. 37.: The left plot shows lift and drag coefficient of the middle pin from the smooth wall case as a function of flow time. The vortex shedding appears to break down, generating a relatively wide wake and lower lift, but it recovers thereafter. In comparison, the lift on the middle pin from the contoured case, right, shows that the time periods of lower lift are shorter, indicating a faster recovery.

the total pressure for both cases. In the smooth wall case, there is an almost constant total pressure in the recycling inflow section. The pressure then drops approaching the region where the stagnation horseshoe vortex is active. At $X/D = 0$, where in the given geometry the cross sectional area of the channel is reduced by half due to the pin bodies, the total pressure recovers, but a significant decrease follows due to mixing and losses in the pin wake. The pressure slightly recovers further downstream. For the contoured case (line with circles in Fig. 38), one can see a disturbance in the pressure curve at $X/D = -2$. This is where the first deformed wall grid points are located. Between $X/D = -2.5$ and $X/D = -2$, the wall is formed as a sharp ramp which leads to losses possibly due to flow separation. Compared to the smooth case, the pressure drop in the pin wake is larger. Towards the channel end, the total pressure difference remains constant and the pressure recovery phase appears to be

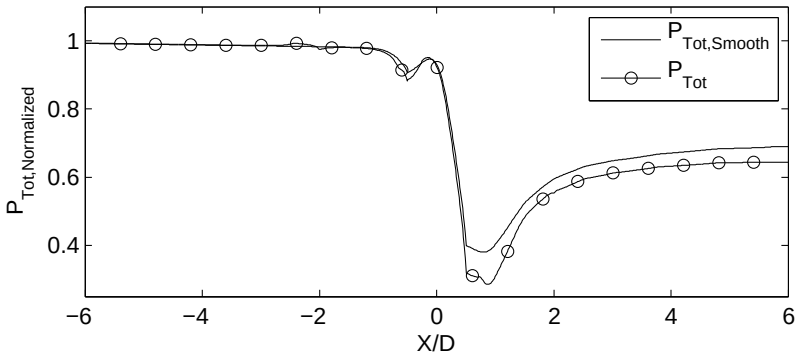

Fig. 38.: The plot shows the total pressure (wall static pressure and dynamic pressure derived from the mean streamwise velocity) normalized with total inlet pressure as a function of streamwise distance. The total pressure loss of the contoured case is higher than for the smooth wall, losses mainly occur in the mixing zone downstrem of the pin row. Upstream (in the region of the leading edge horseshoe vortex), the pressure loss is slighty lower in the contoured case.

completed.

The local effectiveness of the wall contouring can be judged by comparing the friction factor change to heat transfer augmentation. Fig. 39 allows this comparison by plotting the local Nusselt number augmentation based on spanwise averaged wall temperature of the contoured case over the smooth case as well as the friction factor augmentation. The highest local heat transfer increase takes place at the start of the wall contour, at $X/D = -2.5$. The friction factor, which is based on wall static pressure, drops in this region due to the acceleration of the flow, but increases above the smooth wall case after the ramp, indicating losses. Another drop can be seen approaching the pin centers ($X/D = 0$), where the cross section is reduced due to the pin bodies. The friction factor remains almost constant thereafter. The heat

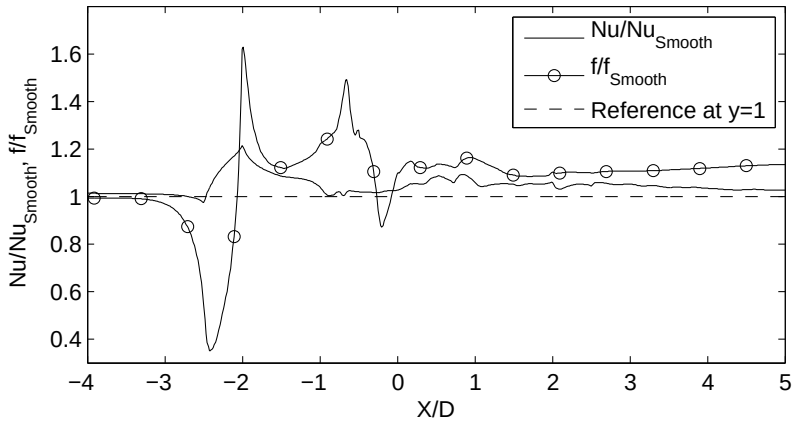

Fig. 39.: The plot shows the Nusselt number based on spanwise averaged wall temperature of the contoured case over that of the smooth case, solid line. The circled line shows the friction coefficient as derived from the pressure drop between a certain streamwise location and the inlet plane, again for the contoured case over the smooth case.

transfer augmentation is highest in the ramped wall section, but this is only due to accelerating the flow which has the effect of increasing the Reynolds number. The highest heat transfer increase due to changing the pin flow by wall contouring is seen between $X/D = 0$ and $X/D = 1$. Care needs to be taken when comparing the friction and heat transfer augmentation at a specific streamwise location: there can be delays in pressure recovery and the wall static pressure does not always equal the mean planar pressure. Further, both values are integral quantities in a sense that the friction factor is based on pressure differences between a varying streamwise location and the (fixed) inlet plane and the Nusselt number is based on a reference temperature obtained from an integral energy balance.

To assess the efficiency, the overall pressure drop across the array can be com-

Table II.: Mean Nusselt number change of the pin fin array comparing the smooth to the contoured case.

Area for average	Pin and endwall	Only endwall
-D to D	2.63%	4.21%
-2.5 D to 2.5 D	5.02%	6.26%

pared to the mean Nusselt number augmentation. Table II shows the area averaged Nusselt number augmentation (relating the smooth wall case to the contoured case) for the endwall only and combined from pin surface and wall. The contouring has a higher effect when combining pin and wall heat transfer and when using a larger area for the evaluation. The experimental values found in Lyall et al. (2007) [20] further enable a comparison to the Nusselt number augmentation that could be achieved by just changing the Reynolds number (bulk velocity). The published data indicate that the averaged, combined Nusselt number augmentation for pin and wall remains constant over the Reynolds number range and the area in question. For an increased Reynolds number that would yield a 5.02% increase in heat transfer, the friction factor would be raised by 13.22%, where this value was found from a second order interpolation of the data plotted in Lyall et al. (2007) [20]. The friction factor augmentation (based on total pressure and measured 8.25D upstream and 5.75D downstream of the pin row) due to the wall contouring in this study is 14.76%. The orthogonal decomposition analysis shows that the energy fraction contained in the highest modes with zero temperature basis function compared to all modes with $\alpha^k \neq 0$ decreases from 32.14% (smooth case) to 31.35%. The highest non zero temperature mode is 8 in the contoured case instead of 7.

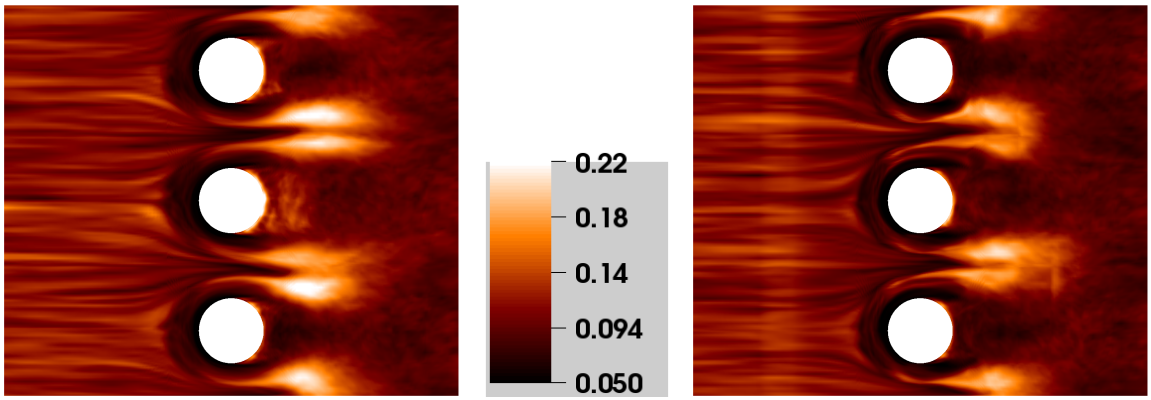

Fig. 40.: The contour plots show temporal wall temperature RMS from the smooth case (left) and the contoured case (right).

Another important aspect of part durability besides overall cooling effectiveness is the temperature fluctuation in the material. Fig. 40 shows the temporal RMS of wall temperature comparing the smooth to the contoured case. Particularily in the recirculation zone close to the trailing edge of the pin (most notably downstream of the middle pin), the RMS have decreased. The region of intense fluctuations in the intersection of the pin wakes is shortened, possibly due to the stabilizing effect the wall contouring has on the vortex shedding (see Fig. 37). In the horseshoe vortex region, there is an increase in temperature RMS compared to the smooth case, but the fluctuation levels are overall more uniform. Similarily comparing the smooth to the contoured case, the spatially resolved heat transfer augmentation is shown in Fig. 41. The increase in heat transfer augmentation is most notable immediately downstream of the pins, where the span wise uniformity is also greater.

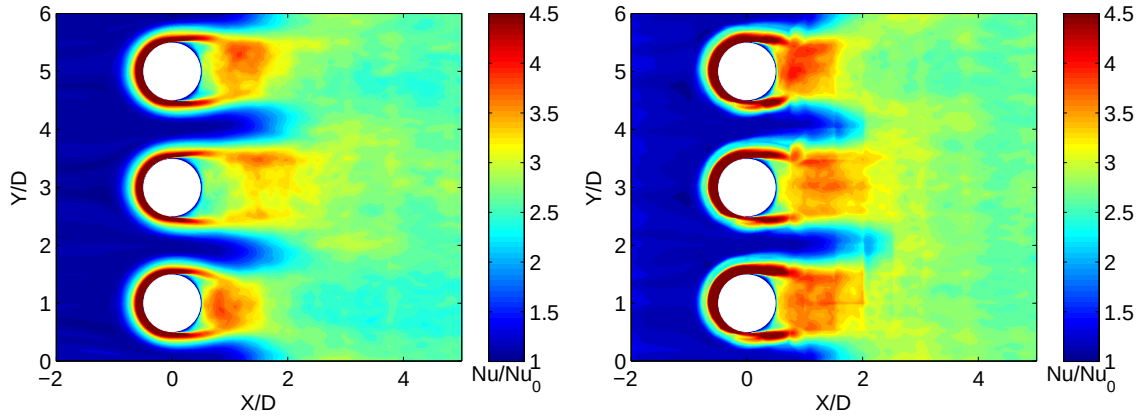

Fig. 41.: The heat transfer augmentation of the undeformed geometry (left) and the wall contoured case (right) is shown. The same definition for unobstructed channel Nusselt number Nu_0 as in [20] was used.

E. Conclusion

Unsteady heat transfer in a single row pin fin heat exchanger is examined with LES. Comparison of integral quantities friction and Nusselt number show good agreement. The data are then analyzed with an orthogonal decomposition technique based on temporal correlations and including internal energy. Since the low order (high energy) modes show a zero amplitude of temperature basis functions, the a mode combination ranking methodology based on enthalpy is development. This confirmed that the mode with the highest basis function amplitude is most relevant to turbulent heat transfer. An isosurface of this mode's temperature basis function is then used to deform the domain endwall, leading to a maximum decrease in cross sectional area of about 11%. The wall contour forms a trough around the pin body upstream of the separation zone and develops sharp ridges at the interface of the wakes. This arrangement seems to stabilize the vortex shedding as can be seen from a more uni-

form lift coefficient history on the middle pin. Depending on the averaging area, the mean heat transfer augmentation increased between 2.6% and 6.2%. If a heat transfer augmentation increase of 5% was to be achieved by merely increasing the Reynolds number, the friction factor augmentation would have been the same as due to endwall contouring. This is remarkable given that the contoured surface is only a first order approximation of the mode's isosurface, which is not smooth. Even though the number of low order modes with near zero temperature amplitude has increased, the amount of energy contained in them fell from 32.14% to 31.35% of all non-zero modes.

CHAPTER VI

DIRECT NUMERICAL SIMULATION AND ORTHOGONAL DECOMPOSITION ANALYSIS OF TURBINE VANE ENDWALL HORSESHOE VORTEX DYNAMICS AND HEAT TRANSFER

A. Introduction

Gas turbine engines are responsible for a considerable part of the world's electricity generation and most aviation transport. Even though the emission of green house gasses through burning of fossil fuel is likely to become more expensive or even restricted in the future, the gas turbine will continue to play a significant role in energy conversion and propulsion. Unfortunately, it is a very complex system that is still not fully understood and a large potential for efficiency increase exists.

To improve our understanding of the complex physics involved, spatial and temporal highly resolved measurements are needed. Direct numerical simulation (DNS) offers this opportunity without being dependent on turbulence modeling. The acquired data can be analyzed through advanced post processing techniques to observe structures, interactions, and correlations, specifically regarding turbulent convective heat transfer.

In gas turbine endwall cooling, turbulent convection is impacted by secondary flow structures originating from the blade geometry. One example is the stagnating boundary-layer vortex, depicted in Fig. 42, left, which exhibits high spatial oscillations. This vortex is also responsible for a large amount of drag, and part failure due to melting, see Fig. 42, right. Gaugler and Russell (1984) [39] studied stagnating boundary-layer vortex flow in relation to turbomachinery by examining the boundary-layer vortex effects in a time varying manner. Through flow visualization

and surface heat transfer, they showed that high convective heat transfer coincides with the most intense vortex action. Laser doppler velocimetry measurements in the stagnation region of a first stage turbine stator vane were performed by Kang et al. (1999) [40]. The contours of turbulent kinetic energy indicate a peak in the turbulent kinetic energy at the same location of the horseshoe vortex center. Streamwise, lateral, and vertical root-mean-square velocity profiles show that the location of these peak values coincide closely with the center of the vortex. Only the peak streamwise fluctuations occurs slightly upstream of the vortex center. The fluctuations are much higher in the vortex region than in a canonical turbulent boundary layer. Similarily high levels are were shown previously by Devenport and Simpson (1990) [41]. It is believed that the unsteady motion of the horseshoe vortex accounts for the increased turbulence measured. Radomsky and Thole (2000) [42] present histograms of the probability density functions (PDF), which show two distinct peaks near the endwall, particularily in the vortex center. This indicates that the flow is oscillating or rather unsteady. The high turbulence intensities in combination with the unsteady vortex and wall generated turbulence greatly enhance the endwall heat transfer [42]. Effects of high freestream turbulence intensities on the endwall region were further studied by Gregory-Smith and Cleak (1992) [43]. The results showed that the mean flow field is not greatly affected by high freestream turbulence and high turbulence within the blade passage is present near the end wall. Spencer et al. (1996) [44] examined flow in an annular cascade of nozzle guide vanes. Using a transient liquid crystal technique to measure heat transfer, the horseshoe vortex was shown not to create a region of high heat transfer near the leading edge of hub endwall.

One challenge of computational simulations, particularly in the realm of gas turbines with widely varying flow regimes, is the formulation of appropriate inlet conditions. Here, it is desired to achieve a developing flat plate boundary layer subject

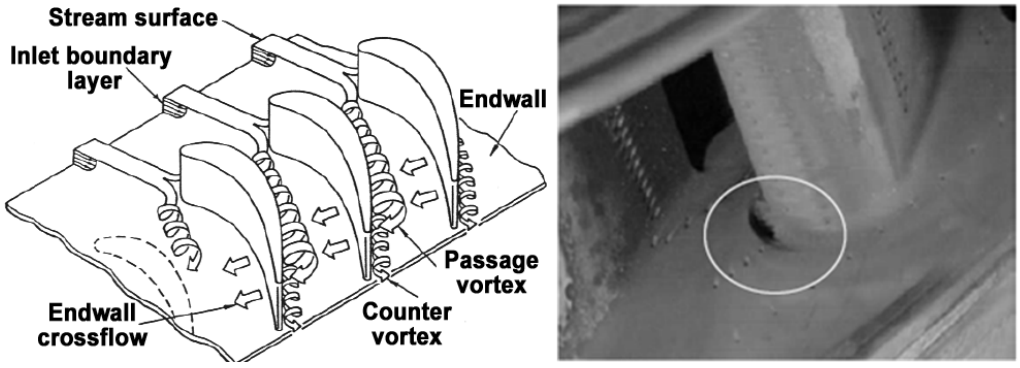

Fig. 42.: The horseshoe vortex rolls up from the stagnating boundary, depicted by Langston (2001) [45] (left). These secondary flow structures are responsible for melting because they drive hot combustion gasses towards the endwall (right, from Thole (2008) [46]).

to high free stream turbulence intensity and length scale. Exemplarily, two principal ways of generating inlet conditions are describe. Sadiki et al. (2003)[47] developed a pre-processing technique where inflow data is genreated beforehand from user defined Reynolds stresses. These data files then need to be read into the Navier Stokes Solver during run time, which makes this methid hard to implement preserving parallel efficiency. Jacobs and Durbin (2001) [48] have shown a way to describe elevated free stream turbulence at the inlet from Fourier modes that resemble grid turbulence. Even though their inlet conditions are based on some physical insight, they rely on random variables and are not free of divergence.

Direct numerical simulations deliver spatial and temporal highly resolved data that can be used for post processing beyond first and second order statistics. One such way is proper orthogonal decomposition (POD), where the flow is decomsposed into orthogonal basis functions. Ball et al. (1991) [13] apply POD to data from direct numerical simulation of channel flow in order to understand bursting and sweeping events in the internal turbulent boundary layer. Later, the same methodology was

used by Duggleby et al. (2009) [14] on a direct numerical simulation of pipe flow. Turbulent structures in the boundary layer could be linked to certain modes and the energy transfer between them better understood. Due to the more complex blade geometry, a direct computation of orthogonal functions is not efficient. An alternative method is shown in Aubry et al. (1991) [4], who demonstrate the equivalence of orthogonal basis functions derived from time and space autocorrelations. An application of this time based method is used in Handler et al. (2006) [5] to analyze the properties of turbulent channel flow when creating drag reduction via the use of polymers in the flow.

In this study, a time-dependent direct numerical simulation (DNS) of a 1st stage stator vane and endwall is performed to examine the structures and dynamics of the dominant horseshoe vortex and characterize its effect on endwall heat transfer. Although the Reynolds number examined (10,000) is lower than engine conditions, the vortex already exhibits strong aperiodic motions and any uncertainty due to sub-grid scale modeling is avoided in the DNS.

B. Numerical method

The incompressible Navier-Stokes equations are solved using a spectral element method (see Fischer et al. (2008) [3]). Heat transfer was incorporated by solving the energy equation as a passive scalar and matching the Prandtl number of air. The mesh consists of 94032 hexahedral elements. Within each, the solution is approximated by 7th order Legendre polynomials. The grid resolution provides a maximum wall distance of the wall nearest cell on the endwall of $z^+ < 1$. For improved stability, the last 2 modes of the Legendre polynomials are multiplied with a quadratic filter function such that the last mode is reduced by 5%. Employing spectral elements provides parallel

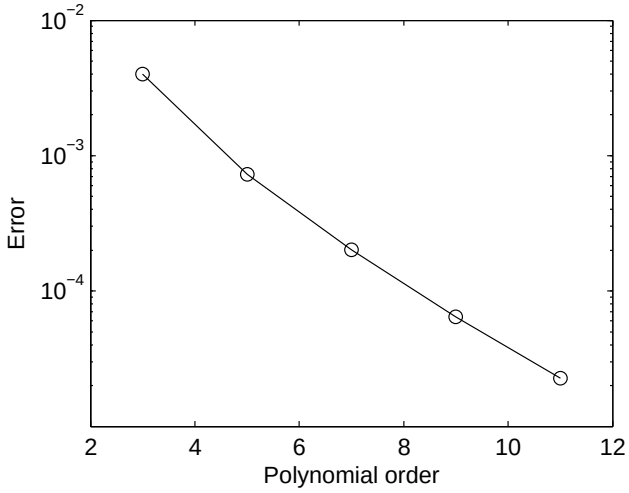

Fig. 43.: The error in total force magnitude on the blade is plotted as a function of solution polynomial order or grid resolution. Exponential convergence is obtained, the simulation was run at order 7.

efficiency, accuracy and exponential convergence. To show grid convergence, the total force magnitude on the blade was measured for 50 time steps and different Legendre polynomial order. The solution was always started from the same, fully developed field and force data were averaged over the last 40 steps. The deviation of force magnitude from the highest resolution is plotted as a function of polynomail order and shows exponential decrease, Fig. 43. Time discretization is done with high-order operator splitting methods and Tensor-product polynomial bases are solved using conjugate gradient iteration with scalable Jacobi and hybrid Schwarz/Multigrid preconditioner [49]. The time step was chosen such that the Courant number is always below two. Every 500 time steps, a data sample was saved for later post processing. A total of 150 samples were collected, spanning close to 18 flow throughs based on axial chord and free stream velocity.

A single blade in the cascade with periodic boundary condition in the pitchwise

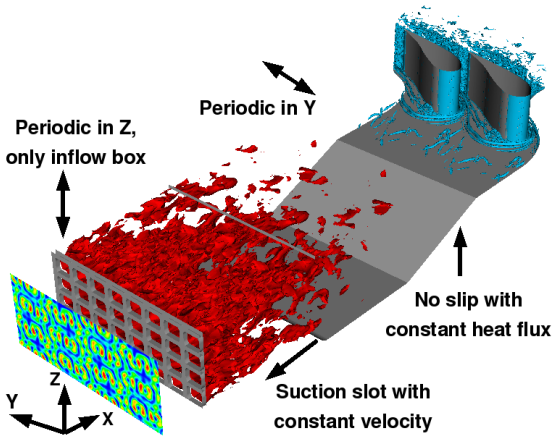

Fig. 44.: The flow domain consists of a single blade with periodic boundary conditions in the pitch wise direction. At the inflow plane, a divergence free vortex field is defined. Grid bars redistribute energy and the inflow parameters are controlled by geometric features such as ramp slope and length or domain length.

direction is considered. The bottom spanwise boundary is treated as a no-slip wall, where a constant specific heat flux is applied at $X/C > -1/3$. The outflow is located 0.75 C downstream (X direction) of the trailing edge. The inflow is placed about 4.60 C upstream of the blade stagnation including the turbulence generating section. A slip condition (stress free) is applied at the top, at half blade span.

1. Numerical domain and boundary conditions

At the inlet, at $X/C = -4.6$, a divergence free velocity field with multiple vortices is defined as shown in Walsh (1992) [38] (see Fig. 44). The streamfunction ψ of the velocity field is given by:

$$\psi = \frac{1}{4}\cos(3z)\sin(4y) - \frac{1}{5}\cos(5y) - \frac{1}{5}\sin(5z). \tag{6.1}$$

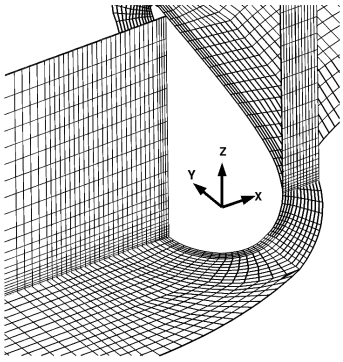

Fig. 45.: The element mesh is shown on the stagnation plane (X/Z) and the endwall (Y/Z). The mesh is refined near the walls.

Since the streamfunction also obeys $-\nabla^2\psi = \kappa\psi$, where κ is the Eigenvalue of the Laplacian, one can control freestream turbulence intensity and length scales by varying the amplitude and wavenumbers of the sine and cosine functions, respectively. As long as it is smaller then the open grid area, the average size of these eddies controls the length scale. Smaller vortices can be achieved by increasing the wavenumber. The inflow section is a doubly periodic (in Y and Z) box which extends to $X/C = -3.1$. At $X/C = -4.2$, an array of bars causes the redistribution of turbulent kinetic energy downstream from inflow plane across all three velocity components. The distance between grid and cascade can be changed during run-time and determines the decay rate. To maintain elevated levels of turbulence intensity inspite of the low Reynolds number, a forcing term has been added to the momentum equation which artificially decreases viscosity in the region downstream of the bars to the middle of the ramp. The mesh is refined in the wall normal directions around the blade and the endwall (see Fig. 45). Those additional element layers are introduced downstream of the inflow box, connected to it via a backward facing step. Since preliminary simulations indicated the accumulation of low momentum fluid in the trough, the step is made

porous and sucks fluid in the negative x direction. This avoids entrainment of low momentum fluid into the main flow when exiting the inflow box. The boundary layer is controlled by a ramp downstream of the step (extending from $X/C = -2$ to $X/C = -1$).

C. Results and discussions

1. Inflow characteristics

Since the blade geometry is a first stage stator vane, the incoming flow should have a relatively large integral length scale and turbulence intensity (Radomsky and Thole (2000) [42]). The inflow generation technique as described above is calibrated to match some of the parameters described therein and in Knost et al. (2009) [50]. While the boundary layer displacement thickness compares favorably, the turbulence intensity (see Fig. 46, top) is closer to the lower one of the two cases examined experimentally. The integral length scale is lower as well. Upstream of the turbine cascade, the turbulent fluctuations are nearly isotropic. The turbulence intensity is around 2.1%, which is achieved by the vortex-containing inflow velocity field in combination with a forcing function acting against the dissipative terms of the momentum equation. The profiles in the pitch wise direction of those quantities are fairly homogeneous (see Fig. 46, bottom).

2. Vortex dynamics

Velocity contour lines in combination with a velocity vector plot are shown in Fig. 47, left. Several leading edge horseshoe vortices are identified, where the most intense one is found nearest to the vane. The smaller ones are located further upstream and closer to the endwall. The main vortex is strong enough to accelerate free stream

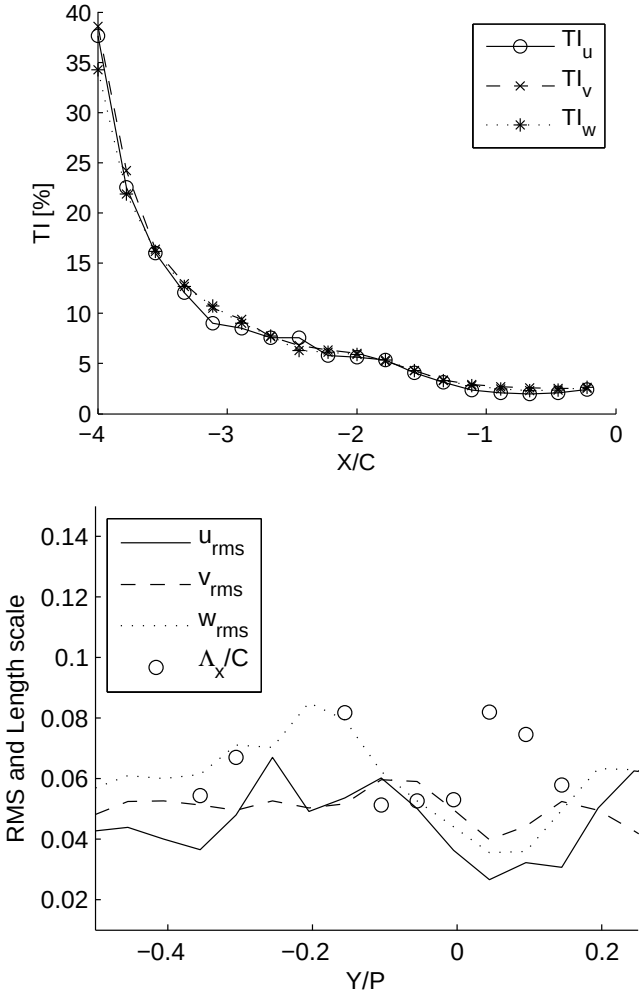

Fig. 46.: The top plot shows the decay of turbulence intensity from the turbulence generating grid to the cascade leading edge ($X/C = 0$). The bottom plot shows the velocity RMS normalized with free stream velocity as well as normalized streamwise integral length scale across the pitch at a span wise location of $Z/S = 0.25$ and $X/C = -1/3$.

fluid towards the endwall, pushing it against the main flow. The incoming flow does not have enough momentum to suppress the formation of those secondary leading edge vortices. These smaller vortices might not be as pronounced in the experimental results due to the much higher experimental Reynolds number. The vortex location in the lower Reynolds number numerical study is shifted further upstream and closer to the endwall. The center of the strongest vortex does not coincide with the peak location of turbulent kinetic energy (Fig. 47, right). It is located further downstream and away from the endwall compared to the mean vortex center. Compared to the experiments, the peak location is shifted slightly further upstream. The distance between the location of peak kinetic energy and mean vortex center is thus greater than in the higher Reynolds number experiments. The overall level of turbulent kinetic energy is about one third of what is shown in Radomsky and Thole (2000) [42].

The high resolution of the simulation allows tracking the stagnation vortex core in space and time. The vortex center has been determined by computing the Lambda-2 vorticity domainwide and then tracking the point where its magnitude is the highest on the stagnation plane and the corresponding vortex the largest. From the time resolved visualization, it is seen that the leading edge vortices oscillate, vanish and also merge. Thus most sharp steps in Fig. 48 result from one vortex vanishing while another one has already formed at a different location. Once the new vortex is stronger, the tracking algorithm locks onto it. In Fig. 48, left, this can be seen at several time instants when the vortex core approaches the blade at $X/C = 0$ (sawtooth pattern at the beginning and two distinct peaks of the circled curve at the end). Due to the free stream momentum, the vortex is accelerated towards the vane stagnation, then pushed towards the endwall and vanishes. The core movement towards the blade is initiated by a movement away from the endwall, see Fig. 48,

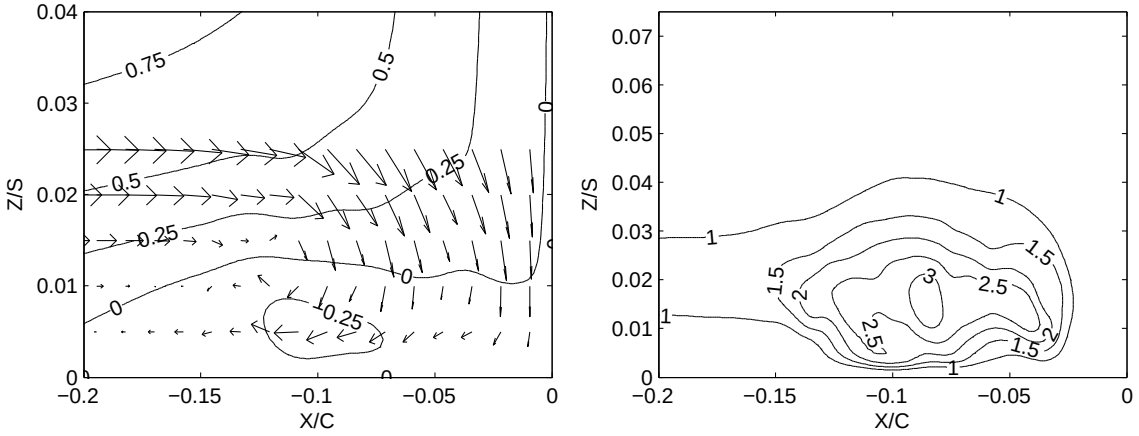

Fig. 47.: The left plot shows contours of mean streamwise velocity and vectors of average in plane velocity components on the stagnation plane. Contours of turbulent kinetic energy, normalized by the free stream velocity squared and scaled by 100, is shown left. Data were taken on the stagnation plane.

right. Two identical trajectories towards vortex destruction can be seen that form an upper bound to the core movement space. If those curves were completed to form a circle, the region of highest turbulent kinetic energy would roughly coincide with its center. The mean vortex position can be seen at the lower left corner of Fig. 48, right, where the point density is the highest.

3. Heat transfer

Endwall heat transfer in terms of Stanton number is shown in Fig. 49. It is highest slightly south of the stagnation point and in the wake of the blade. One can also see a deflection of a high heat transfer zone within the passage towards the suction side (see isolines 10 and 18), following the trace of the passage vortex. Upstream and between the vanes, where no secondary flow structures increase mixing, an isoline

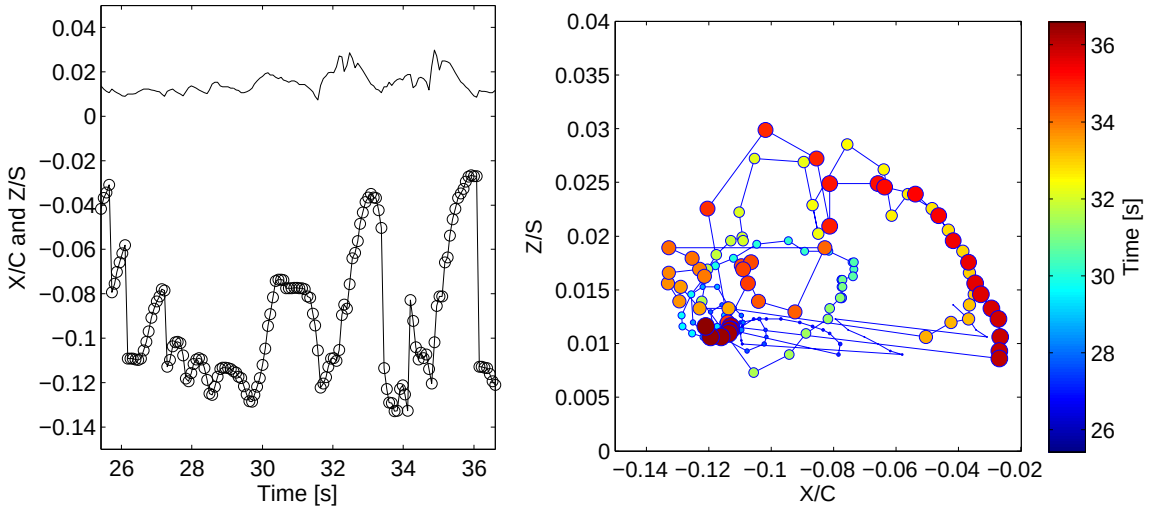

Fig. 48.: The left plot shows the strongest stagnation vortex center's trajectory over time in the spanwise (top) and streamwise (bottom, circled line) direction. The circle size and color changes with flow time - the darker and bigger, the later in time is the point. Combining the plots, the vortex trajectory on the stagnation plane as a function of flow time is shown right.

bends east towards the blade passage, indicating higher heat transfer due to flow acceleration. Compared to the experiments, the computational heat transfer values are higher upstream of the vane but roughly the same in the blade wake. These deviations are expected since the experimental Reynolds number was much higher. Fairly high fluctuations in surface heat transfer in the horseshoe vortex region can be seen in Fig. 50. The highest dynamics (around 34 s flow time) coincide with the highest dynamics of the largest horseshoe vortex, Fig. 48, left. The impact of turbulent flow structures on endwall temperature is also visualized in Fig. 51. The figure shows isosurfaces of coherent vorticity, visualizing multiple horseshoe vortices that merge while travelling through the passage. The wall temperature decreases below these structure.

4. Orthogonal decomposition

To focus the orthogonal expansion on the stagnation and passage vortex, only flow data between $X/C = -1/3$ and the blade trailing edge are considered. Due to memory restrictions, the solution polynomial order for all orthogonal postprocessing was reduced from seven to five. The resulting time eigenfunctions are shown in Fig. 52. The first four modes (zero to three) are not shown since they do not contain any time-varying parts, but instead constitute the average for all signal components. There is no relation between mode number and signal component, thus all four modes are needed to construct a complete average field. For validation purposes, Fig. 53 compares the average in plane velocities in the stagnation plane superimposed on a contour of mean flow temperature derived from averaging all data samples (left) to the reduced order field containing the sum of modes zero to three (right). The plots are almost identical and slight deviations can be explained by the different grid resolution used for the full scale simulation and the orthogonal decomposition postprocessing.

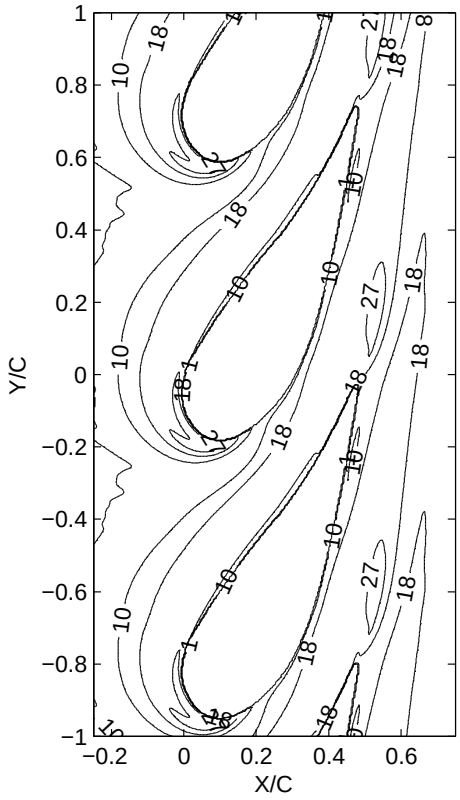

Fig. 49.: Contours of Stanton number on the passage endwall, scaled by 1000. The computational domain is copied three times along the periodic direction for better visualization.

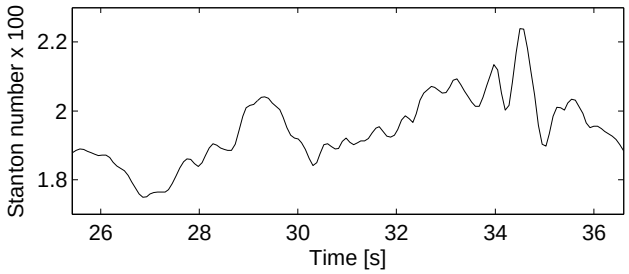

Fig. 50.: The area averaged Stanton number between $-0.15 < X/C < 0$ and $-0.1 < Y/P < 0.1$ is shown as a function of simulation time.

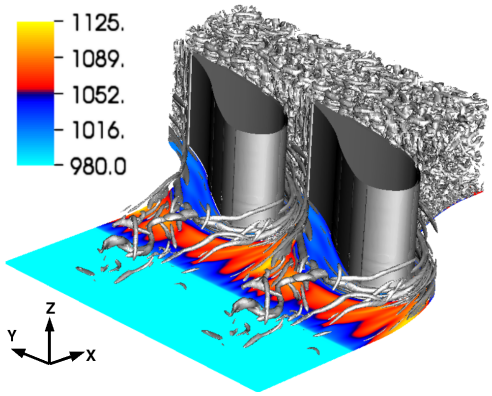

Fig. 51.: The plot shows an isosurfaces of Lambda-2 vorticity (grey) and endwall temperature. The computational domain has been copied once along the periodic direction for better visualization.

The different scales of temperature and velocity basis functions apparent from Fig. 52 do not contain useful information and can be attributed to the signal non-dimensionalizing and weighting. The dynamical information of each mode, however, can be analyzed: most notably, the pitch wise (y) component has higher fluctuating amplitudes than the other three components. They are the highest in mode eight. Within the shown modes, the frequency of fluctuations is qualitatively the same. The temperature basis function of mode five has a fairly distinct, broad peak towards the end of the simulated time, which coincides with the stagnation vortex core location closest to the blade (peak of circled line at time 36 s in Fig. 48, left). At the same time instant, the time function of that mode for the stream wise velocity has a fairly steep decrease. The spatial eigenfunction of mode five is shown in Fig. 54, left. All spatial basis function contours area built by plotting isosurfaces at $\varphi^k(\vec{x}) = -2$ (blue) and $\varphi^k(\vec{x}) = 2$ (red), which is on average 15% of their maximum value. Mode five has the closest resemblance to the passage vortex. This mode, unlike the other high

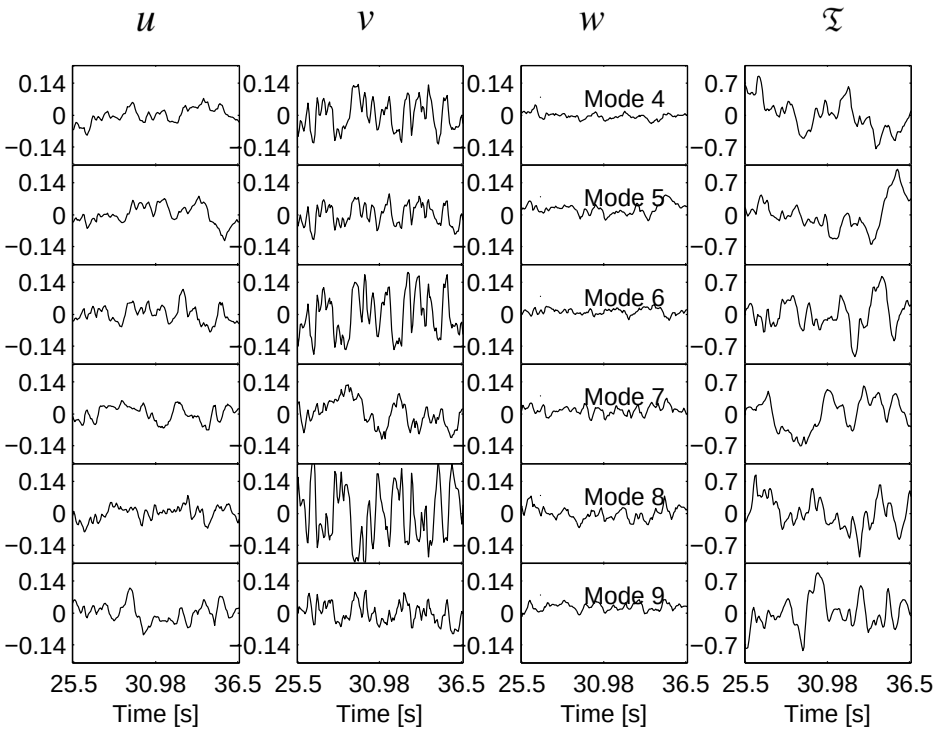

Fig. 52.: The orthogonal time basis functions from an analysis covering the domain from $X/C = -1/3$ to the blade trailing edge.

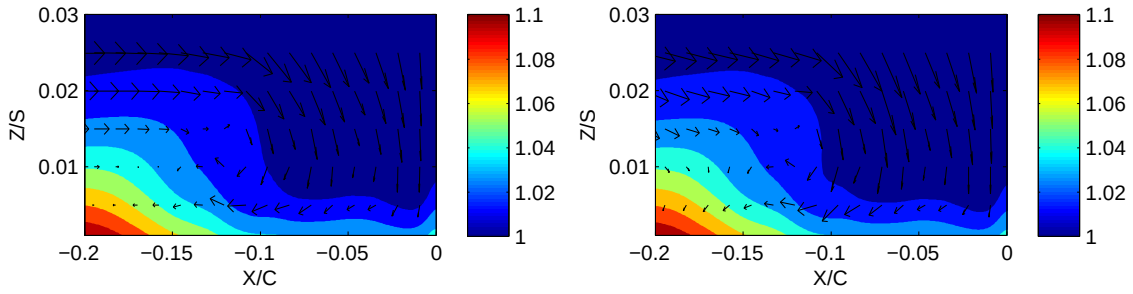

Fig. 53.: The left plot shows the average in plane velocity vectors superimposed on a contour of fluid temperature normalized with inlet temperature derived from ensemble averaging all data samples. The right plot shows a reduced order representation containing the sum of modes zero to three.

energy ones, is not very active in the region of the horseshoe vortex.

In order to judge different mode's contribution to heat transfer in the stagnation area close to the vane, a single mode heat transfer ranking was performed based on the presented time orthogonal basis set in the region from $X/C = -0.5$ to the vane front, and from $Y/P = -0.4$ to $Y/P = 0.4$. The resulting matrix is shown in Fig. 55. Modes six and eight have the highest positive contribution to turbulent wall heat flux, increasing heat transfer. The spatial basis function of mode eight seems to capture the heat transfer dynamics in the region of high average Stanton number south of the stagnation point, compare to the figure on page 101. The spatial eigenfunction of mode six, depicted in Fig. 54, right, has one of the most distinctive regions of activity in the horseshoe vortex area among the high energy modes, but it is still relatively small compared to the structures in the mean flow. The peak in temperature basis function of mode six (at time 34.58 s) coincides with the highest gradient of horseshoe vortex core movement in the wall normal direction. This is the time when the leading edge vortex upstream of the blade accelerates away from the wall into the free stream and gets advected towards the blade (compare to 34.58 s in Fig. 48 on page 99, left).

D. Conclusions

A direct numerical simulation of a first stage stator blade with less than engine condition $\mathrm{Re} = 10,000$ was performed. The high intensity, high length scale combustor exit flow was modeled with a vorticity-containing inflow and geometric mesh features, with which a turbulence free stream intensity of close to 3% and a stream wise length scale of around 0.08 C could be achieved. The leading edge horseshoe vortex appears not to be one single structure, but instead multiple that move, vanish and merge.

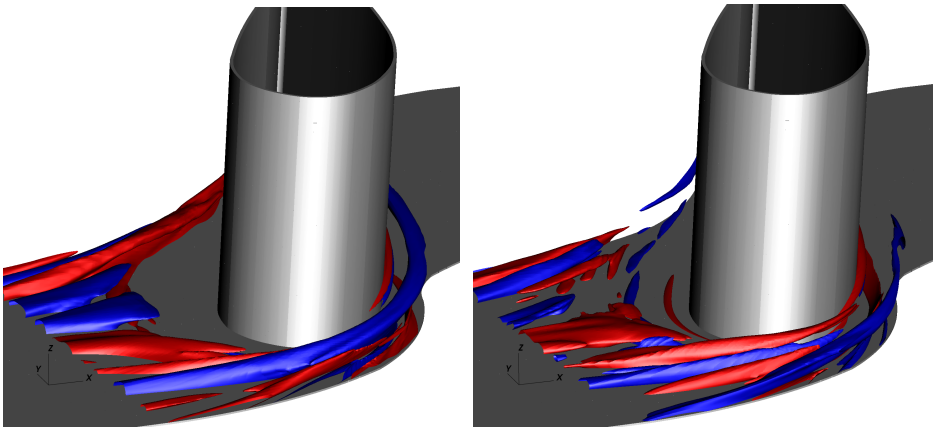

Fig. 54.: The spatial eigenfunctions of mode five (left) and six (right) are plotted. A value of -2 was chosen for the blue isosurface and +2 for the red.

The dynamics of the strongest leading edge horseshoe vortex were observed with a core tracking algorithm applied on the stagnation plane. This showed that the vortex has the tendency to travel away from the endwall, towards the blade where it then gets pushed back down and vanishes. Two almost identical core trajectories along this path were observed. An orthogonal decomposition based on time was performed on the flow data. To reconstruct an averaged field, the first four modes need to be used. Their time functions are constant. The time instant of the largest and broadest peak in the temperature and stream wise velocity time basis function of mode five is identical to the time when the vortex is closest to the blade. The spatial eigenfunction of this mode represents the passage vortex and is not active in the horseshoe vortex region. This mode is however, the biggest contributor to negative turbulent heat transfer in a control plane upstream of the leading edge. The highest positive heat transfer contribution is made by modes six and eight. Two peaks in their time basis function coincide with the time instant when the gradient in vortex core wall normal velocity is highest. The spatial basis function of mode six has the most dis-

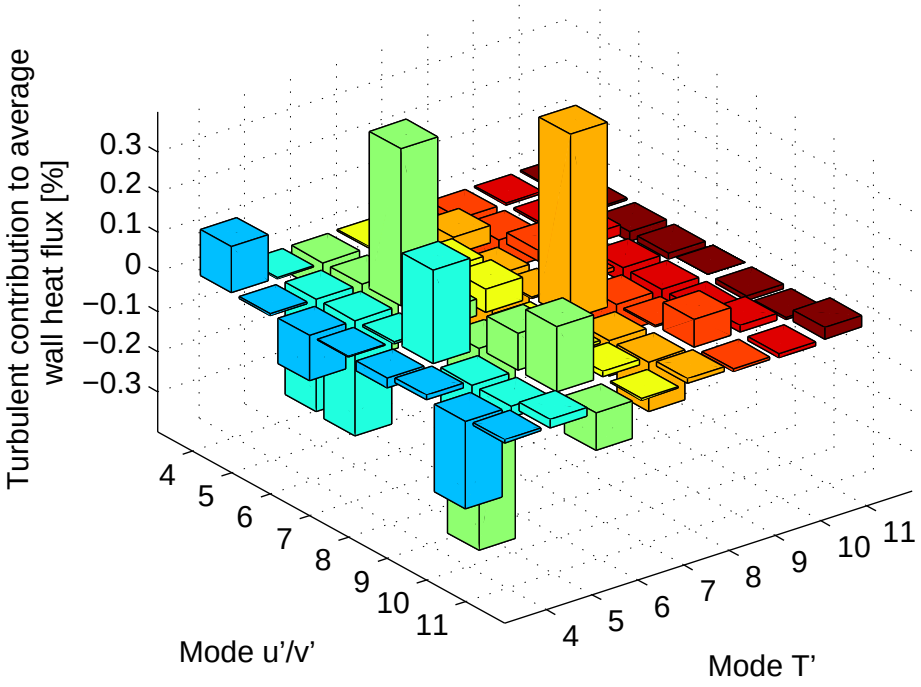

Fig. 55.: The plot shows the contribution to wall heat flux for different mode combinations. The area of interest was defined from $X/C = -0.5$ to the vane front, and from $Y/P = -0.4$ to $Y/P = 0.4$.

tinct imprint of the horseshoe vortex, though it is relatively small compared to the free stream structures. Modes six and eight also have the highest fluctuations in the pitch wise velocity component. No mode could be found within the first ten that resembles only or mainly the leading edge horseshoe vortex.

CHAPTER VII

CONCLUSIONS AND FUTURE WORK

In the first chapter, it is shown that orthogonal basis functions derived from static wall pressure measurements can be linked to flow features such as the tip clearance vortex of a transonic compressor. This is most pronounced when the compressor operates near stall and the imprint of the vortex trajectory on the dynamics of the wall pressure is the highest. When the compressor stage is driven into stall, the basis function linked to the tip clearance vortex develops a peak upstream of the blade leading edge, which might be an indication for flow spillage. This has already been identified as a stall precursor in subsonic compressors. To further investigate the mode dependence on the experimental setting, data with higher spatial resolution, which will also yield a larger number of basis functions, needs to be investigated. The blade trailing edge should be instrumented as well since the second precursor for stall in subsonic compressors has been found to be a trailing edge back flow. To control the tip clearance, circumferential grooves are applied to the compressor casing. Examining this data set will help validating the link between modes and vortex dynamics, for example.

Simulating a single row pin fin heat exchanger with unsteady Reynolds-averaged Navier-Stokes turbulence modeling and applying orthogonal decomposition, it was possible to distinguish between modes responsible for lift, drag and the stagnating boundary layer vortex. This correlation became less distinct when more dynamics were included in the simulation by resolving the large scales (LES). The deviation of integral quantities such as surface heat transfer between numerical and experimental results decreased with LES. In both simulations, the reduced order representation of the data, ranked with respect to heat transfer, shows modes that were not contributing

to turbulent heat transfer and can thus be considered wasteful.

In an attempt to optimize the pin fin heat exchanger, a wall contour is derived from the spatial eigenfunction of one mode identified as particularly important to heat transfer. Comparing the smooth with the contoured case over the same simulated time, it is shown that the energy in the modes without any enthalpy dynamics decreases. The contoured wall leads to a more uniform wake shape among the three pins included in the domain. The highest heat transfer increase due to wall contouring is seen in the wake region immediately downstream of the pin row. On the end wall, the root mean square temperature decreases in the pin fin wake but is slightly elevated in the stagnation region upstream. The pressure drop across the array is raised by roughly the same magnitude that a sole increase in Reynolds number would cause. To improve efficiency, the wall contour edges should be made less sharp. This optimization provides a parameter free, single pass design improvement. But since the orthogonal basis set is only optimal for the sample it was built from, no predictions for future (or past) flow behavior can be made. Thus the need for validating the method with longer time integration and different operating conditions arises. Since the improvements seem to be linked in part to the wake of the middle pin, the influence of the periodic boundary conditions might need to be decreased further by including more pins in the domain. Examining a multi row arrangement would be more relevant to real gas turbine design. Another interesting aspect from the industrial design point of view would be to examine whether an optimization can also be based on results of the lower order turbulence modeling.

For a direct numerical simulation of a first stage stator turbine passage, inflow with elevated length scale and free stream intensity is generated. The simulation shows that there are multiple horseshoe vortices that oscillate upstream of the blade, vanish, regenerate and can also merge. There is a punctual correlation of intense vor-

tex dynamics and peaks in the orthogonal temperature basis function. The highest endwall heat transfer is seen downstream of the stagnation point towards the blade suction side, where the horseshoe vortices are pushed together by the pitch wise pressure gradient. The mode ranking unveiled two modes of distinct importance for heat transfer among the first ten modes. As a next step, this information should be used for optimization similar to what is shown for the pin fin cooling passage. To make the numerical simulations more relevant to real gas turbines, the inflow conditions need to be better controllable and the Reynolds number needs to increase. The free stream intensity, integral length scale and boundary layer parameters need to be definable by the user a priori. For reaching engine Reynolds numbers on the order of 10^6 while maintaining computational feasibility, an accurate LES model that correctly captures heat transfer in stagnating flows is essential. Within this setting, the optimization method as described above should be tested to see whether a reduction of temperature fluctuations in certain parts of the end wall, improvement of spatial distribution or change of heat transfer magnitude can be achieved. Pulsating cooling jets using the dominant frequency of time functions, for example, could be an alternative to end wall contouring.

The link between the energy optimal orthogonal basis functions and flow structures is neither guaranteed to exist nor straightforward to establish. As the systems examined in this dissertation show, prior knowledge of the flow structures needs to exist. The orthogonal expansion presented herein locks onto flow parts with high fluctuating kinetic energy - which might or might not be the ones that are looked for. The heat transfer ranking eliminates this problem and is valid independently of how certain basis functions are interpreted.

REFERENCES

[1] US Environmental Protection Agency, "Electric power annual report 2009," http://www.eia.doe.gov/cneaf/electricity/epa/epa.pdf, accessed December 2010.

[2] Rolls Royce plc., "ESA IMPRESS integrated project," http://www.spaceflight.esa.int/impress/text/pop-up/trent.html, accessed December 2010.

[3] P. F. Fischer, J. W. Lottes, and S. G. Kerkemeier, "NEK5000 Web page," 2008, http://nek5000.mcs.anl.gov.

[4] N. Aubry, R. Guyonnet, and R. Lima, "Spatiotemporal analysis of complex signals: Theory and applications.," *Journal of Statistical Physics*, vol. 64, pp. 683–739, 1991.

[5] R. A. Handler, K. D. Housiadas, and A. N. Beris, "Karhunen-Loeve representations of turbulent channel flows using the method of snapshots," *International Journal for Numerical Methods in Fluids*, vol. 52, pp. 1339–1360, 2006.

[6] D. Werner, *Funktionalanalysis*, 6th edition, Heidelberg, Germany: Springer-Verlag, 2007.

[7] W.M. Kays, M.E. Crawford, and B. Weigand, *Convective Heat and Mass Transfer*, 4th edition, New York, NY: McGraw-Hill Book Company, Inc., 2005.

[8] E. M. Greitzer, "Some aerodynamic problems of aircraft engines: Fifty years after - the 2007 IGTI scholar lecture," *Journal of Turbomachinery*, vol. 131, CID 031101, 2007.

[9] T. R. Camp and I. J. Day, "A study of spike and modal stall phenomena in a low-speed axial compressor," *Journal of Turbomachinery*, vol. 120, pp. 393–401, 1998.

[10] H. D. Vo, C. S. Tan, and E. M. Greitzer, "Criteria for spike initiated rotating stall," *Journal of Turbomachinery*, vol. 130, CID 011023, 2008.

[11] C. Hah, J. Bergner, and H.-P. Schiffer, "Short length-scale rotating stall inception in a transonic axial compressor - Criteria and mechanism," in *Proceedings of ASME TurboExpo 2006*, Barcelona, Spain, 2006, ASME paper GT-2006-90045.

[12] C. Biela, M. W. Müller, and H.-P. Schiffer, "Unsteady pressure measurement in a single stage axial transonic compressor near the stability limit," in *Proceedings of ASME TurboExpo 2008*, Berlin, Germany, 2008, ASME paper GT-2008-50245.

[13] K. S. Ball, L. Sirovich, and L. R. Keefe, "Dynamical eigenfunction decomposition of turbulent channel flow," *Int. J. Num. Meth. Fluids*, vol. 12, pp. 585–604, 1991.

[14] A. Duggleby, K.S. Ball, and M. Schwänen, "Structure and dynamics of low Reynolds number turbulent pipe flow," *Phil. Trans. Roy. Soc. A*, vol. 367, no. 1888, pp. 473–488, 2009.

[15] P. Holmes, J. L. Lumley, and G. Berkooz, *Turbulence, Coherent Structures, Dynamical Systems, and Symmetry*, Cambridge, UK: Cambridge University Press, 1996.

[16] M. Schobeiri, *Turbomachinery Flow Physics and Dynamic Performance*, Heidelberg, Germany: Springer-Verlag, 2005.

[17] J.-C. Han, S. Dutta, and S. V. Ekkad, *Gas Turbine Heat Transfer and Cooling Technology*, New York, NY: Taylor and Francis, 2000.

[18] G. L. Kindlmann, "Semi-automatic generation of transfer functions for direct volume rendering," MS Thesis, Cornell University, Ithaca, NY, January 1999, http://www.cs.utah.edu/∼gk/MS/html/thesis.html, accessed Feb. 10th 2009.

[19] J. Armstrong and D. Winstanley, "A review of staggered array pin fin heat transfer for turbine cooling applications," *Journal of Turbomachinery*, vol. 110, pp. 94–103, 1988.

[20] M.E. Lyall, A.A. Thrift, and K. A. Thole, "Heat transfer from low aspect ratio pin fins," in *Proceedings of ASME TurboExpo 2007*, Montreal, Canada, 2007, ASME paper GT-2007-27431.

[21] F.E. Ames and L.A. Dvorak, "Turbulent transport in pin fin arrays - experimental data and predictions," in *Proceedings of ASME TurboExpo 2005*, Reno, NV, 2005, ASME paper GT-2005-68180.

[22] M.E. Young and A. Ooi, "Turbulence models and boundary conditions for bluff body flow," in *Proceedings of the Fifteenth Australasian Fluid Mechanics Conference*, Sydney, Australia, 2004.

[23] D. Holloway, D. Walters, and J. Leylek, "Prediction of unsteady, separated boundary layer over a blunt body for laminar, turbulent, and transitional flow," *International Journal for Numerical Methods in Fluids*, vol. 45, pp. 1291–1315, 2004.

[24] K. Harrison and D. Bogard, "Comparison of RANS turbulence models for prediction of film cooling performance," in *Proceedings of ASME TurboExpo 2008*, Berlin, Germany, 2008, ASME paper GT-2008-51423.

[25] P.A. Durbin, "On the k-3 stagnation point anomaly," *International Journal of Heat and Fluid Flow*, vol. 17, no. 1, pp. 89–90, 1996.

[26] W.M. Kays and M.E. Crawford, *Convective Heat and Mass Transfer*, New York, NY: McGraw-Hill Book Company, Inc., 1980.

[27] I. Celik, M. Klein, and J. Janicka, "Assessment measures for engineering LES applications," *Journal of Fluids Engineering*, vol. 131, CID 031102, 2009.

[28] V.C. Patel and M.R. Head, "Some observations on skin friction and velocity profiles in fully developed pipe and channel flows," *Journal of Fluid Mechanics*, vol. 38, pp. 181–201, 1969.

[29] F.P. Incropera and D.P. DeWitt, *Fundamentals of Heat and Mass Transfer*, New York, NY: John Wiley and Sons, Inc., 2002.

[30] G. Su, H.C. Chen, and J.C. Han, "Computation of flow and heat transfer in rotating rectangular channels (AR=4:1) with pin-fins by a Reynolds stress turbulence model," in *Proceedings of ASME TurboExpo 2005*, Reno, NV, 2005, ASME paper GT-2005-68390.

[31] S. Stolz, "High-pass filtered eddy-viscosity models for large eddy simulations of compressible wall-bounded flows," *Journal of Fluids Engineering*, vol. 127, no. 4, pp. 666–673, 2005.

[32] P. F. Fischer and J. Mullen, "Filter-based stabilization of spectral element methods," *C.R.Acad. Sci. Ser. I-Anal Numer.*, vol. 163, pp. 193–204, 2001.

[33] M. Bergmann and L. Cordier, "Optimal control of the cylinder wake in the laminar regime by trust-region methods and POD reduced-order models," *Journal of Computational Physics*, vol. 16, pp. 7813–7840, 2008.

[34] D. Thvenin and G. Janiga, Eds., *Optimization and Computational Fluid Dynamics*, Heidelberg, Germany: Springer-Verlag, 2008.

[35] S. P. Lynch, S. Narayan, and K. A. Thole, "Heat transfer for a turbine blade with nonaxisymmetric endwall contouring," *Journal of Turbomachinery*, vol. 133, CID 011019, 2011.

[36] A. K. Saha and S. Acharya, "Computations of turbulent flow and heat transfer through a three-dimensional nonaxisymmetric blade passage," *Journal of Turbomachinery*, vol. 130, CID 031008, 2008.

[37] S. Reising and H.-P. Schiffer, "Non-axisymmetric end wall profiling in transonic compressorspart II: Design study of a transonic compressor rotor using non-axisymmetric end walls-optimization strategies and performance," in *Proceedings of ASME TurboExpo 2009*, Orlando, FL, 2009, ASME paper GT-2009-59134.

[38] O. Walsh, "Eddy solutions of the Navier-Stokes equations," in *The Navier-Stokes Equations II - Theory and Numerical Methods*, vol. 1530 of *Lecture Notes in Mathematics*, pp. 306–309, Heidelberg, Germany: Springer-Verlag, 1992.

[39] R. E. Gaugler and L. M. Russell, "Comparison of visualized turbine endwall secondary flows and measured heat transfer patters," *ASME J. Eng. Gas Turbine Power*, vol. 106, pp. 168–172, 1984.

[40] M. Kang, A. Kohli, and K. A. Thole, "Heat transfer and flowfield measurements in the leading edge region of a stator vane endwall," *Journal of Turbomachinery*, vol. 121, pp. 558–568, 1999.

[41] W. J. Devenport and R. L. Simpson, "Time-dependent and time-averaged turbulence structure near the nose of a wing-body junction," *J. Fluid Mech.*, vol. 210, pp. 23–55, 1990.

[42] R. Radomsky and K. A. Thole, "High freestream turbulence effects in the endwall leading edge region," *Journal of Turbomachinery*, vol. 122, pp. 699–708, 2000.

[43] D. G. Gregory-Smith and J. G. E. Cleak, "Secondary flow measurements in a turbine cascade with high inlet turbulence," *Journal of Turbomachinery*, vol. 114, pp. 173–183, 1992.

[44] M. C. Spencer, T. V. Jones, and G. D. Lock, "Endwall heat transfer measurements in an annular cascade of nozzle guide vanes at engine representative Reynolds and Mach numbers," *International Journal of Heat and Fluid Flow*, vol. 17, pp. 139–147, 1996.

[45] L. S. Langston, "Secondary flows in axial turbines - a review," *Ann. New York Acad. Sci.*, vol. 934, pp. 11–26, 2001.

[46] K. A. Thole, Pennsylvania State University, State College, PA, 2008, personal communication.

[47] A. Sadiki, M. Klein, and J. Janicka, "A digital filter based generation of inflow data for spatially developing direct numerical or large eddy simulations," *Journal of Computational Physics*, vol. 86, pp. 652–665, 2003.

[48] R. G. Jacobs and P. A. Durbin, "Simulations of bypass transition," *Journal of Fluid Mechanics*, vol. 428, pp. 185–212, 2001.

[49] J. W. Lottes and P. F. Fischer, "Hybrid multigrid/Schwarz algorithms for the spectral element method," *J. Sci. Comp.*, vol. 24, no. 1, pp. 45–78, 2004.

[50] D. G. Knost, K. A. Thole, and A. Duggleby, "Evaluating a slot design for the combustor-turbine interface," in *Proceedings of ASME TurboExpo 2009*, Orlando, FL, 2009, ASME paper GT-2009-60168.

APPENDIX A

SAMPLE CALCULATION FOR INTRODUCING ENTHALPY THICKNESS INTO THE ENERGY BALANCE

First, Eqn. (2.22) is devided by a free stream variable that is not a function of y, for example the free stream velocity u_∞.

$$\frac{\dot{q}_s''}{u_\infty} = \frac{1}{u_\infty}\frac{\partial}{\partial x}\int_0^\infty \rho u h_{ref} dy + \frac{1}{u_\infty}\frac{\partial}{\partial z}\int_0^\infty \rho w h_{ref} dy$$

The right hand side can be rewritten using the following derivative:

$$\begin{aligned}
\frac{\partial}{\partial x}\left(\frac{1}{u_\infty}\int_0^\infty \rho u h_{ref} dy\right) + \frac{\partial}{\partial z}\left(\frac{1}{u_\infty}\int_0^\infty \rho w h_{ref} dy\right) = \\
&= \int_0^\infty \rho u h_{ref} dy \frac{\partial}{\partial x}\left(\frac{1}{u_\infty}\right) + \frac{1}{u_\infty}\frac{\partial}{\partial x}\left(\int_0^\infty \rho u h_{ref} dy\right) \\
&+ \int_0^\infty \rho w h_{ref} dy \frac{\partial}{\partial z}\left(\frac{1}{u_\infty}\right) + \frac{1}{u_\infty}\frac{\partial}{\partial z}\left(\int_0^\infty \rho w h_{ref} dy\right) \\
&= \frac{\int_0^\infty \rho u h_{ref} dy}{u_\infty}\left(\frac{1}{u_\infty}\right)\frac{-\partial u_\infty}{\partial x} + \frac{1}{u_\infty}\frac{\partial}{\partial x}\left(\int_0^\infty \rho u h_{ref} dy\right) \\
&+ \frac{\int_0^\infty \rho w h_{ref} dy}{u_\infty}\left(\frac{1}{u_\infty}\right)\frac{-\partial u_\infty}{\partial z} + \frac{1}{u_\infty}\frac{\partial}{\partial z}\left(\int_0^\infty \rho w h_{ref} dy\right)
\end{aligned}$$

Rearranging and inserting yields:

$$\begin{aligned}
\frac{\dot{q}_s''}{u_\infty} = &\int_0^\infty \frac{\rho u h_{ref}}{u_\infty} dy \left(\frac{1}{u_\infty}\right)\frac{\partial u_\infty}{\partial x} + \int_0^\infty \frac{\rho w h_{ref}}{u_\infty} dy \left(\frac{1}{u_\infty}\right)\frac{\partial u_\infty}{\partial z} \\
&+ \frac{\partial}{\partial x}\left(\int_0^\infty \frac{\rho u h_{ref}}{u_\infty} dy\right) + \frac{\partial}{\partial z}\left(\int_0^\infty \frac{\rho w h_{ref}}{u_\infty} dy\right).
\end{aligned}$$

Repeating this with $c_p(T_s - T_\infty)$ and deviding by ρ, which is assumed to be constant, will result in Eqn. (2.25).

APPENDIX B

REYNOLDS DECOMPOSITION AND AVERAGING OF ENTHALPY BALANCE

Reynolds decomposition and averaging is applied on Eqn. (2.25).

$$\frac{\dot{q}''_s}{\rho u_\infty c_p(T_s - T_\infty)} =$$
$$= \frac{\partial(\int_0^\infty \frac{\overline{u}+u'}{u_\infty}\frac{\overline{T}+T'-T_\infty}{T_s-T_\infty}dy)}{\partial x} + \frac{\partial(\int_0^\infty \frac{\overline{w}+w'}{u_\infty}\frac{\overline{T}+T'-T_\infty}{T_s-T_\infty}dy)}{\partial z}$$
$$+ \int_0^\infty \frac{\overline{u}+u'}{u_\infty}\frac{\overline{T}+T'-T_\infty}{T_s-T_\infty}dy\left(\frac{1}{u_\infty}\frac{\partial u_\infty}{\partial x} + \frac{1}{T_s-T_\infty}\frac{\partial(T_s-T_\infty)}{\partial x}\right)$$
$$+ \int_0^\infty \frac{\overline{w}+w'}{u_\infty}\frac{\overline{T}+T'-T_\infty}{T_s-T_\infty}dy\left(\frac{1}{u_\infty}\frac{\partial u_\infty}{\partial z} + \frac{1}{T_s-T_\infty}\frac{\partial(T_s-T_\infty)}{\partial z}\right)$$

$$\frac{\dot{q}''_s}{\rho u_\infty c_p(T_s - T_\infty)} =$$
$$= \frac{\partial(\int_0^\infty \frac{\overline{\overline{u}(\overline{T}-T_\infty)}+\overline{\overline{u}T'}+\overline{u'(\overline{T}-T_\infty)}+\overline{u'T'}}{u_\infty(\overline{T}_s-T_\infty)}dy)}{\partial x} + \frac{\partial(\int_0^\infty \frac{\overline{\overline{w}(\overline{T}-T_\infty)}+\overline{\overline{w}T'}+\overline{w'(\overline{T}-T_\infty)}+\overline{w'T'}}{u_\infty(T_s-T_\infty)}dy)}{\partial z}$$
$$+ \int_0^\infty \frac{\overline{\overline{u}(\overline{T}-T_\infty)}+\overline{\overline{u}T'}+\overline{u'(\overline{T}-T_\infty)}+\overline{u'T'}}{u_\infty(T_s-T_\infty)}dy\left(\frac{1}{u_\infty}\frac{\partial u_\infty}{\partial x} + \frac{1}{T_s-T_\infty}\frac{\partial(T_s-T_\infty)}{\partial x}\right)$$
$$+ \int_0^\infty \frac{\overline{\overline{w}(\overline{T}-T_\infty)}+\overline{\overline{w}T'}+\overline{w'(\overline{T}-T_\infty)}+\overline{w'T'}}{u_\infty(T_s-T_\infty)}dy\left(\frac{1}{u_\infty}\frac{\partial u_\infty}{\partial z} + \frac{1}{T_s-T_\infty}\frac{\partial(T_s-T_\infty)}{\partial z}\right)$$

$$= \frac{\partial(\int_0^\infty \frac{\overline{u}(\overline{T}-T_\infty)}{u_\infty(T_s-T_\infty)}dy + \int_0^\infty \frac{\overline{u'T'}}{u_\infty(T_s-T_\infty)}dy)}{\partial x} + \frac{\partial(\int_0^\infty \frac{\overline{w}(\overline{T}-T_\infty)}{u_\infty(T_s-T_\infty)}dy + \int_0^\infty \frac{\overline{w'T'}}{u_\infty(T_s-T_\infty)}dy)}{\partial z}$$
$$+ \left(\int_0^\infty \frac{\overline{u}(\overline{T}-T_\infty)}{u_\infty(T_s-T_\infty)}dy + \int_0^\infty \frac{\overline{u'T'}}{u_\infty(T_s-T_\infty)}dy\right)\left(\frac{1}{u_\infty}\frac{\partial u_\infty}{\partial x} + \frac{1}{T_s-T_\infty}\frac{\partial(T_s-T_\infty)}{\partial x}\right)$$
$$+ \left(\int_0^\infty \frac{\overline{w}(\overline{T}-T_\infty)}{u_\infty(T_s-T_\infty)}dy + \int_0^\infty \frac{\overline{w'T'}}{u_\infty(T_s-T_\infty)}dy\right)\left(\frac{1}{u_\infty}\frac{\partial u_\infty}{\partial z} + \frac{1}{T_s-T_\infty}\frac{\partial(T_s-T_\infty)}{\partial z}\right)$$

APPENDIX C

SCALAR SPATIAL BASIS FUNCTIONS FROM PINFIN LES

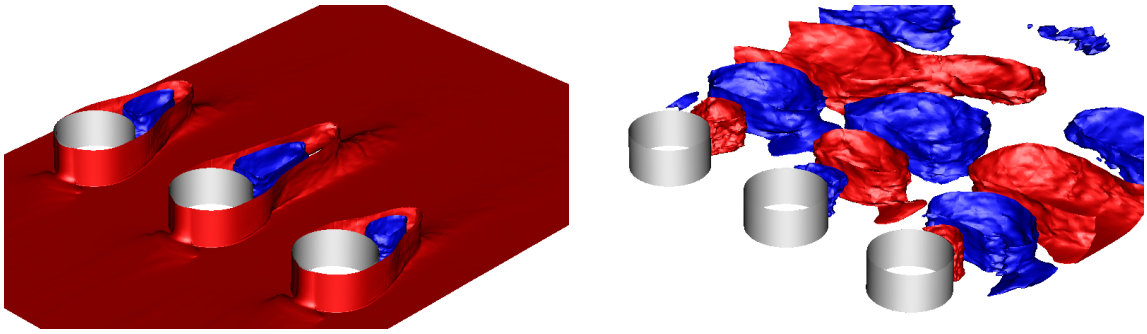

Isosurfaces at 4 (blue) and -4 (red) of scalar spatial basis function of mode 0 (left) and 1 (right).

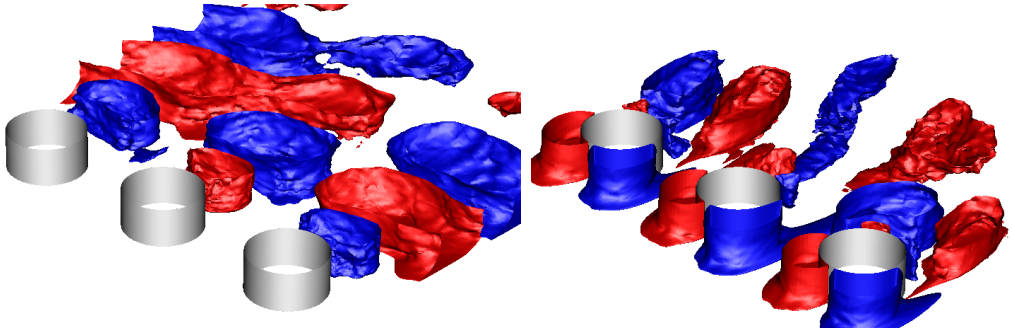

Isosurfaces at 4 (blue) and -4 (red) of scalar spatial basis function of mode 2 (left) and 3 (right).

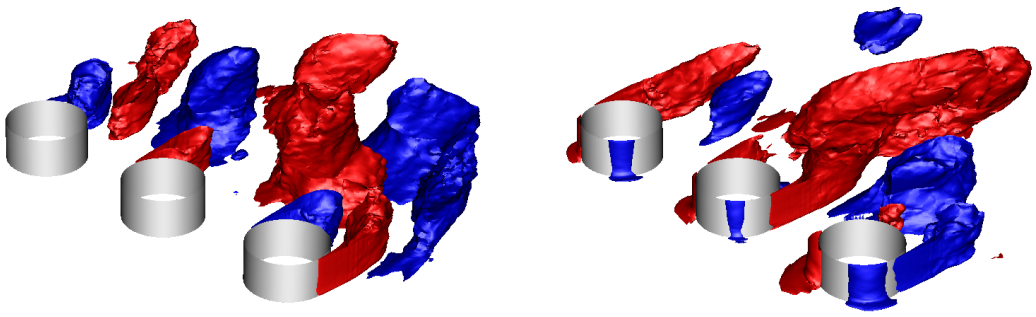

Isosurfaces at 4 (blue) and -4 (red) of scalar spatial basis function of mode 4 (left) and 5 (right).

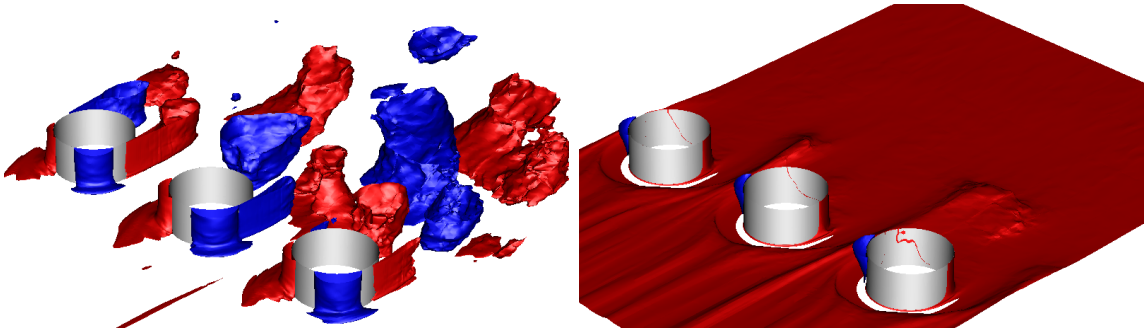

Isosurfaces at 4 (blue) and -4 (red) of scalar spatial basis function of mode 6 (left) and 7 (right).

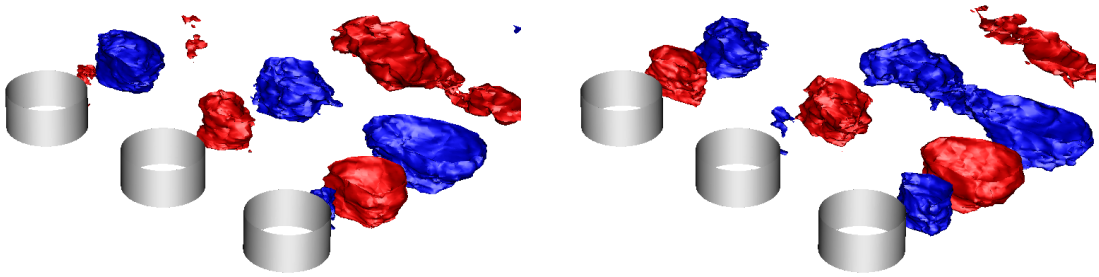

Isosurfaces at 4 (blue) and -4 (red) of scalar spatial basis function of mode 8 (left) and 9 (right).

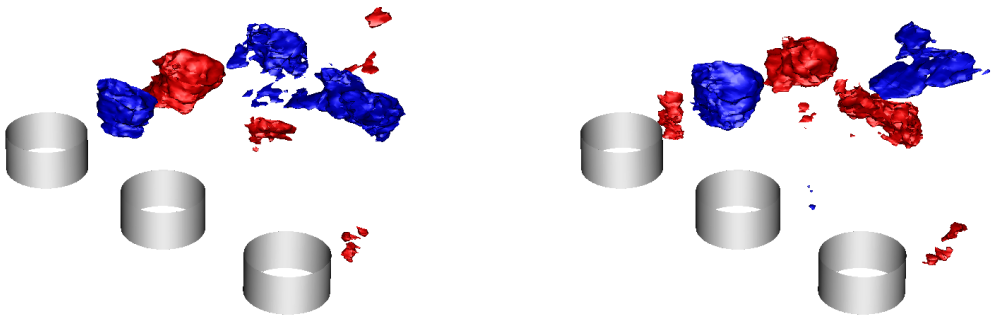

Isosurfaces at 4 (blue) and -4 (red) of scalar spatial basis function of mode 10 (left) and 11 (right).

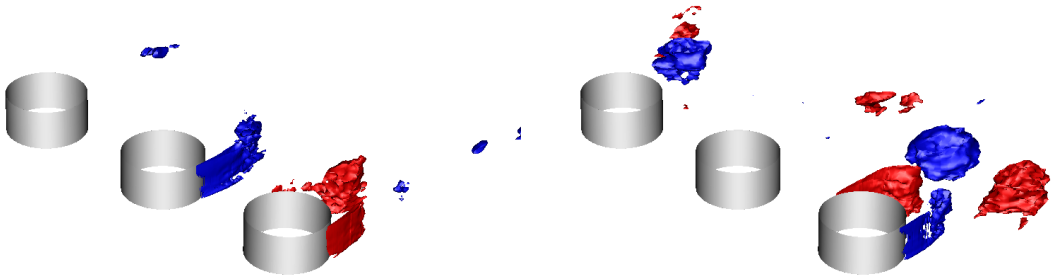

Isosurfaces at 4 (blue) and -4 (red) of scalar spatial basis function of mode 12 (left) and 13 (right).

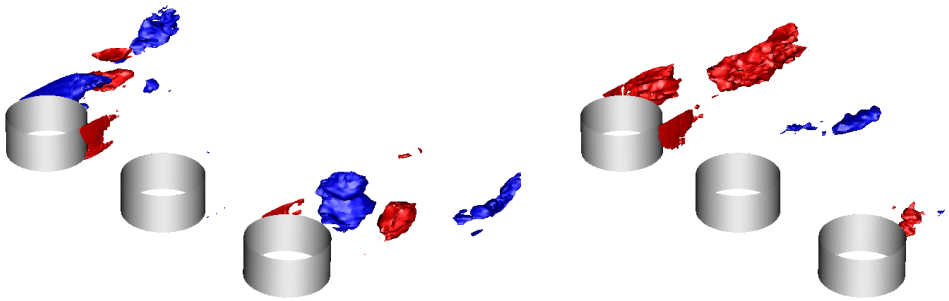

Isosurfaces at 4 (blue) and -4 (red) of scalar spatial basis function of mode 14 (left) and 15 (right).

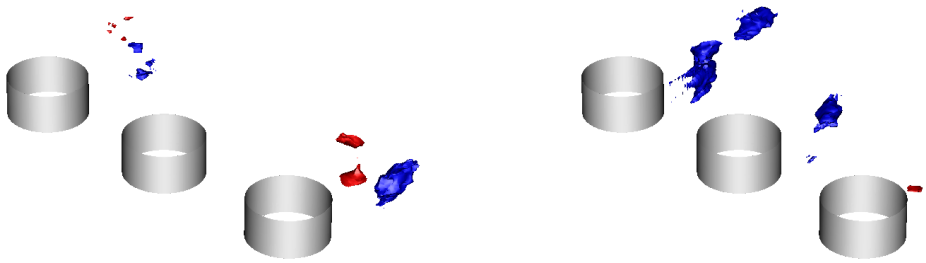

Isosurfaces at 4 (blue) and -4 (red) of scalar spatial basis function of mode 16 (left) and 17 (right).

Isosurfaces at 4 (blue) and -4 (red) of scalar spatial basis function of mode 18 (left) and 19 (right).

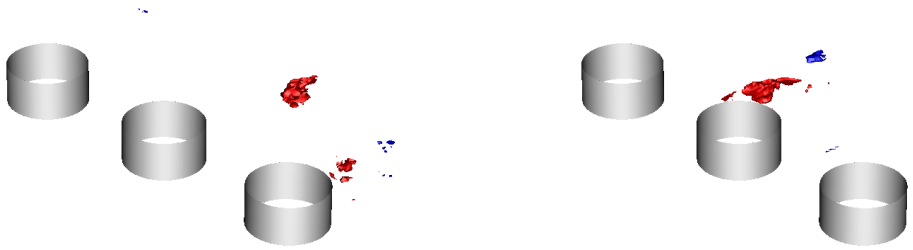

Isosurfaces at 4 (blue) and -4 (red) of scalar spatial basis function of mode 20 (left) and 21 (right).

Isosurfaces at 4 (blue) and -4 (red) of scalar spatial basis function of mode 22 (left) and 23 (right).

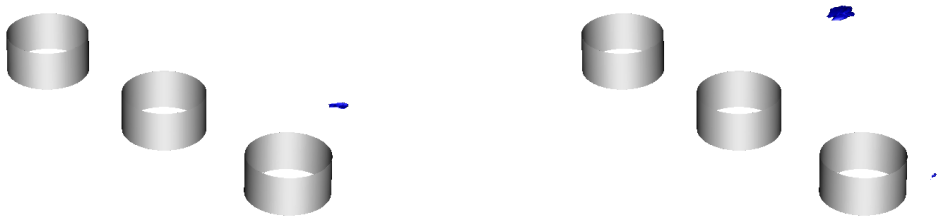

Isosurfaces at 4 (blue) and -4 (red) of scalar spatial basis function of mode 24 (left) and 25 (right).

Isosurfaces at 4 (blue) and -4 (red) of scalar spatial basis function of mode 26 (left) and 27 (right).

Isosurfaces at 4 (blue) and -4 (red) of scalar spatial basis function of mode 28 (left) and 29 (right).

Isosurfaces at 4 (blue) and -4 (red) of scalar spatial basis function of mode 30 (left) and 31 (right).

Isosurfaces at 4 (blue) and -4 (red) of scalar spatial basis function of mode 32 (left) and 33 (right).

Isosurfaces at 4 (blue) and -4 (red) of scalar spatial basis function of mode 34 (left) and 35 (right).

APPENDIX D

SCALAR SPATIAL BASIS FUNCTIONS FROM TURBINE PASSAGE DNS

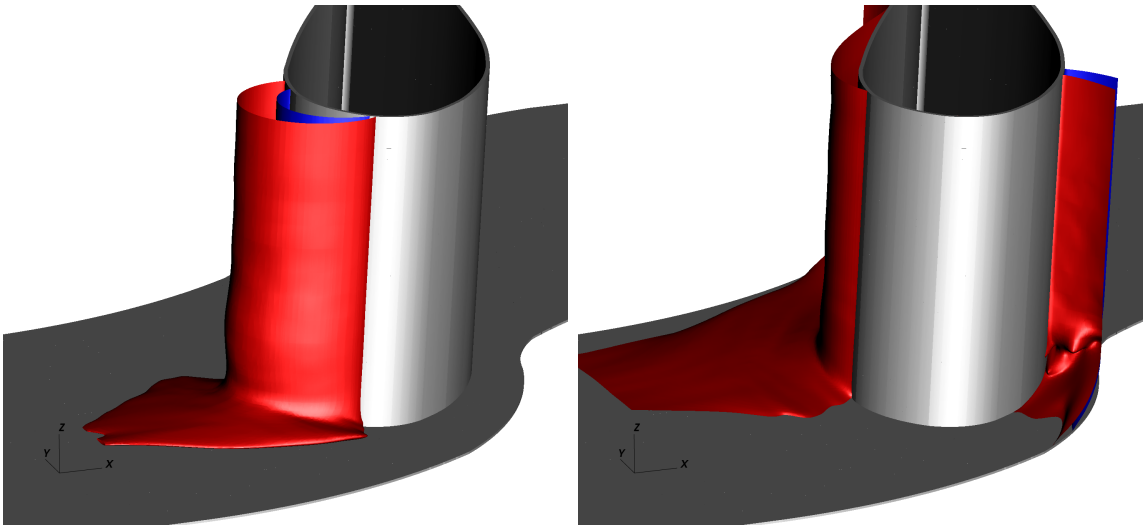

Isosurfaces at -2 (blue) and 2 (red) of scalar spatial basis function of mode 0 (left) and 1 (right).

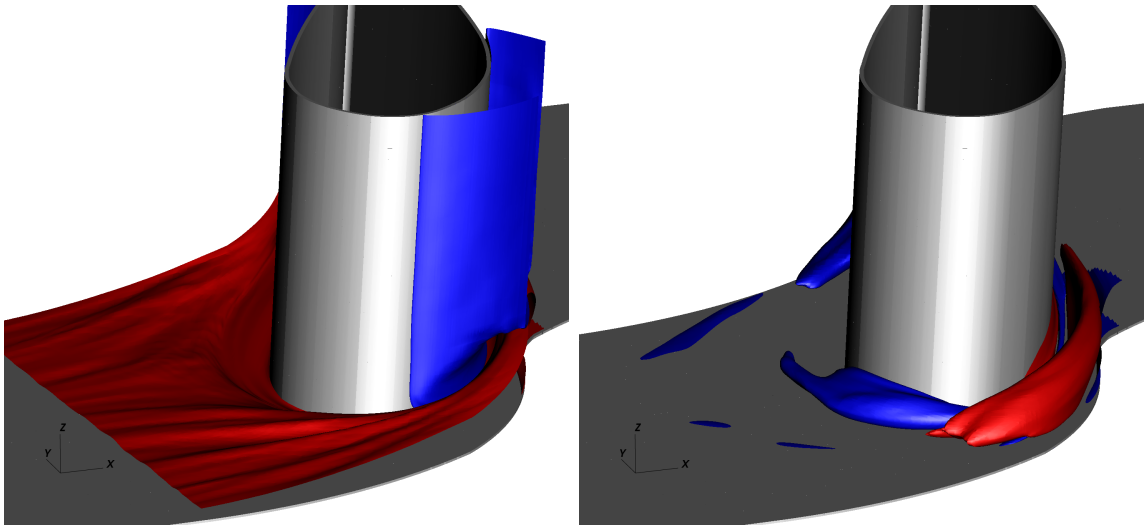

Isosurfaces at -2 (blue) and 2 (red) of scalar spatial basis function of mode 2 (left) and 3 (right).

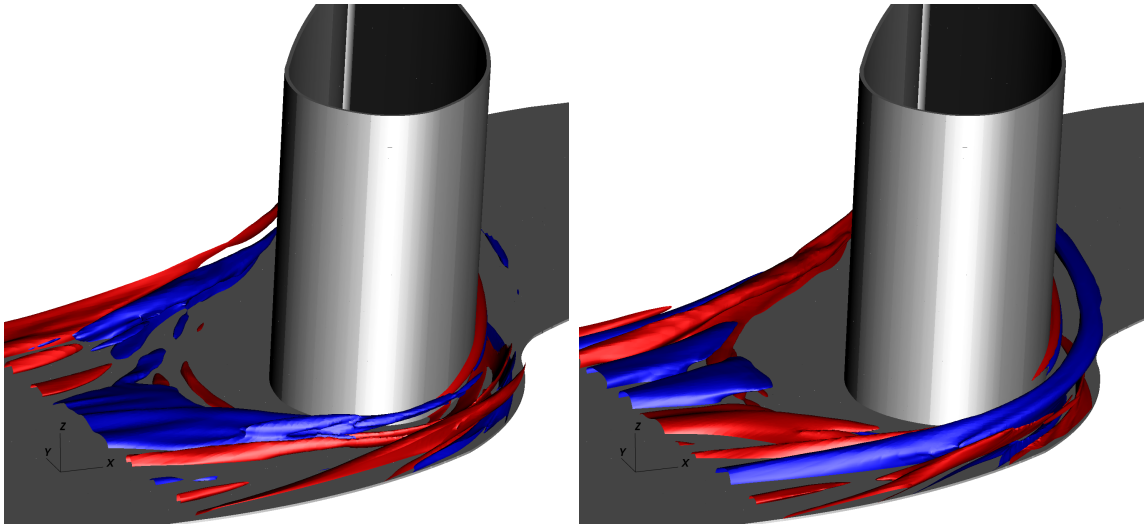

Isosurfaces at -2 (blue) and 2 (red) of scalar spatial basis function of mode 4 (left) and 5 (right).

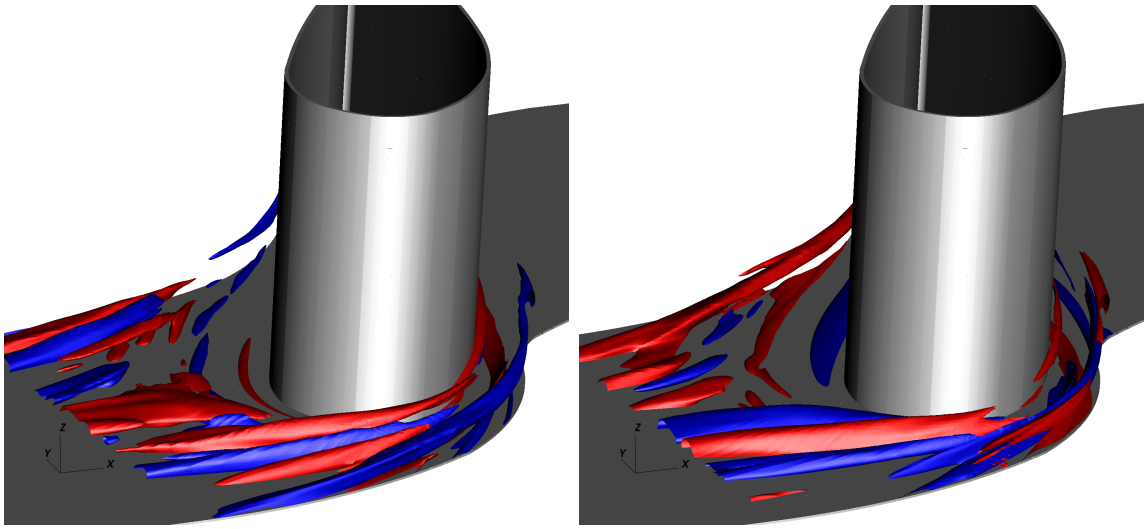

Isosurfaces at -2 (blue) and 2 (red) of scalar spatial basis function of mode 6 (left) and 7 (right).

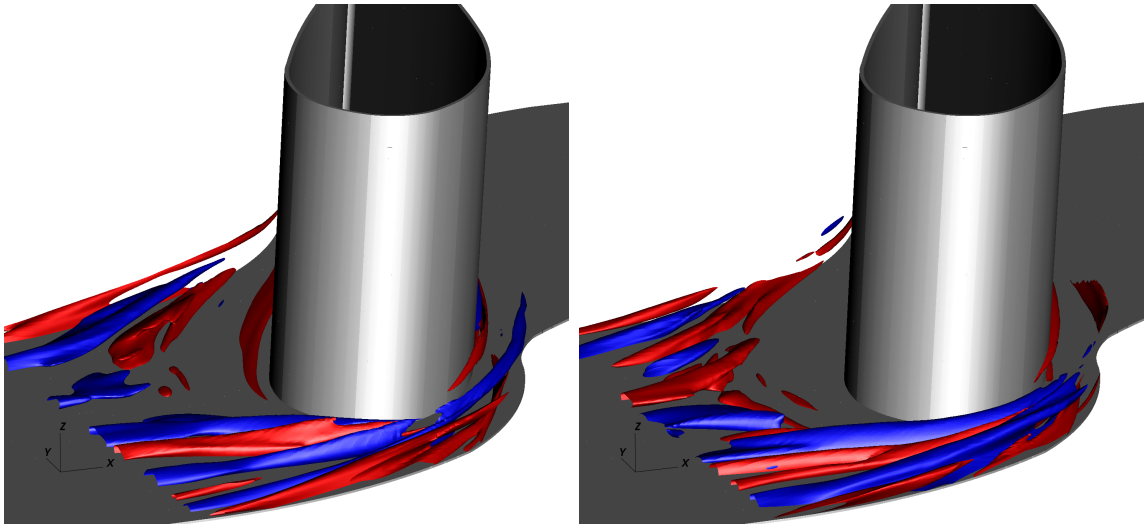

Isosurfaces at -2 (blue) and 2 (red) of scalar spatial basis function of mode 8 (left) and 9 (right).

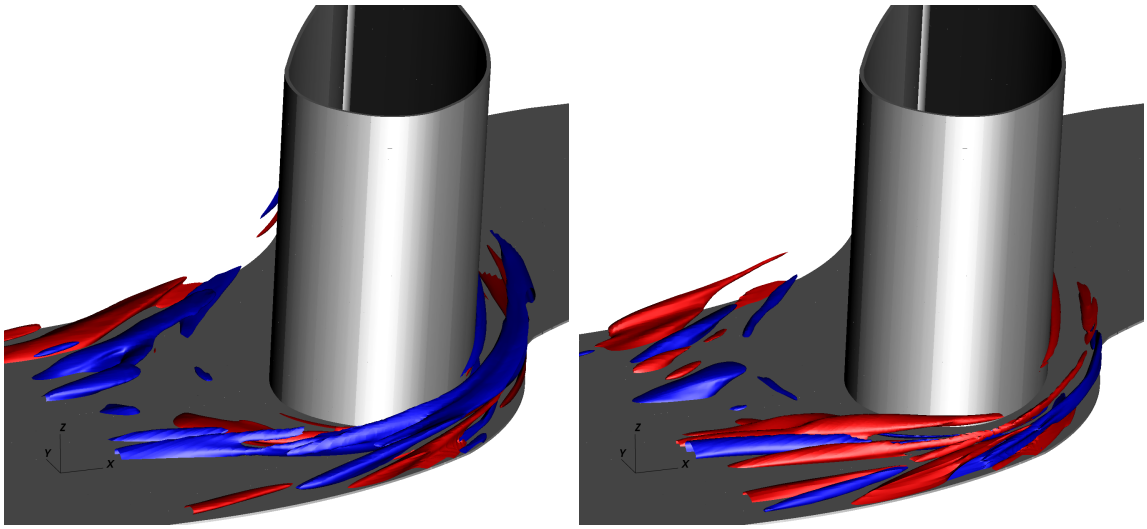

Isosurfaces at -2 (blue) and 2 (red) of scalar spatial basis function of mode 10 (left) and 11 (right).

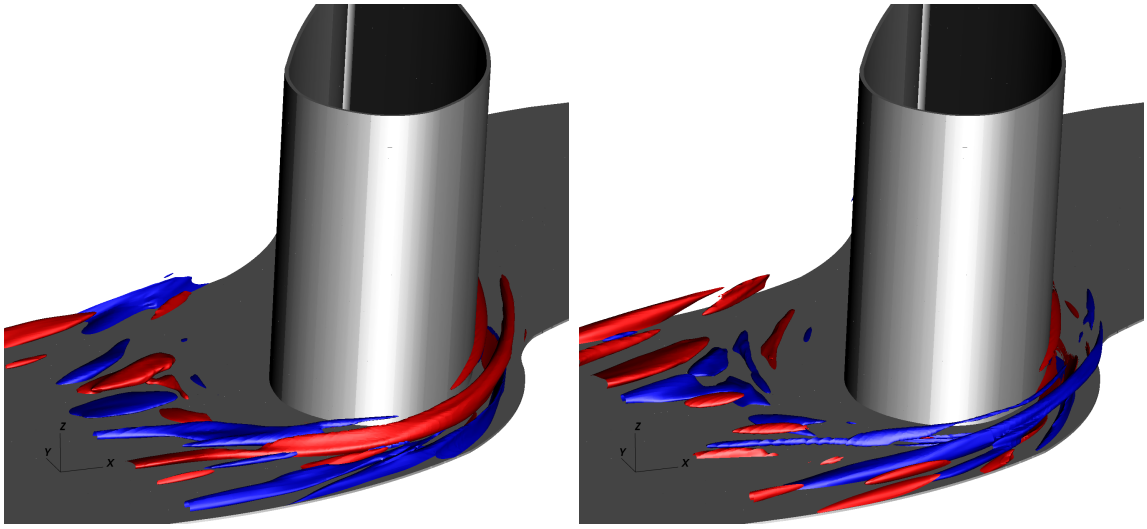

Isosurfaces at -2 (blue) and 2 (red) of scalar spatial basis function of mode 12 (left) and 13 (right).

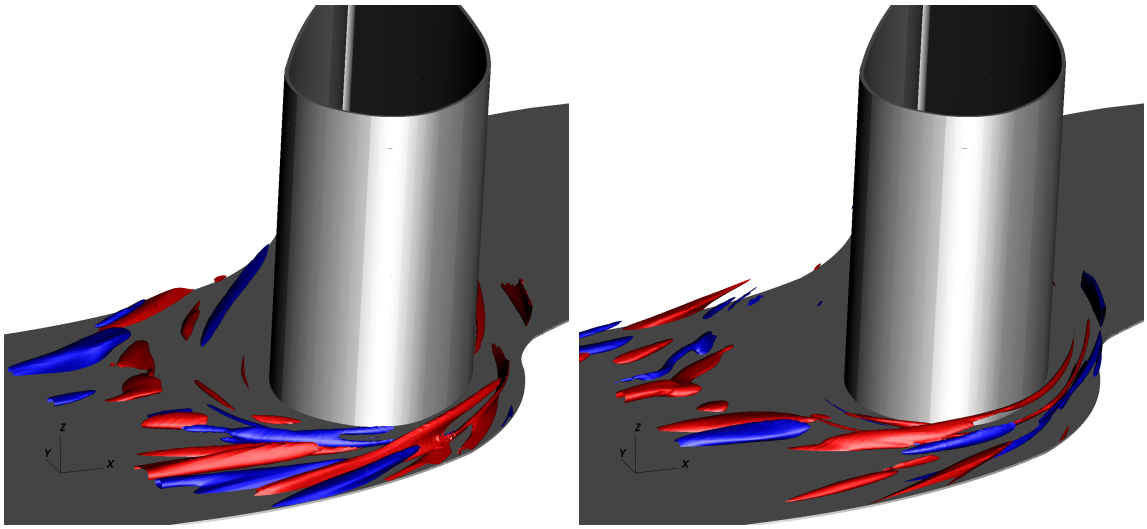

Isosurfaces at -2 (blue) and 2 (red) of scalar spatial basis function of mode 14 (left) and 15 (right).

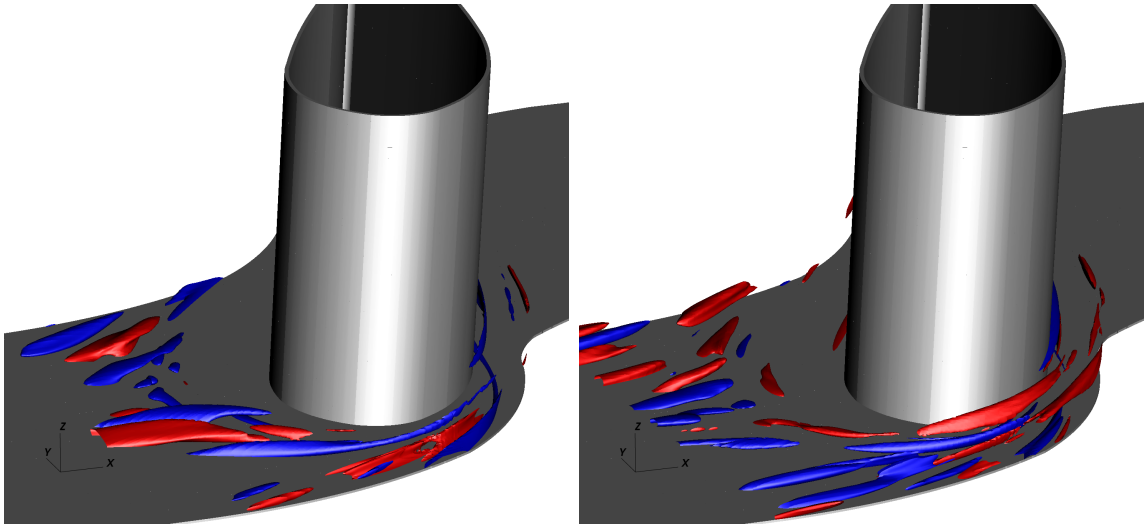

Isosurfaces at -2 (blue) and 2 (red) of scalar spatial basis function of mode 16 (left) and 17 (right).

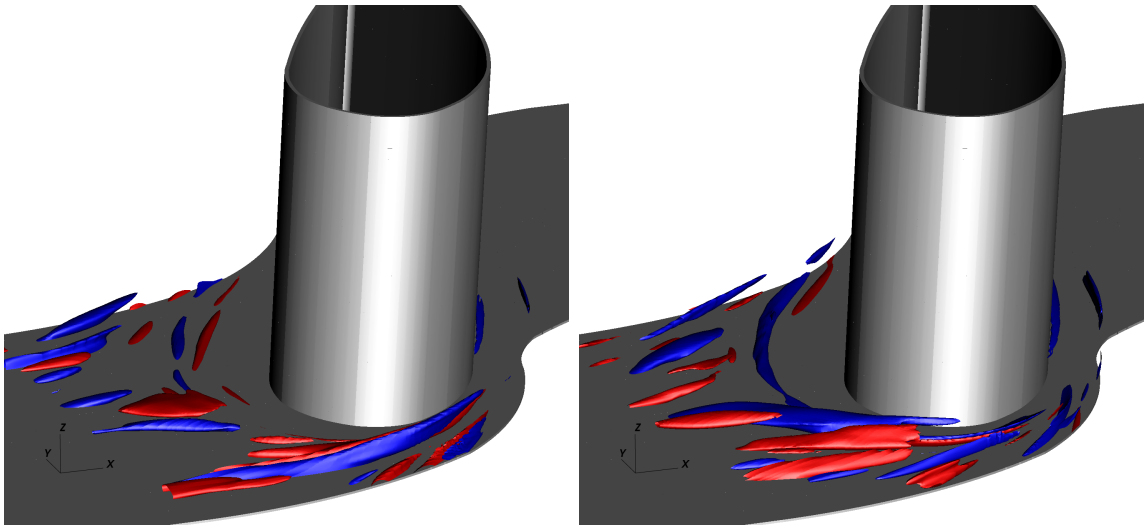

Isosurfaces at -2 (blue) and 2 (red) of scalar spatial basis function of mode 18 (left) and 19 (right).

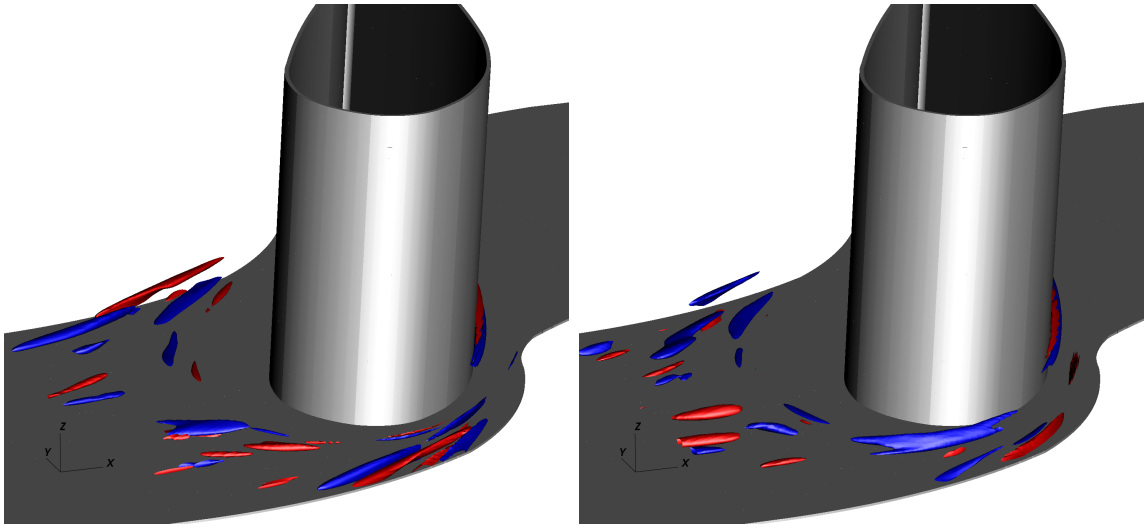

Isosurfaces at -2 (blue) and 2 (red) of scalar spatial basis function of mode 20 (left) and 21 (right).

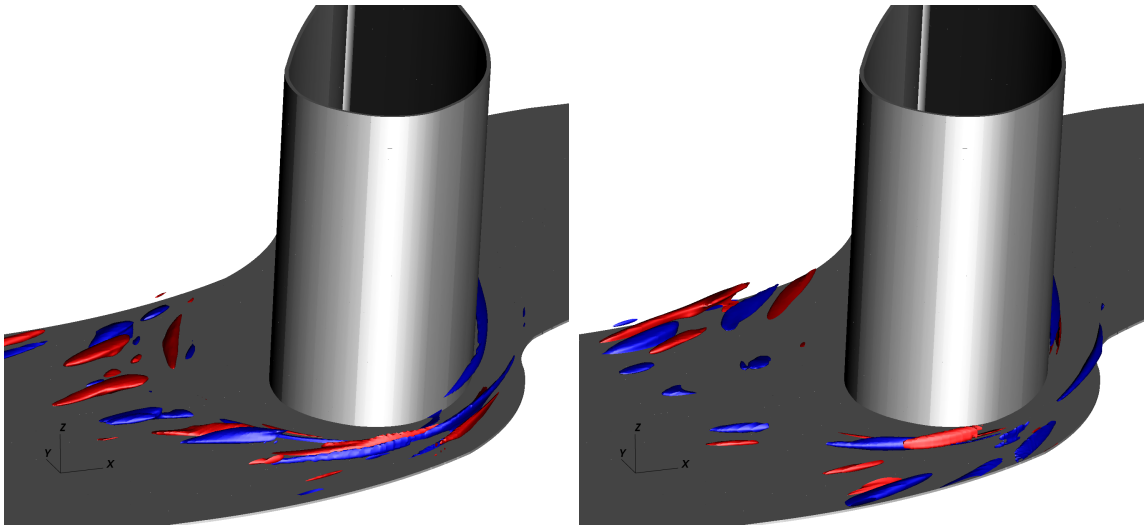

Isosurfaces at -2 (blue) and 2 (red) of scalar spatial basis function of mode 22 (left) and 23 (right).

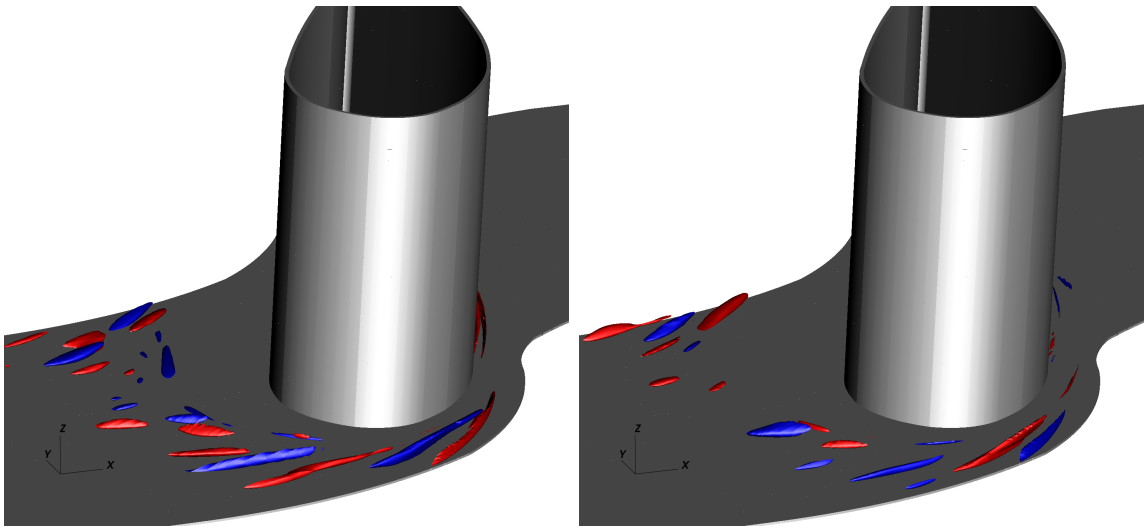

Isosurfaces at -2 (blue) and 2 (red) of scalar spatial basis function of mode 24 (left) and 25 (right).

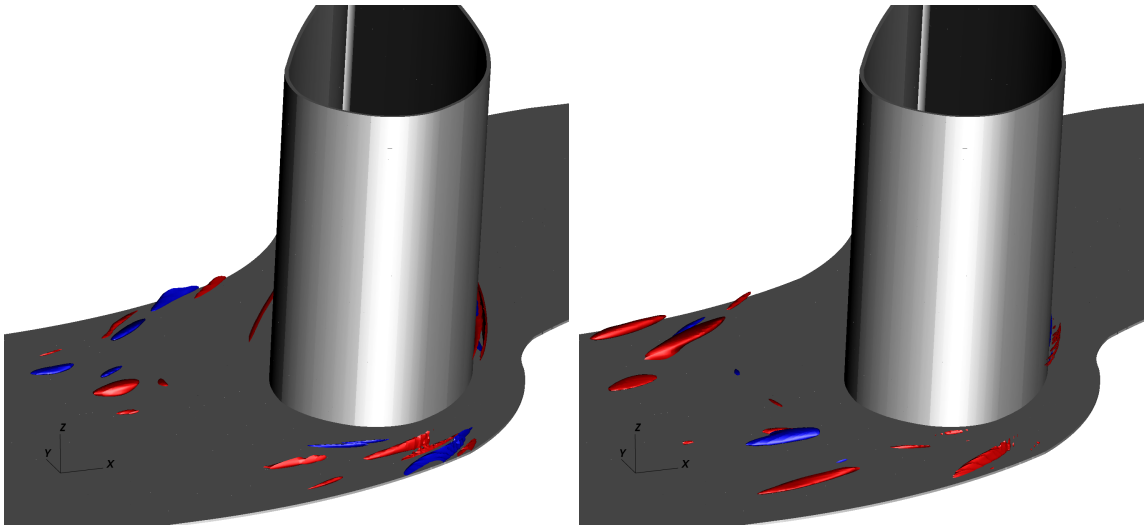

Isosurfaces at -2 (blue) and 2 (red) of scalar spatial basis function of mode 26 (left) and 27 (right).

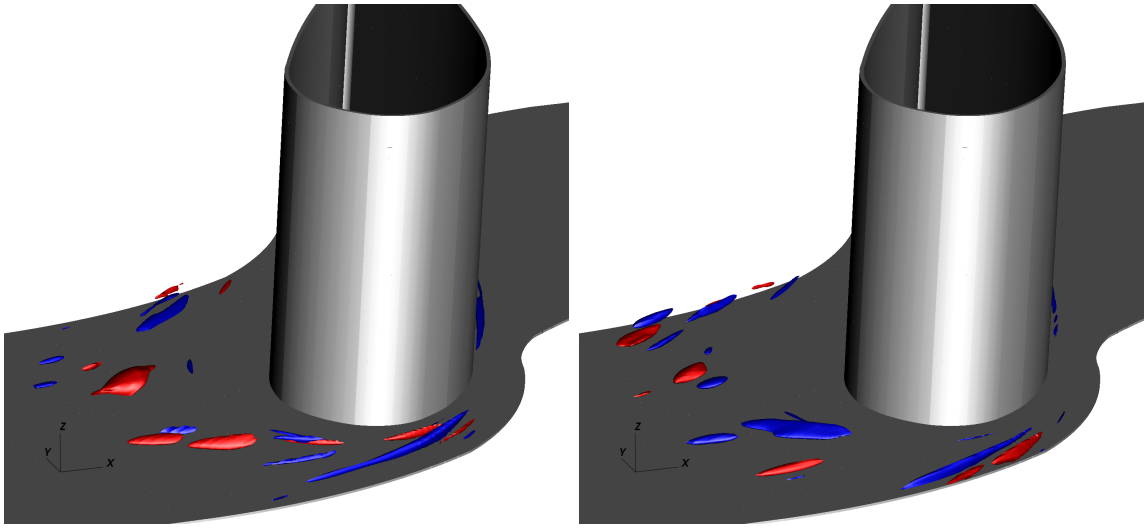

Isosurfaces at -2 (blue) and 2 (red) of scalar spatial basis function of mode 28 (left) and 29 (right).

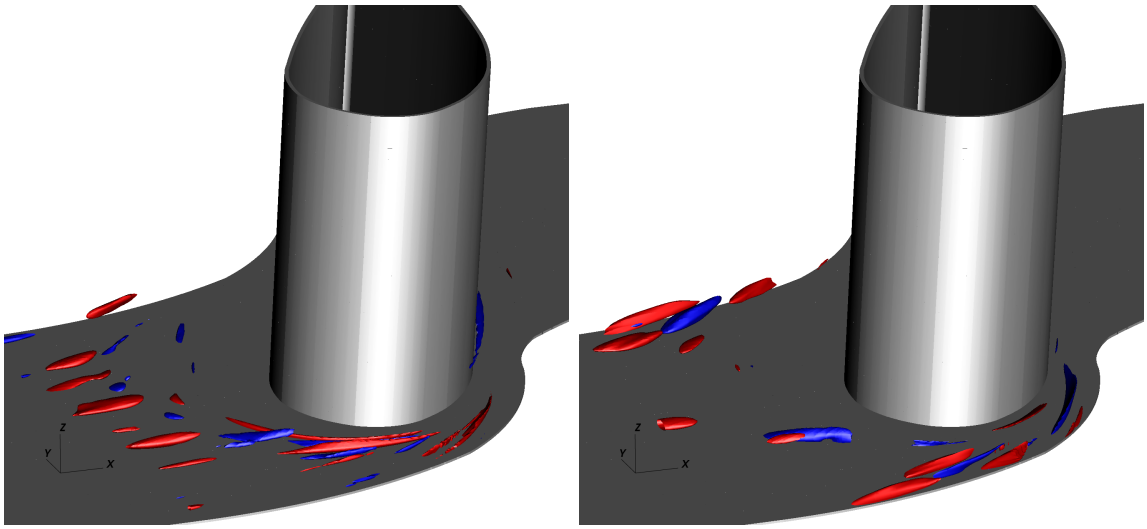

Isosurfaces at -2 (blue) and 2 (red) of scalar spatial basis function of mode 30 (left) and 31 (right).

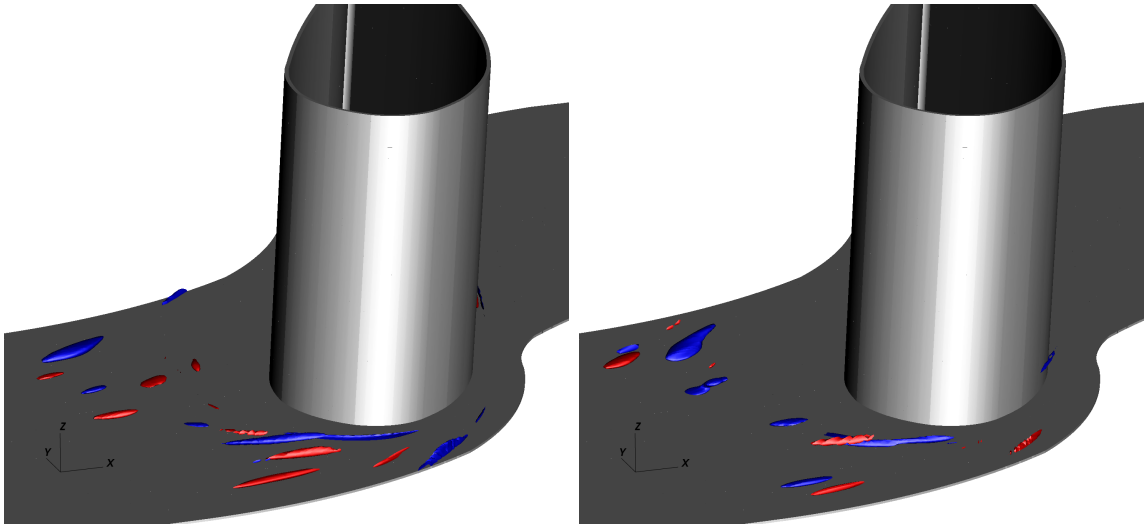

Isosurfaces at -2 (blue) and 2 (red) of scalar spatial basis function of mode 32 (left) and 33 (right).

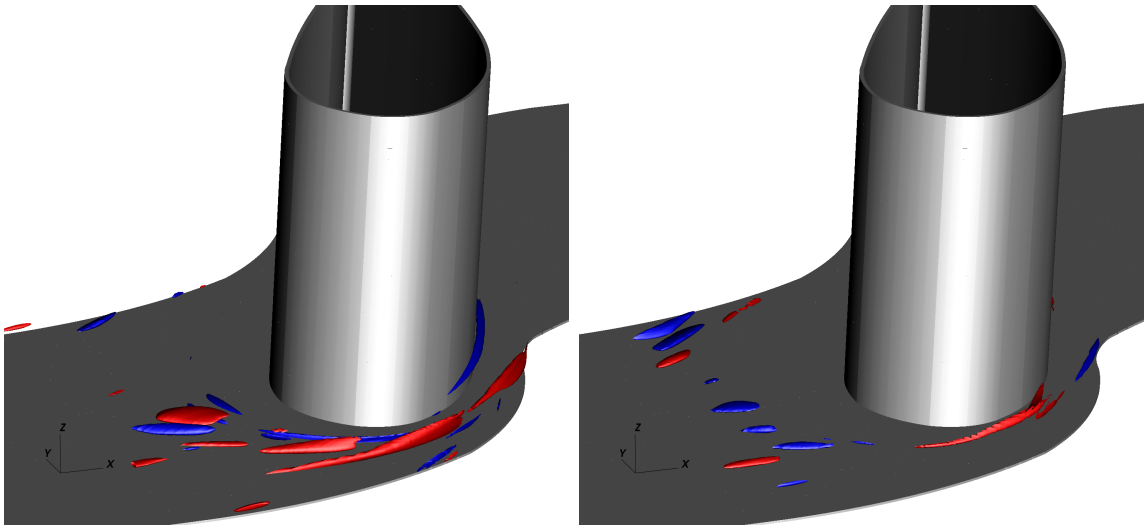

Isosurfaces at -2 (blue) and 2 (red) of scalar spatial basis function of mode 34 (left) and 35 (right).

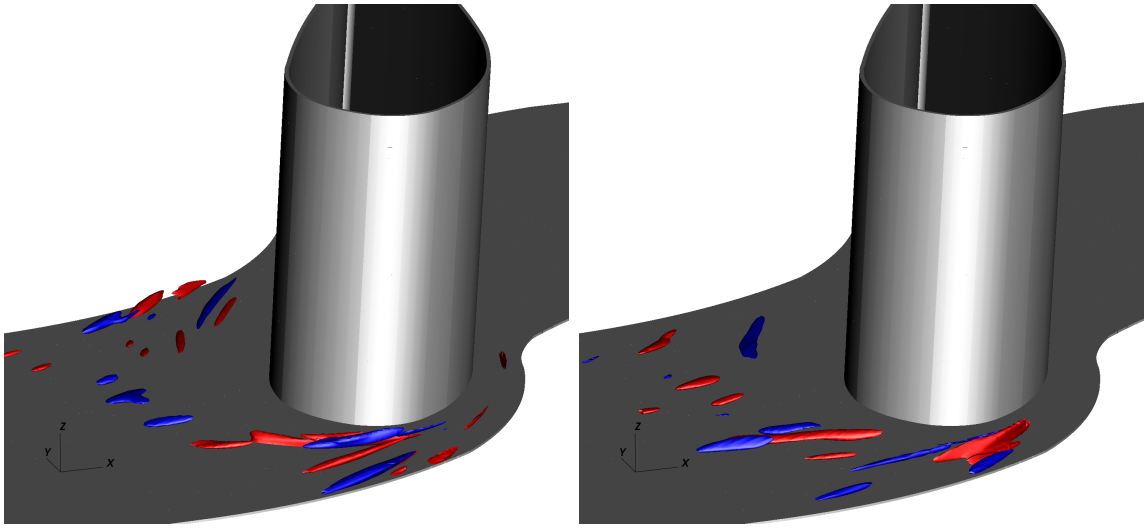

Isosurfaces at -2 (blue) and 2 (red) of scalar spatial basis function of mode 36 (left) and 37 (right).

VITA

Name:	Markus Schwänen
Address:	Department of Mechanical Engineering 3123 TAMU College Station TX 77843-3123
Email Address:	schwaenen@tamu.edu
Education:	Dipl.-Ing. Mechanical Engineering, Technische Universität Darmstadt, Germany, September 2007 Thesis Topic: "Numerical Flow Calculations in Pin Fin Cooling Channels"

The typist for this dissertation was Markus Schwänen.